Available online at www.sciencedirect.com

jmr&t
Journal of Materials Research and Technology

journal homepage: www.elsevier.com/locate/jmrt

Review Article

Thermal stability, mechanical properties, and tribological performance of TiAlXN coatings: understanding the effects of alloying additions

Willey Yun Hsien Liew [a,*], *Hooi Peng Lim* [a], *Gan Jet Hong Melvin* [b], *Jedol Dayou* [c], *Zhong-Tao Jiang* [d]

[a] *Faculty of Engineering, Universiti Malaysia Sabah, Jalan UMS, 88400, Kota Kinabalu, Sabah, Malaysia*
[b] *Centre of Research in Energy and Advanced Materials, Faculty of Engineering, Universiti Malaysia Sabah, Jalan UMS, 88400, Kota Kinabalu, Sabah, Malaysia*
[c] *Energy, Vibration and Sound Research Group (e-VIBS), Faculty of Science and Natural Resources, Universiti Malaysia Sabah, Jalan UMS, 88400, Kota Kinabalu, Sabah, Malaysia*
[d] *Surface Analysis and Materials Engineering Research Group, Chemistry and Physics, College of Science, Health, Engineering and Education, Murdoch University, Perth, WA, 5150, Australia*

ARTICLE INFO

Article history:
Received 1 December 2021
Accepted 3 January 2022
Available online 7 January 2022

Keywords:
Diffusion
Hardness
Oxidation
Microstructure
Wear

ABSTRACT

In tribological applications, the degradation of metallic coatings due to oxidation and thermal softening at high temperatures is an issue of increasing concern. Recently, researchers have focused on the development of durable hard coatings that can perform well under elevated temperatures. The alloying of ternary TiAlN coatings with various elements has received considerable attention due to its ability to improve coating properties at high temperatures by solid solution hardening, grain refinement, formation of new phases, diffusion barriers, and self-lubricious tribo-oxides. This paper reviews the microstructure, thermal stability, oxidation behaviour, and mechanical and tribological properties of resultant quaternary TiAlXN coatings (X = Si, Cr, V, Ta and B). The effects of the deposition parameters, chemical composition, high-temperature annealing, and coating architecture on the coating properties are discussed in depth. The properties of quinary TiAlCrSiN coatings are also reviewed to provide a better understanding of the synergistic effects of Si and Cr additions to TiAlN. The maximum hardness and plastic deformation resistance (H/E and H^3/E^2) of TiAlXN coatings produced by various deposition techniques are compared. This paper provides useful insights into the challenges and future research perspectives of the reviewed coatings.

* Corresponding author.
E-mail address: wyhliew@ums.edu.my (W.Y.H. Liew).
https://doi.org/10.1016/j.jmrt.2022.01.005

1. Introduction

Friction and wear are the primary issues of concern for most mechanical parts with sliding components, especially in machining and tooling applications. The efficiency and performance of machine tools are usually reduced by cumulative material losses due to friction and wear. In this regard, substantial research has been conducted to develop protective coatings for machine tools that decrease friction and wear whilst enhancing tool life, performance, and durability. Various types of coatings have been developed, including aluminide coatings, overlay coatings, nitride-based coatings, and carbide-based coatings [1]. Among these, transition metal nitrides such as titanium nitride (TiN) are extensively used as a coating material for machine tools due to their high hardness, excellent resistance to wear and corrosion, and good chemical stability [2–4]. However, TiN coatings have the disadvantage of forming fast-growing rutile structure TiO_2 at temperatures above 500 °C, making them susceptible to cracks and thus decreasing their oxidation resistance [5,6]. Fateh et al. [7] reported that TiN coatings oxidised at above 600 °C to form TiO_2, and that this oxide did not yield significant lubrication effects and wear protection.

Surface modification by alloying TiN with Al has been found to improve the oxidation resistance, and both the mechanical and tribological properties of TiN coatings at high temperatures. A substitutional solid solution of TiAlN coating can be formed when Al atoms, with a smaller atomic radius, substitute for Ti atoms in the TiN lattice [8–10]. The crystal structure, oxidation resistance, and mechanical and tribological properties of TiAlN are greatly influenced by Al content. The addition of Al to TiN within the solubility limit (<70 at.% Al) has been found to effectively enhance the hardness, wear resistance, and oxidation resistance of protective coatings [11–18]. The substitution of Ti by Al atoms in TiN lattice (with Al content of 50–65 at.%) formed a single-phase cubic-NaCl structure (Ti,Al)N solid solution, which significantly increased hardness and tool life [15]. Greater Al content was found to reduce grain size, resulting in increased hardness [19]. However, Al content above the optimum value of 65 at.% led to a reduction in hardness due to the structural transformation of cubic-NaCl to wurtzite-AlN [12,16]. TiAlN coatings had a high tendency to form protective alumina oxide (Al_2O_3), which suppressed further inward oxygen diffusion to the underlying coating, and thus protected the nitride layer underneath from further oxidation [20]. The initial oxidation temperature for TiAlN was 700 °C (about 200 °C higher than that of TiN) at which Al_2O_3, acting as a barrier against oxygen diffusion, was formed [21]. Vaz et al. [22] found that greater Al content increased the oxidation resistance of $Ti_{1-x}Al_xN$. Compared with $Ti_{0.62}Al_{0.38}N$, $Ti_{0.35}Al_{0.65}N$ (with higher Al concentration) exhibited greater oxidation resistance due to the enhanced suppression of oxygen diffusion by the formation of Al_2O_3 and intermediate Ti–Al mixed oxide. Increasing Al content from $x = 0.65$ to 0.81 led to reduced oxidation resistance, similar to that of AlN, which coincided with a change in the microstructure from NaCl to wurtzite structure. The formation of TiO_2 was undesirable because it could lead to cracking which would consequently accelerate oxidation [20,23]. However, Al_2O_3 was able to protect the TiAlN coating during sliding, resulting in a reduced rate of friction and wear [23–26]. Similarly, the Al_2O_3 formed on the TiAlN coating reduced the adhesion between stainless steel and the coated tools [27]. In adhesion tests, the $Ti_{0.35}Al_{0.65}N$ with cubic B1–NaCl structure failed at the highest critical load, as compared to the other $Ti_{1-x}Al_xN$ coatings [28]. A change in the structure of the $Ti_{1-x}Al_xN$ coatings from cubic ($x = 0.38$ and 0.65) to wurtzite ($x = 0.73$ and 0.81) resulted in a reduction in the critical load and a change in the failure mechanism. The coatings with lower Al content ($x = 0.38$ and 0.65) exhibited conformal cracking at lower loads and chipping at higher loads. In contrast, chipping was the primary failure mode of the higher Al content ($x = 0.73$ and 0.81) coatings.

More recently, many studies have found that incorporating a fourth alloying element to TiAlN can further enhance the oxidation resistance, thermal stability, and the mechanical and tribological properties of the coatings at elevated temperatures (up to 1000 °C). In particular, the influence of Si addition TiAlN coatings has been extensively investigated [29–32]. The superior mechanical properties of TiAlSiN over TiAlN coatings can be attributed to their nanocomposite structure consisting of an amorphous (a-Si_3N_4) phase embedded along the grain boundaries in nanocrystalline nc-(Ti,Al)N. The preferential oxidation of TiAlSiN to form Al_2O_3 assisted by Si addition increased the oxidation resistance of the coating as the Al_2O_3 served as a diffusion barrier, which retarded further oxidation up to 1000 °C [33–35]. Additionally, the formation of lubricious oxides such as Cr_2O_3 and V_2O_5 by alloying Cr [36,37] and V [38] to TiAlN at high temperatures was responsible for the low friction coefficient (COF) and low wear rate of the coatings. Alloying Ta to TiAlN has been found to suppress the formation of wurtzite AlN and to stabilise the early formation of the rutile r-TiO_2 phase, thus avoiding the anatase-to-rutile TiO_2 phase transformation [39,40]. This led to an improvement in thermal stability and oxidation resistance. Baker et al. [41] reported that incorporating B into TiAlN produced a nanocomposite coating consisting of nanocrystalline nc-(Ti,Al)N grains separated by amorphous BN (a-BN) and TiB_2 phases, which exhibited superior wear resistance to TiN and (Ti,Al)N.

It was also reported that high-temperature annealing was able to increase the hardness of coatings by forming coherent interfaces resulting from spinodal decomposition, which effectively restricted dislocation movement across the phases [42]. Additionally, the design of multilayer structures comprising of alternating layers with different attributes (e.g. hardness and elastic modulus) significantly enhanced the coating properties. Hardness enhancement in multilayer coatings has been attributed to the hindering of dislocation motion by the interfaces between the layers [43–45]. Furthermore, the interfaces between two adjacent layers in a multilayer structure can deflect crack propagation and retard grain boundary slip, producing a hard yet tough coating [46]. Therefore, it might be expected that the combined effect of quaternary coatings and multilayer structures would result in coatings with excellent characteristics. This paper provides a review of the effects of Si, Cr, V, Ta, and B on the microstructure, thermal stability, oxidation behaviour, wear

resistance, and tribological properties of TiAlXN coatings (where X = Si, Cr, V, Ta and B). The discussion will include the influence of the deposition parameters (i.e. substrate bias voltage, nitrogen pressure or flow rate, modulation period, different ratio of target or cathode composition), high-temperature annealing, and coating architecture on the properties of quaternary coatings. In addition, quinary nanocrystalline coatings produced by introducing Si and Cr simultaneously into TiAlN are also reviewed to provide a better understanding of the synergetic effect of these alloying elements on coating properties. This synergy is increasingly attractive in advanced surface engineering applications.

2. Review of TiAlSiN coatings

2.1. *Mechanical, thermal stability, oxidation and tribological behaviour of TiAlSiN monolayer coatings*

The effects of Si content on the mechanical, oxidation, thermal stability, and tribological properties of TiAlSiN coatings have been well-studied. Yu et al. [47] reported a change in the hardening mechanism in TiAlSiN with Si content. At 2.02 at.% Si, increased hardness was observed due to reduced grain size (the Hall-Petch effect) and the formation of Ti(AlSi)N solid-solution phase with lattice distortion introduced by the Si and Al atoms dissolving in the TiN. Increasing the Si content to 4.78–7.95 at.% led to the formation of nanocrystalline Ti(AlSi)N embedding in the amorphous Si_3N_4 matrix, giving rise to increased hardness and strength of adhesion to the substrate. The coating with 4.78 at.% Si exhibited a relatively low COF (compared with TiAlSiN coatings with 0, 13.44 and 22.14 at% Si contents) and provided better wear protection for tools (compared with TiAlN and TiN coatings) in the high-speed machining of hardened steel under dry conditions. The diameter of the crystallites in the TiAlSiN coating with 5 at.% Si was less than 13 nm, which was significantly smaller than that of the TiAlN (diameter ~33 nm). Above 7.95 at.% Si, the hardness reduced due to excessive amorphous Si_3N_4 produced, Carvalho et al. [48] found that solid solution (Ti,Si,Al)N was developed under conditions of low surface mobility by the substitution of Ti by Si and Al atoms in the TiN lattice. Alternately, nc-Ti(Al)N/a-Si_3N_4 was developed by the segregation of Si atoms under conditions of high surface mobility. Several researchers had attributed the increase in hardness with increasing Si content to the reduction in grain size, the strengthening of grain boundaries by the strong cohesive energy of the amorphous and crystalline interphase boundaries, and the restriction of dislocation motion by the amorphous Si_3N_4 phase at grain boundaries [49–55].

Coatings with both high hardness and resistance to plastic deformation are highly desirable. H^3/E^2 and H/E are regarded as an indicator of the material to resist plastic deformation. Many researchers have found that maximum hardness, H/E and H^3/E^2 could be obtained using appropriate Si content [47,49–51,56–62] (see Figs. 1 and 2 and Table 1). However, increasing Si content beyond its optimum value led to a reduction in these mechanical properties, which often resulted in reduced wear resistance, due to the formation of excessive amorphous Si_3N_4 phase [47,49,62]. Flink et al. [63] attributed the decrease in the hardness of TiAlSiN coatings with increasing Si content to the formation of hexagonal wurtzite (Al,Ti,Si)N and a significant amount of amorphous Si_3N_4 phase. Coatings with superior resistance to plastic deformation were explained by the ability of the nano-sized crystallites Ti(AlSi)N in the amorphous Si_3N_4 and AlN to resist dislocation motion [56].

Besides Si content, Al/Ti ratio and Al content have also been found to significantly influence the microstructure and mechanical properties of protective coatings. By fixing the Si content and varying the Al/Ti ratio, Tillmann and Dildrop [49] showed that hardness was also governed by the Al/Ti ratio. Hardness increased from 26.3 to 31.3 GPa, with an increase in

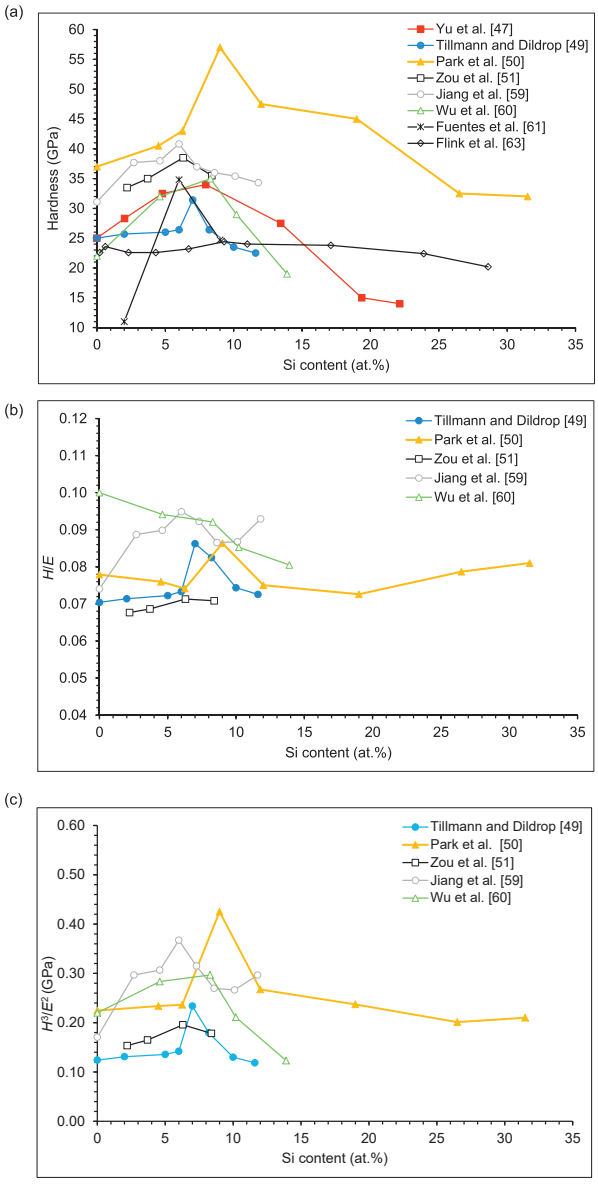

Fig. 1 – Comparison of the (a) hardness, (b) H/E and (c) H^3/E^2 ratio measured for TiAlSiN coatings deposited by various deposition techniques as a function of Si content (For coatings with optimum Si content of between 6 and 9.3 at.% Si).

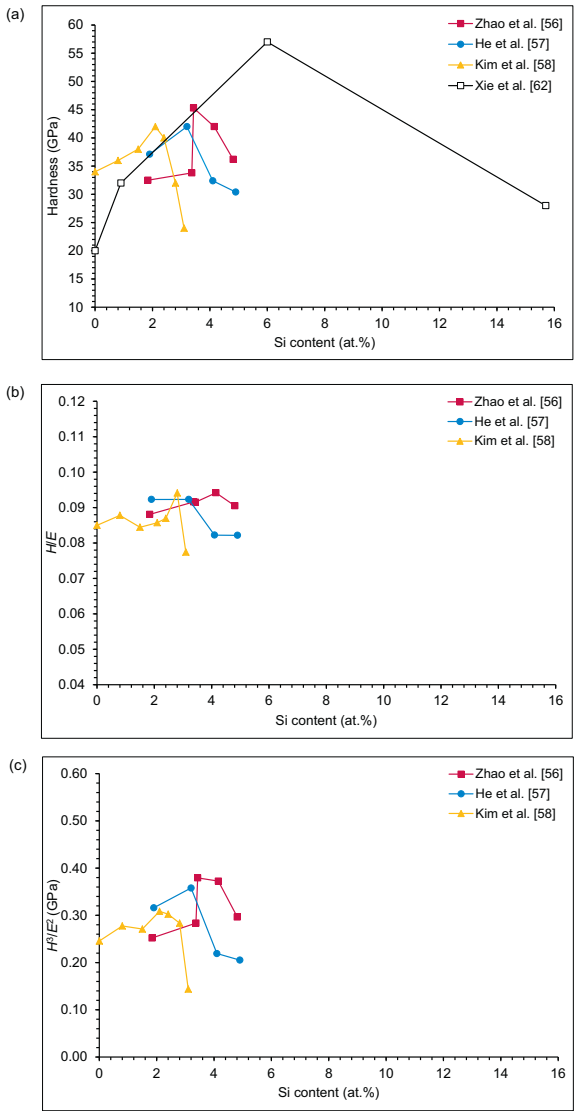

Fig. 2 – Comparison of the (a) hardness, (b) *H/E* and (c) H^3/E^2 ratio measured for TiAlSiN coatings deposited by various deposition techniques as a function of Si content (For coatings with optimum Si content of between 2.1 and 6 at.% Si).

the Al/Ti ratio from 1.02 to 1.16. However, a reduction in hardness to 22 GPa was observed when the Al/Ti ratio was increased to 1.24 (Table 1). Fuentes et al. [61] found that TiAlSiN coatings with 6 and 9 at.% Si consisted of (Ti,Al,Si)N solid solution of Ti replaced by Al and Si atoms. Low Si content of 2 at.% produced a high Al/Ti ratio (Table 1), and thus the microstructure was dominated by wurtzite phase. This resulted in low adhesion strength and hardness, leading to a high wear rate. Martin et al. [64] also found that the effect of Si on hardness, *H/E* and H^3/E^2 was governed by the Ti/Al ratio. As shown in Table 1, the hardness, *H/E* and H^3/E^2 of the coating deposited using a $TiAl_{50:50}$ cathode increased with greater Si content. Using $TiAl_{75:25}$ and $TiAl_{33:67}$ cathodes, the hardness, *H/E* and H^3/E^2 reduced with increasing Si. All TiAlSiN coatings with various chemical compositions had a grain size of less than 10 nm. Chen et al. [65] studied the effect of Al content on the microstructure and mechanical properties of TiAlSiN coatings using $Ti_{0.94}Si_{0.06}N$, $Ti_{0.62}Al_{0.32}Si_{0.06}N$, and $Ti_{0.48}Al_{0.46}Si_{0.06}N$ coated samples. Greater Al content led to a reduction in the x value of nc-$Ti_{1-x}N$/a-Si_3N_4, which in turn gave rise to increased hardness and a grain size reduction from 10 to 3.6 nm, with x = 1 and 0.51, respectively. In the continuous dry turning of stainless steel, the WC tool coated with the hardest $Ti_{0.48}Al_{0.46}Si_{0.06}N$ coating exhibited the longest tool life. This was followed by the $Ti_{0.62}Al_{0.32}Si_{0.06}N$ and $Ti_{0.94}Si_{0.06}N$ coated tools. Jiang et al. [59] found that both Al and Si content governed the grain size in the TiAlSiN coatings. An increase in Si content impeded the growth of TiN grains, leading to a reduction in grain size. An initial increase in Al content promoted grain growth before excessive Al content reduced the grain size. The vacancy, solid solution, and precipitate hardening effects which were governed by the chemical composition, appeared to have also contributed to variation in coating hardness. Due to the various factors at work simultaneously, it was difficult to predict the optimal Al and Si content which would yield the hardest coating. Experimental results showed that intermediate Al and Si content (7.5 and 6 at.%, respectively) gave rise to the highest hardness.

Various deposition processes produced TiAlSiN monolayer coatings with maximum hardness, *H/E* and H^3/E^2 of 24.4–57.0 GPa, 0.0713–0.1164 and 0.1957–0.4333 GPa, respectively, at the optimum Si content of 2.1–9.3 at.% (Table 1). The means of the maximum hardness, *H/E* and H^3/E^2 values were 38.9 ± 9.1 GPa, 0.0922 ± 0.0105 and 0.3291 ± 0.0738 GPa, respectively. The optimum Si content for peak hardness, as obtained by Yu et al. [47], Tillmann and Dildrop [49], Zou et al. [51], Jiang et al. [59], Wu et al. [60], Fuentes et al. [61] and Flink et al. [63], was between 6 and 9.3 at.% (Fig. 1). These studies showed that increasing Si content produced neither a significant change [47,49] nor a reduction [59–61,63] in Al/Ti ratio up to the peak hardness. Zhao et al. [56], He et al. [57], Kim et al. [58] and Xie et al. [62] obtained lower optimum Si content of 2.1–6 at.% (Fig. 2). It was found that as Si content was increased, either Ti content decreased while Al content stayed essentially the same [58] or that Ti content decreased while Al content increased [57,62]. In both cases, the Al/Ti ratio increased and it is possible that this promoted the formation of wurtzite phase (resulting in a peak hardness at a lower Si content) [61] and also caused the solute solution to attain its solubility limit at a lower Si content, which would then form nanocrystal Ti(AlSi)N/amorphous Si_3N_4 phase. These effects could have shifted the optimum Si contents to a lower value.

Cao et al. [66] observed a change in the microstructure of TiAlSiN coatings (from coarse columnar to fine-grained) with increasing bias voltage (Table 1). This did not significantly alter the chemical composition of the coatings. Although the columnar grained coatings had a lower hardness and H^3/E^{*2} (E* is the effective elastic modulus), they exhibited greater wear resistance since the coarse grains had less tendency to be pulled out. However, H^3/E^{*2} had a direct influence on the critical loads for the cracking and spallation of coatings, (i.e. higher H^3/E^{*2} required a higher critical load). Chen et al. [67] found that increasing the bias voltage made virtually no change to the chemical composition of TiAlSiN coatings. However, it did result in increased hardness (Table 1) and

Table 1 – Summary of the deposition method and parameters, substrate, elemental composition, and hardness, Young's modulus, H/E and H^3/E^2 of TiAlSiN monolayer coatings.

Ref.	Deposition method	Substrate	Voltage	Si content (at.%)	Ti content (at.%)	Al content (at.%)	Al/Ti	Hardness (GPa)	Young's Modulus (GPa)	H/E	H^3/E^2 (GPa)	Remark
Yu et al. [47]	Hollow cathode discharge (HCD) and mid- frequency magnetron sputtering (MFMS) hybrid coating deposition	Si (100) wafer (XPS characterization), mirror polished SUS304 stainless steel plates (SEM, EDX and XRD characterization, nano-indentation), cemented carbide insert (scratch test), cemented carbide endmill (machining)	Constant bias voltage of −200 V	0	45.12	19.76	0.4379	25.0[a]				[a]estimated from Fig. 7 in ref. [47]
				2.02	49.66	10.38	0.2090	28.3[a]				
				4.78	46.90	10.27	0.2190	32.5[a]				
				7.95	46.52	10.58	0.2274	34.0[a]				
				13.44	42.20	11.63	0.2756	27.5[a]				
				19.36	38.32	10.70	0.2792	15.0[a]				
				22.14	35.70	11.25	0.3151	14.0[a]				
Tillmann and Dildrop [49]	Direct current (DC) magnetron sputtering	Hot work steel AISI H11 (SEM and XRD characterization, nano-indentation, scratch and ball-on-disc tests)	Not available	≈7			1.02	26.3[b]	310[b]	0.0839	0.1829	[b]estimated from Fig. 2 in ref. [49]
				≈7			1.03	27.0[b]	330[b]	0.0818	0.1807	[c]estimated from Fig. 3 in ref. [49]
				≈7			1.09	27.5[b]	360[b]	0.0778	0.1694	[d]estimated from Fig. 3 in ref. [49]
				≈7			1.16	31.3[b]	350[b]	0.0943	0.2934	
				≈7			1.21	28.8[b]	340[b]	0.0853	0.2110	
				≈7			1.24	22.0[b]	300[b]	0.0733	0.1183	
				0[c]			1.16	25.0[d]	355[d]	0.0704	0.1240	
				2[c]			1.16	25.7[d]	360[d]	0.0714	0.1310	
				5[c]			1.16	26.0[d]	360[d]	0.0722	0.1356	
				6[c]			1.16	26.4[d]	360[d]	0.0733	0.1420	
				7[c]			1.16	31.4[d]	364[d]	0.0863	0.2337	
				8.2[c]			1.16	26.4[d]	320[d]	0.0825	0.1797	
				10[c]			1.16	23.5[d]	316[d]	0.0744	0.1300	
				11.6[c]			1.16	22.5[d]	310[d]	0.0726	0.1185	
Park et al. [50]	Arc ion plating	WC–Co (SEM, EDX, EPMA, XRD, TEM and XPS characterization, nano-indentation, ball-on-disc test)	Constant bias voltage of −25 V	0				37.0[e]	475[e]	0.0779	0.2245	[e]estimated from Fig. 7 in ref. [50]
				4.5				40.5[e]	533[e]	0.0760	0.2338	
				6.25				43.0[e]	580[e]	0.0741	0.2363	
				9				57.0[e]	650[e]	0.0864	0.4251	
				12				47.5[e]	633[e]	0.0750	0.2675	
				19				45.0[e]	620[e]	0.0726	0.2371	
				26.5				32.5[e]	413[e]	0.0787	0.2013	
				31.5				32.0[e]	395[e]	0.0810	0.2100	
Zou et al. [51]	Unbalanced magnetron sputtering	Si (111) wafers (AFM, EDX, XPS and TEM characterization) mirror polished stainless steel (nano-indentation, ball-on-disc test)	Constant bias voltage of −75 V	2.2	35	12	0.3429	33.5[f]	495[f]	0.0677	0.1534	[f]estimated from Fig. 7(a) in ref. [51]
				3.7	34	13	0.3824	35.0[f]	510[f]	0.0686	0.1648	
				6.3	33	14	0.4242	38.5[f]	540[f]	0.0713	0.1957	
				8.4	34	15	0.4412	35.5[f]	501[f]	0.0709	0.1782	
Sui et al. [52]	Reactive magnetron sputtering	WC-8 wt.% Co inserts (SEM, EDX, XRD, TEM and XPS characterization, nano-indentation, scratch test, machining)	Not available	7				22				
Zhao et al. [56]	Plasma immersion ion implantation	WC-8 wt.% Co (SEM, EDX, XRD, XPS and TEM characterization, nano-indentation, scratch test)	Pulsed substrate bias of: Magnitude: 15 kV Frequency: 100 Hz Pulse width: 60 μs	1.84	42.44	3.13	0.0738	32.5[g]	369[g]	0.0881	0.2521	[g]estimated from Fig. 6 in ref. [56]
				3.37	38.51	1.91	0.0496	33.8[g]	369[g]	0.0916	0.2836	
				3.43	37.97	1.97	0.0519	45.3[g]	495[g]	0.0915	0.3794	
				4.15	39.10	1.82	0.0465	42.0[g]	446[g]	0.0942	0.3725	
				4.81	43.72	1.73	0.0396	36.2[g]	400[g]	0.0905	0.2965	

(continued on next page)

Table 1 – (*continued*)

Ref.	Deposition method	Substrate	Voltage	Si content (at.%)	Ti content (at.%)	Al content (at.%)	Al/Ti	Hardness (GPa)	Young's Modulus (GPa)	H/E	H^3/E^2 (GPa)	Remark
He et al. [57]	Hybrid PVD technology	Polished p-type silicon (111) wafer (XPS, TEM and XRD characterization), Ni-based high-temperature alloy (SEM and Raman characterization, nano-indentation, scratch and pin-on-disc tests)	Constant bias voltage of −100 V	1.9 3.2 4.1 4.9	48.6 45.8 43.3 36.8	6.2 9.7 11.6 16.8	0.1276 0.2118 0.2679 0.4565	37.1 42.0 32.4 30.4	402 455 394 370	0.0923 0.0923 0.0822 0.0822	0.3160 0.3579 0.2191 0.2052	
Kim et al. [58]	Closed field unbalanced magnetron sputtering	Si (100) wafer (AES, XRD, XPS and TEM characterization), AISI H13 steel (nano-indentation, ball-on-disc test)	Constant bias voltage of −100 V	0 0.8 1.5 2.1 2.4 2.8 3.1	31.0 30.0 29.0 27.5 28.0 27.5 26.5	25.0 25.5 26.0 25.5 25.5 25.0 25.5	0.8065 0.8500 0.8966 0.9273 0.9107 0.9091 0.9623	34[h] 36[h] 38[h] 42[h] 40[h] 32[h] 24[h]	400[h] 410[h] 450[h] 490[h] 460[h] 340[h] 310[h]	0.0850 0.0878 0.0844 0.0857 0.0870 0.0941 0.0774	0.2457 0.2775 0.2710 0.3086 0.3025 0.2835 0.1439	[h]estimated from Fig. 5 in ref. [58]
Jiang et al. [59]	Reactive close-field unbalanced magnetron sputtering	Si (100) (SEM, EDX, XPS and XRD characterization, nano-indentation, residual stress measurement)	Constant bias voltage of −60 V	0 2.7 4.6 6.0 7.3 8.6 10.1 11.8	29.7 29.5 30.2 31.5 30.4 29.4 32.1 32.4	16.7 12.1 10.6 7.5 5.6 4.0 1.9 –	0.5623 0.4102 0.3510 0.2381 0.1842 0.1361 0.0592 –	31.1[i] 37.7[i] 38.0[i] 40.8[i] 37.0[i] 36.0[i] 35.4[i] 34.3[i]	420[i] 425[i] 423[i] 430[i] 401[i] 416[i] 408[i] 369[i]	0.0740 0.0887 0.0898 0.0949 0.0923 0.0865 0.0868 0.0930	0.1705 0.2967 0.3067 0.3673 0.3150 0.2696 0.2665 0.2964	[i]estimated from Fig. 9 in ref. [59]
Wu et al. [60]	Hybrid PVD technology	Polished p-type silicon (111) wafers (FESEM, TEM, XRD and XPS characterization), high-temperature alloy (nano-indentation, thermal stability study, ball-on-disc test)	Constant bias voltage of −100 V	0 4.6 8.3 10.2 13.9	22.0 30.4 27.7 28.3 22.7	33.1 26.7 22.2 24.2 20.1	1.5045 0.8783 0.8014 0.8551 0.8855	22[j] 32[j] 35[j] 29[j] 19[j]	220[j] 340[j] 380[j] 340[j] 236[j]	0.1000 0.0941 0.0921 0.0853 0.0805	0.2200 0.2835 0.2969 0.2110 0.1232	[j]estimated from Fig. 5 in ref. [60]
Fuentes et al. [61]	Cathodic arc evaporation	Hot work steels DIN 1.2344 (FESEM, EDX GDOES and XRD characterization, nano-indentation, scratch and ball-on-disc tests)	Constant bias voltage of −60 V	2 6 9	9 31 23	24 10 12	2.6667 0.3226 0.5217	11.0 34.8 24.7	263 472 336	0.0418[+] 0.0737[+] 0.0735[+]	0.0192[+] 0.1892[+] 0.1335[+]	[+]Calculated based on E*
Xie et al. [62]	Multi-plasma immersion ion implantation and deposition	Si (100) wafer (SEM, EDX, XRD and XPS characterization), polished M2 tool steel (nano-indentation, scratch test)	Pulsed substrate bias of: Magnitude: 20 kV Frequency: 50 Hz Pulse width: 60 μs	0 0.9 6.0 15.7	45.1 46.1 40.2 35.5	0 0.4 2.7 5.6	– 0.0087 0.0672 0.1577	20[k] 32[k] 57[k] 28[k]				[k]estimated from Fig. 5 in ref. [62]

Flink et al. [63]	Arc evaporation	WC-6 wt.% Co (SEM, EDX, XRD and TEM characterization, nano-indentation, machining, thermal annealing study)	Constant bias voltage of −35 V	0.2	38.9	60.9	1.5656	22.6[m]				[m]estimated from Fig. 4 in ref. [63]
				0.6	37.6	61.7	1.6410	23.6[m]				
				2.3	36.7	61.0	1.6621	22.6[m]				
				4.3	38.8	56.9	1.4665	22.6[m]				
				6.7	35.7	57.6	1.6134	23.2[m]				
				9.3	35.5	55.2	1.5549	24.4[m]				
				11.0	34.5	54.5	1.5797	24.0[m]				
				17.1	32.8	50.1	1.5274	23.8[m]				
				23.9	30.8	45.3	1.4708	22.4[m]				
				28.6	28.1	43.3	1.5409	20.2[m]				
Martin et al. [64]	Vacuum arc	Aluminium foil (EDX, XPS and XRD characterization), semiconductor-grade polished (100)-conducting silicon (nano-indentation, TEM and FIB characterization)	Constant bias voltage of −150 V	$TiAl_{75:25}$								
				0				31	365	0.0849	0.2236	
				4				30	340	0.0882	0.2336	
				5				27	320	0.0844	0.1922	
				$TiAl_{50:50}$								
				0				28	332	0.0843	0.1992	
				5.5				32	275	0.1164	0.4333	
				$TiAl_{33.67}$								
				0				24	282	0.0851	0.1738	
				7.5				21	253	0.0830	0.1447	
				14				16	222	0.0721	0.0831	
Cao et al. [66]	Pulsed-DC reactive magnetron sputtering	M42 tool steel (SEM, EDX and FIB characterization, scratch and ball-on-disc tests)	Bias voltage (V) of:									[+]Calculated based on E*
			−40	1.8 ± 0.3	37.7 ± 1.9	11.3 ± 0.5		27.6	360.0	0.0767[+]	0.1622[+]	
			−50	1.8 ± 0.3	37.7 ± 1.9	11.3 ± 0.5		28.3	358.5	0.0789[+]	0.1764[+]	
			−60	1.8 ± 0.3	37.7 ± 1.9	11.3 ± 0.5		31.5	368.4	0.0855[+]	0.2303[+]	
			−70	1.8 ± 0.3	37.7 ± 1.9	11.3 ± 0.5		33.8	369.0	0.0916[+]	0.2836[+]	
			−80	1.8 ± 0.3	37.7 ± 1.9	11.3 ± 0.5		34.1	378.0	0.0902[+]	0.2775[+]	
Chen et al. [67]	Modulated pulsed power magnetron sputtering	Si (100) wafers (EPMA, XRD, FESEM and TEM characterization, nano-indentation, residual stress measurement, thermal conductivity study)	Bias voltage (V) of:									[n]estimated from Fig. 5 in ref. [67] [+]Calculated based on E*
			−35	4.8	17.9	25.9	1.4469	31.0[n]	400[n]	0.0775[+]	0.1862[+]	
			−65	4.7	18.2	26.1	1.4341	32.5[n]	405[n]	0.0802[+]	0.2093[+]	
			−100	4.8	17.9	26.2	1.4637	34.4[n]	415[n]	0.0829[+]	0.2364[+]	
			−130	5.1	18.0	25.3	1.4056	37.5[n]	425[n]	0.0882[+]	0.2920[+]	
Ma et al. [68]	High power impulse magnetron sputtering	WC-10 wt.% Co (SEM, EDX, AFM and XRD characterization, nano-indentation, scratch test)	Bias voltage (V) of:									
			−60	4.29	25.04	19.76	0.7891	30.14	357.11	0.0844	0.2147	
			−90	4.25	26.18	18.85	0.7200	34.14	418.25	0.0816	0.2275	
			−120	4.15	27.65	17.70	0.6401	42.23	567.22	0.0745	0.2341	
			−150	3.92	28.66	16.94	0.5911	40.76	545.52	0.0747	0.2276	
Tillmann and Dildrop [69]	Magnetron sputtering	Hot work steel AISI H11 (SEM and EDX characterization, nano-indentation)	Bias voltage (V) of:									[p]estimated from Fig. 3 in ref. [69]
			−75	7.46	17.55	18.28	1.0416	25.0[p]	310.0[p]	0.0806	0.1626	
			−100	7.13	17.79	18.84	1.0590	27.1[p]	350.0[p]	0.0774	0.1625	
			−125	7.14	19.12	19.56	1.0230	25.0[p]	293.3[p]	0.0852	0.1816	
			−150	7.11	19.48	19.83	1.0180	23.5[p]	266.7[p]	0.0881	0.1825	
			−200	6.88	19.62	19.94	1.0163	21.0[p]	263.3[p]	0.0798	0.1336	
Chen et al. [73]	Cathodic arc evaporation	WC-6 wt.% Co and WC-10 wt.% Co tools (EPMA, SEM and XRD characterization, nano-indentation, machining)	Constant bias voltage of −100 V	6				42.4				
Chang et al. [86]	Cathodic arc evaporation	Si substrates (EPMA, FESEM, EDX, XRD, TEM and FIB characterization), WC-Co (nano-indentation, scratch and ball-on-disc tests)	Constant bias voltage of −120 V	7				38	515	0.0738	0.2069	

compressive stress, reduced grain size (from 16 to 5 nm) and altered microstructure (from a dense columnar to a featureless and flat cross-sectional structure). Similarly, Ma et al. [68] observed an increase in hardness, a reduction in grain size (from 10.5 to 7.4 nm), and a microstructural change from columnar to dense structure with increasing bias voltage (Table 1). However, increasing the bias voltage was found to decrease adhesion strength. The increase in hardness with bias voltage was attributed to the change in the microstructure as well as the increase in compressive stress and reduction in grain size via continuous nucleation produced by high ion bombardment [69]. It should be noted that extremely high bias voltage produced defects leading to reduced hardness. Ma et al. [68] and Tillmann and Dildrop [69] showed that variation of the bias voltage did not significantly change the chemical composition. Fig. 3 shows the variation in coating hardness with negative bias voltages (V). The maximum hardness, H/E and H^3/E^2 obtained by varying the bias voltage were 27.1–42.2 GPa, 0.0844–0.0881 and 0.1825–0.2341 GPa, respectively, with means of 35.2 ± 3.5 GPa, 0.0863 and 0.2083 GPa.

Studies have been conducted to investigate the thermal stability of TiAlSiN coatings. Chang et al. [70] found that TiAlSiN retained the as-deposited hardness of 36 ± 2 GPa during annealing at 700 °C. A slight reduction in hardness to 33 ± 1 GPa occurred at 900 °C, indicating good thermal stability. In contrast, the hardness of TiAlN coatings reduced significantly from 31 ± 1 GPa (as-deposited hardness) to 26 ± 2 and 19 ± 2 GPa upon annealing at 700 and 900 °C, respectively. Similarly, $Ti_{0.78}Si_{0.04}Al_{0.18}N$, $Ti_{0.66}Si_{0.13}Al_{0.21}N$, and $Ti_{0.63}Si_{0.13}Al_{0.24}N$ exhibited peak hardness at an annealing temperature of 800 °C before a decrease in hardness was registered at 900 °C [48]. Pei et al. [71] observed that the optimum annealing temperature for TiAlSiN coatings was 1000 °C. This was higher than that of the TiAlN coatings at 800 °C, which were completely oxidised at 850 °C. The delay in the formation of w-AlN (known to reduce the coating hardness) caused by the presence of Si was the reason for the 200 °C increase in optimum temperature. Xie et al. [72] reported that although the surface of the TiAlSiN coating oxidised at 800 °C exhibited TiO_2, Al_2O_3, and SiO_2, it still maintained a high level of hardness and wear resistance because a nanocomposite structure consisting of TiO_2 nanocrystals embedded in an amorphous SiO_2 matrix was retained in the oxidised layer. Chen et al. [73] attributed the high hardness of TiAlSiN coated tools at the annealing temperatures of 700–900 °C to the retarding effects of the amorphous Si_3N_4 on the formation of h-AlN. If Si content was not high enough to produce sufficient a-Si_3N_4 phase to retard recrystallisation, a reduction in the hardness of the coating would occur upon annealing [74].

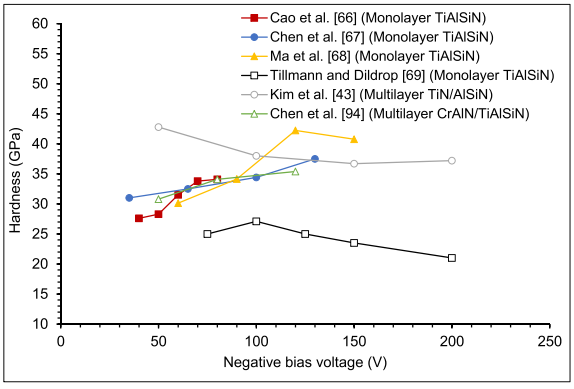

Fig. 3 – Variation in the hardness of the monolayer and multilayer TiAlSiN coatings with negative bias voltages.

Hong et al. [75] investigated the oxidation behaviour of TiAlSiN coatings, mainly consisting of TiN, Si_3N_4 and AlN, with increasing annealing temperature up to 800 °C. At 400 °C, a considerable amount of TiN was oxidised to form Ti_2O_3. The onset oxidation temperature for Si_3N_4 and AlN to form SiO_x and AlO_x was higher at 600 °C. As the annealing temperature increased, the oxides grew from the surface towards the interior of the coating, resulting in coarsening of the microstructure. The dominant wear mechanisms of the as-deposited coating sliding on a Ti6Al4V ball were oxidation and adhesion. Coatings annealed at 800 °C suffered a higher wear rate due to abrasion aggravated by the coarsening of microstructure and intense oxidation. Barshilia et al. [76] found that the TiAlSiN coatings were stable up to an annealing temperature of 850 °C and only started to oxidise at 900 °C, forming rutile TiO_2 (r-TiO_2) phase and Al_2O_3. Similarly, Chen et al. [74] found that TiAlSiN coatings with higher Al and Si content exhibited greater oxidation resistance and thus better wear resistance at elevated temperatures. Al and Si promoted the formation of interfacial a-Si_3N_4 and nc-TiO_2-Al_2O_3/a-SiO_2, leading to dense Al_2O_3 and SiO_2 on the surface which served to prevent the inward diffusion of oxygen. Interfacial a-Si_3N_4 played an important role in suppressing oxygen diffusion through the column boundaries. Si also inhibited the undesirable transformation of cubic TiN to r-TiO_2, which could cause significant volume expansion and consequently the spallation of oxide layers. The oxidation onset temperature for TiAlN was 650 °C. The onset temperature for TiAlSiN was higher and increased with Al and Si content up to 830 °C.

Several researchers have proposed different mechanisms by which Si content served to increase the oxidation resistance of TiAlSiN. Si was found to delay the transition of anatase TiO_2 (a-TiO_2) to porous r-TiO_2 and to favour the formation of dense Al_2O_3 on the coating surface, consequently impeding the diffusion of oxygen atoms into the material [60,71,77–79]. The formation of a SiO_2 tribo-layer due to the oxidation of Si_3N_4 also prevented the diffusion of oxygen [80]. However, excessive Si could cause the formation of large amounts of amorphous phase and, thus, a deterioration in oxidation resistance [60]. Sui et al. [52] found that TiAlN had a coarse columnar structure but in contrast TiAlSiN coating had a dense nanocrystalline structure embedded in the amorphous matrix due to the suppression of grain coalescence by the Si_3N_4 amorphous phase at its grain boundaries. A dense nanocrystal structure has higher oxidation resistance since it has fewer pathways for the diffusion of oxygen atoms. In the high-speed turning of titanium with coolant, the TiAlSiN coated tool exhibited a longer tool life with a less built-up edge, and less adhesive wear and chipping at the tool edge due to its high hardness and good oxidation resistance.

Sui et al. [52] attributed the excellent adhesion of TiAlN, as compared to TiAlSiN, to its relatively low hardness and columnar structure. The Ti(AlSi)N crystal lattice distortion also contributed to the poor adhesion of the TiAlSiN coating.

Yu et al. [47] reported that low Si content increased the adhesion of the coating to the substrate. Increasing the Si content from 4.78 to 22.14 at.% caused large amounts of amorphous Si_3N_4 matrix to form which led to a reduction in adhesion strength. In contrast, Philippon et al. [81] found that the TiAlSiN coating with 15 at.% Si exhibited higher adhesion strength and wear resistance than the coating with 7 at.% Si due to the greater presence of amorphous phase. The amorphous phase played an essential role in offsetting the deterioration of adhesion strength caused by the high compressive residual stress induced by the applied substrate bias. Zhu et al. [82] found that while high residual compressive stress contributed to the relatively high hardness of the TiAlSiN, it diminished the adhesion strength of the coating. In scratch tests, the failure mode of the TiAlSiN coatings was buckling spallation due to their high toughness and poor adhesion strength. In contrast, the failure mode of the TiAlN coatings was wedging spallation due to their inferior toughness and high adhesion strength (Fig. 4). Better adhesion strength could be achieved by depositing a buffer layer, such as TiAlN and Ti, at the coating/substrate interface [45,73,83]. Alternatively, adhesion strength could be improved by means of gradually reducing the Si content toward the interface to reduce the residual compressive stress thereat. Lü et al. [84] showed that reducing the Si content from the surface towards the substrate improved the adhesion strength of TiAlSiN coatings with little sacrifice of hardness. This coating (known as gradient coating) had a slightly lower hardness than the non-gradient TiAlSiN coating (with uniformly distributed Si content) but possessed similar adhesion strength to that of the TiAlN coating. The longer tool life exhibited by the gradient coated tools, as compared to the non-gradient and TiAlN coated tools, in the wet machining of titanium was due to their outstanding hardness and adhesion strength. Deposition of $Ti_{1-x}(Al_ySi_{1-y})_xN$ coatings, using an HiPIMS/DCMS configuration (with the substrate bias pulses applied with Al+/Si + supplantation effect and minimization of Ar + irradiation) had yielded some interesting results [85]. The solubility limit was found to increase with a reduction in x value. As a result, lower x values required greater Si content (i.e. lower y value) to achieve precipitation of w-AlN. For certain x and y ratios, the coating films were almost stress-free (<0.5 GPa) whilst still possessing high hardness (~30 GPa).

In the dry milling of titanium alloy at 150 and 200 m/min, TiAlSiN coated tools exhibited higher resistance to notch wear, chipping and thermal cracking [80]. The TiAlSiN coating also showed a lower tendency to delaminate owing to its superior oxidation and strength of adhesion with the substrate. The TiAlSiN coated tool, which exhibited higher resistance to various wear modes, had a tool life outperforming the AlTiN coated tool by 32 and 66% at cutting speeds of 150 and 200 m/min, respectively. In the high-speed milling of Ti–6Al–4V under dry conditions, the TiAlSiN coated tool with superior hot hardness, exhibited higher resistance to abrasion wear than the TiAlN coated tool [70]. However, the TiAlSiN coated tools showed poorer performance in milling steel due to the low adhesion strength of the coating with the substrate [73]. In milling, where tools are subject to impact, the most important properties a coated tool must possess in order to ensure high durability are high toughness and adhesion strength.

It has been widely reported that Si has a significant influence on the tribological properties of TiAlSiN coatings. The reported decrease in the COF with increasing Si content has been attributed to the greater amount of SiO_2 and $Si(OH)_2$ tribo-layers produced by the reaction between the Si_3N_4 and humidity [50,51,58,60]. Kim et al. [54] attributed the superior wear resistance of the TiAlSiN coated tools (as compared to TiAlN coated tools) in the high-speed machining of hardened die steel under dry conditions to the formation of these tribo-layers and their high levels of hardness. Temperature governed the type of tribo-layer formed at the sliding surfaces, as shown in Fig. 5 [57]. The relatively low levels of wear and friction measured in the sliding tests carried out on TiAlSiN at

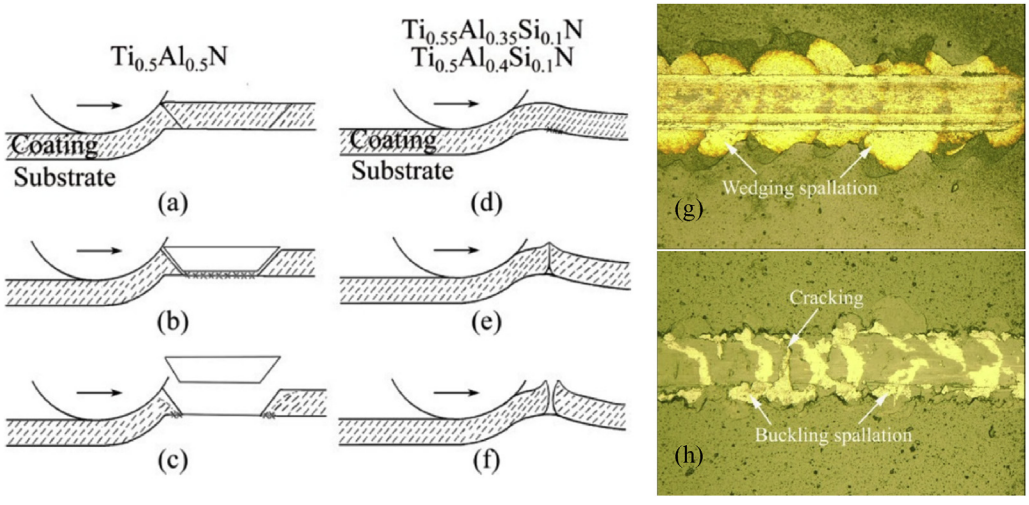

Fig. 4 – (a)–(f) Schematic of scratch failure modes for TiAlN and TiAlSiN coatings: (a)–(c) Wedging spallation of TiAlN coating. (d)–(f) Buckling spallation of TiAlSiN coating. Optical micrographs of the scratch tracks of (g) $Ti_{0.5}Al_{0.5}N$ and (h) $Ti_{0.5}Al_{0.4}Si_{0.1}N$ which show evidence of wedging and buckling spallation, respectively. Reprinted from Transactions of Nonferrous Metals Society of China, 26(6), Li-hui Zhu, Cheng Song, Wang-yang Ni, Yi-xiong Liu, Effect of 10% Si addition on cathodic arc evaporated TiAlSiN coatings, 1638–1646, Copyright (2016), with permission from Elsevier [82].

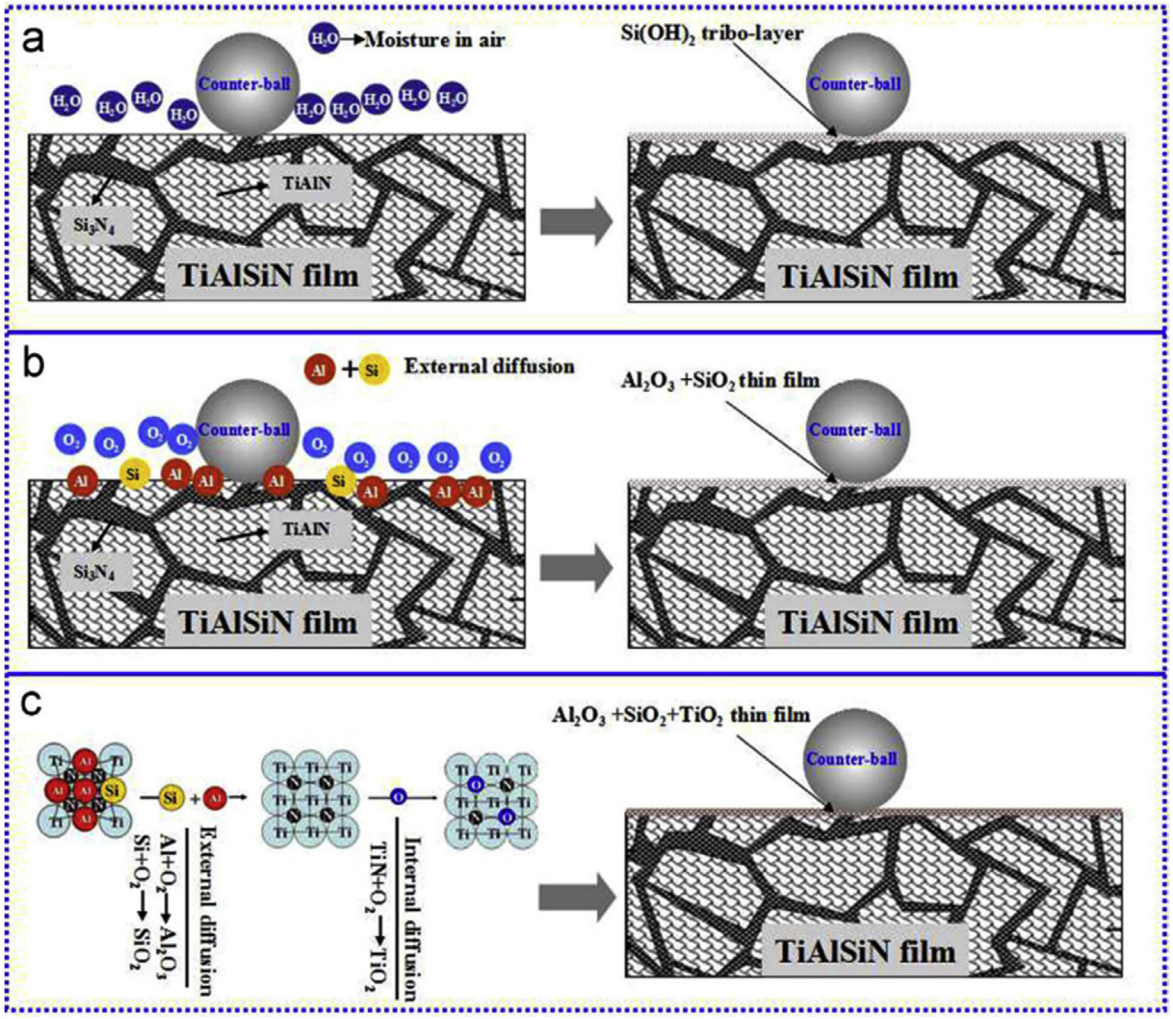

Fig. 5 – Schematic of (a) $SiO_2.nH_2O$ transfer film produced in the process of sliding at RT, (b) mixed Al_2O_3 and SiO_2 mixed oxide film formed at 600 °C, (c) Al_2O_3, SiO_2 and TiO_2 mixed oxide film produced at 800 °C. Reprinted from Tribology International, 98, Nairu He, Hongxuan Li, Li Ji, Xiaohong Liu, Huidi Zhou, Jianmin Chen, High temperature tribological properties of TiAlSiN coatings produced by hybrid PVD technology, 133–143, Copyright (2016), with permission from Elsevier [57].

room temperature were due to the formation of $SiO_2.nH_2O$ produced by the reaction of Si with moisture in the air. This explains the reduction in the COF with increasing Si content. At 600 °C, Al and Si atoms in the coating diffused to the surface to form a compact Al_2O_3 and SiO_2 mixed layer, enhancing the abrasive and adhesive wear resistance of the coating. At 800 °C, in addition to Al_2O_3 and SiO_2, low shear strength r-TiO_2 responsible for the low COF was also formed. Al_2O_3, SiO_2 and $Si(OH)_2$ were able to act as effective lubricants, resulting in a stable COF [55]. Tillmann & Dildrop [49] found that raising the temperature from 500 to 800 °C in the sliding tests increased the amount of SiO_2, leading to a marked reduction in wear. Increasing Si content in the coating resulted in greater SiO_2 formation, providing better wear protection for the coating. However, adding too much Si could result in the formation of excessive amorphous Si_3N_4, which was detrimental to wear resistance. If this effect exceeded the benefits produced by the SiO_2, an increase in wear would result. The COF of all coatings (with various Si contents) at 20, 500 and 800 °C was 0.7 ± 0.1. This showed that the Si content had no significant effect on the COF. The lower wear and friction properties of AlTiSiN coating compared to AlTiN could also be attributed to its high resistance to abrasion wear due to its high hardness in addition to the formation of a tribo-layer [86]. Nitrogen content was also found to have a pronounced effect on the mechanical properties, microstructure, and wear resistance of TiAlSiN coatings [87]. TiAlSi was found to possess an amorphous structure. By adding N into the coating using an f_{N2} (the ratio of nitrogen flow rate to the total flow rate) of 10%, a TiAlSiN coating consisting of nc-TiAlN/a-Si_3N_4 with the greatest hardness was produced. Increasing f_{N2} from 10 to 40% did not significantly change the elemental composition (N, Al, Ti, and Si) of the coating but resulted in an increase in grain size from 5 to 10 nm to 10–20 nm, the precipitation of AlN, and a further increase in H^3/E^2. The increased hardness and H^3/E^2 resulted in a significant improvement in wear resistance.

2.2. *Mechanical, thermal stability, oxidation and tribological behaviour of TiAlSiN multilayer coatings*

Multilayer coatings are developed to combine the best properties of the individual coatings. Therefore, multilayer coatings may simultaneously possess excellent hardness, oxidation resistance, toughness, and adhesion. The maximum hardness, H/E and H^3/E^2 of the TiAlSiN multilayer coatings (involving the use of TiAlSiN and other coatings) produced by various researchers ranged between 20.8 and 42.8 GPa, 0.0662–0.1119 and 0.1271–0.3883 GPa, respectively (Table 2), with means of 34.1 ± 6.1 GPa, 0.0885 ± 0.0132 and 0.2598 ± 0.0829 GPa. Xiao et al. [88] reported that AlCrN coatings exhibited the highest oxidation resistance. This was followed by AlCrN/TiAlSiN-2 (a multilayer coating with increasing AlCrN thickness towards the substrate), AlCrN/TiAlSiN-1 (a multilayer coating with fixed individual thickness) and TiAlSiN. The oxide formed on the AlCrN/TiAlSiN-2 was Al_2O_3, whereas the oxides formed on AlCrN/TiAlSiN-1 were Al_2O_3 and TiO_2. The results showed that the architecture of AlCrN/TiAlSNi-2 was more effective in preventing the outward diffusion of Ti to form TiO_2. It was suggested that the dense Al_2O_3 contributed substantially to the low wear rate of AlCrN/TiAlSiN-2. AlCrN had superior oxidation resistance due to its ability to form dense Al–Cr–O on the coating surface, which inhibited the inward diffusion of oxygen and the outward diffusion of metal elements. However, TiAlSiN with nanocrystal structure possessed greater hardness than AlCrN (Table 2). In sum, the multilayer coating with alternate layers of AlCrN and TiAlSiN had the combined properties of outstanding hardness and oxidation resistance.

Pei et al. [71] reported that the as-deposited TiAlSiN monolayer and TiAlN/TiAlSiN multilayer coatings had hardness values of 33.1 and 35.6 GPa, respectively (Table 2). The peak levels of hardness achieved in the annealing process at 1000 °C were 36.7 and 38.2 GPa for the TiAlSiN monolayer and TiAlN/TiAlSiN multilayer coatings, respectively. The TiAlN in the TiAlN/TiAlSiN multilayer coating stabilised the TiAlSiN layer in its metastable cubic structure based on epitaxial growth, which subsequently resulted in an increase in hardness. The TiAlN/TiAlSiN multilayer coating exhibited higher oxidation resistance than the TiAlSiN monolayer coating, which could be attributed to the retardation of oxygen diffusion by the numerous interfaces and the rapid formation of an Al-oxide layer due to its relatively high Al content. Similarly, Fukumoto et al. [89] found that a TiAlSiN/CrAlN multilayer coating possessed higher oxidation resistance than the TiAlSiN monolayer coating. This was because the addition of CrAlN to TiAlSiN increased the Al content in the coating, making more Al atoms available to form protective Al_2O_3 on the coating surface. The TiAlSiN/CrAlN multilayer coating with modulation period, $\Lambda = 5.5$ nm exhibited better oxidation resistance than that with $\Lambda = 12.3$ nm. Multilayer coatings with a smaller period and a uniform multilayer structure had more interfaces with defects or voids that acted as a barrier to the diffusion of oxygen and metal atoms. The multilayer coating with a smaller period retained excellent oxidation resistance even after annealing at 1000 °C with its nitride coating still intact. In contrast, the multilayer coating with $\Lambda = 12.3$ nm had thicker Ti-rich oxide layers, likely to be TiO_2, which accelerated the oxidation. The work by Parlinska-Wojtan et al. [90] suggested that a major contributor to the superior oxygen resistance of the TiAlSiN multilayer coating, consisting of Ti-rich and AlSi-rich alternate nano-layers, was the high diffusion rate of Al to the surface induced by the earlier formation of Al_2O_3 and TiO_2. Liu et al. [91] investigated the effect of Λ, in the range of 2–27 nm, on the mechanical properties of TiAlSiN/CrN multilayer coatings. Decreasing Λ from 27 to 7.5 nm increased both hardness, H/E and H^3/E^2 to their peak values due to the greater effectiveness of the multilayer structure in retarding dislocation motion. When $\Lambda = 8.5$ nm, the highest adhesion strength was achieved but at the cost of lower hardness, H/E and H^3/E^2. Therefore, Λ in the range of 7.5–8.5 nm was considered optimal for producing coatings with the combined properties of superior hardness, resistance to plastic deformation, and strength of adhesion (see Table 2). The properties of the multilayer coatings deteriorated significantly when Λ decreased to below 8.5 nm. This could be explained by the increased grain size of the columnar crystals due to a reduction in the amount of amorphous phase formed and the reduced inhibitory effect of the multilayer structures on the growth of columnar crystals. Liu et al. [92] investigated the wear and mechanical properties of AlTiSiN/AlCrSiN multilayer coatings consisting of rock salt structure of TiN and CrN and wurtzite structure of AlN, and with Λ ranging from 25–147 nm. All coatings had a similar chemical composition, as shown in Table 2. Reducing Λ from 147 to 60 nm led to an increase in hardness and elastic modulus up to their peak values due to the Hall-Petch effect. A decrease in these mechanical properties with the reduction in Λ from 60 to 25 nm was due to the formation of high numbers of droplet defects. The coating with the smallest Λ (=25 nm), which had the lowest residual compressive stress, exhibited the highest adhesion strength, toughness, and abrasive wear resistance.

Zhao et al. [45] investigated the wear and adhesion strength of mono and multilayer TiAlSiN coatings. The multilayer coatings, consisting of 2, 5, 7, and 10 alternate layers of TiAlSiN, had a fixed modulation ratio of 1:2 but different Λ of 0.18, 0.26, 0.36 and 0.90 μm, respectively (Table 2). The alternate layers of TiAlSiN (referred to as alternate layers A and B) were deposited at nitrogen pressures of 0.2 and 0.08 Pa, which gave rise to Si contents of 4.72 and 3.27 at.% Si, and hardness values of 41.4 and 33.7 GPa, respectively. The hardness, wear resistance, and adhesion strength of the TiAlSiN multilayer coatings increased as Λ decreased. All multilayer coatings exhibited higher adhesion strength than the TiAlSiN monolayer coatings, which had either a layer A or B coating. The wear rate of the multilayer coating with the smallest Λ (=0.26 μm) was about 1/8 of that of the A monolayer coating. Li et al. [46] investigated the performance of various types of TiAlSiN mono and multilayer coated cutting tools in the machining of Inconel 718 under dry conditions. The multilayer coatings, which consisted of 2, 4, and 8 alternate layers of TiAlSiN (referred to as alternate layers A and B, and deposited using bias voltages of −150 and −270 V, respectively), had a fixed modulation ratio of 1:2 but different values of Λ (2.100, 1.050 and 0.525 nm, respectively). The TiAlSiN monolayer coating had either layer A or B. Layer A had greater adhesion strength than layer B, whereas layer B had

Table 2 – Summary of the deposition method and parameters, substrate, description of coating, and hardness, Young's modulus, H/E and H^3/E^2 of TiAlSiN multilayer coatings.

Ref.	Deposition method	Substrate	Description of coating	Hardness (GPa)	Young's Modulus (GPa)	H/E	H^3/E^2 (GPa)	Remark
Kim et al. [43]	Cathodic arc plasma deposition	SKD 11 tool steel (EPMA, XRD and TEM characterization, nano-indentation), Si wafer (residual stress measurement)	TiAlSiN multilayer consisting alternate TiN/AlSiN deposited using AlSi cathode current (A) of:					
			35	42.8[a]				[a]estimated from Fig. 2 in ref. [43]
			43	38.5[a]				
			50	37.4[a]				
			55	36.2[a]				
			TiAlSiN multilayer consisting alternate TiN/AlSiN deposited using AlSi bias voltage (V) of:					
			−50	42.8[b]				[b]estimated from Fig. 4 in ref. [43]
			−100	38.0[b]				
			−150	36.7[b]				
			−200	37.2[b]				
Zhao et al. [45]	Plasma immersion ion implantation	WC-8 wt.% Co (SEM, EDX, XRD and TEM characterization, nano-indentation, scratch and ball-on-disc tests)	TiAlSiN (high hardness) deposited at 0.2 Pa nitrogen	41.4[c]	457.0[c]	0.0907	0.3405	[c]estimated from Fig. 5 in ref. [45]
			TiAlSiN (low hardness) deposited at 0.08 Pa nitrogen	33.7[c]	392.5[c]	0.0859	0.2487	
			Multilayer coatings consisting alternate high and low-hardness TiAlSiN layers with Λ (μm) of:					
			0.18	37.5[c]	405.3[c]	0.0913	0.3084	
			0.26	37.0[c]	400.0[c]	0.0925	0.3166	
			0.36	37.0[c]	415.8[c]	0.0889	0.2930	
			0.90	33.3[c]	357.9[c]	0.0931	0.2888	
Li et al. [46]	High power impulse magnetron sputtering (HiPIMS)	WC-CO tool inserts (SEM, EDX and XRD characterization, nano-indentation, scratch test, machining)	TiAlSiN with high adhesion deposited using −150 V (layer A)	23.1	398	0.0581	0.0779	
			TiAlSiN with high hardness deposited using −270 V (layer B)	47.9	929	0.0516	0.1273	
			TiAlSiN multilayer (bilayers of A and B)	27.5	456	0.0603	0.1003	
			TiAlSiN multilayer (4 alternate layers of A and B)	27.8	437	0.0636	0.1123	
			TiAlSiN multilayer (8 alternate layers of A and B)	29.6	377	0.0786	0.1829	
Sui et al. [52]	Reactive magnetron sputtering	WC-8 wt.% Co (SEM, EDX, XRD, TEM and XPS characterization, nano-indentation, scratch test, machining)	TiAlN	16.7				
			TiAlSiN	22.0				
			TiAlN/TiAlSiN	20.8				

Pei et al. [71]	Cathodic arc deposition	WC-6 wt.% Co (SEM and EDX characterization), W (nano-indentation), low-alloy steel (XRD characterization), polycrystalline Al_2O_3 plates (oxidation test)	$Ti_{0.52}Al_{0.48}N$	29.1	475.0	0.0613	0.1092	
			$Ti_{0.53}Al_{0.38}Si_{0.09}N$	33.1	395.6	0.0837	0.2317	
			$Ti_{0.52}Al_{0.48}N/Ti_{0.53}Al_{0.38}Si_{0.09}N$	35.6	473.2	0.0752	0.2015	
Chen et al. [73]	Cathodic arc evaporation	WC-6 wt.% Co and WC-10 wt.% Co tools (EPMA, SEM and XRD characterization, nano-indentation, machining)	TiAlN monolayer	31.2				
			TiAlSiN monolayer	42.4				
			TiAlN/TiAlSiN multilayer	39.8				
Ma et al. [83]	Multi-arc ion plating	TC18 (Ti5Al5Mo5V1CrFe) alloy (FESEM, EDX, XRD and XPS characterization, nano-indentation, scratch and ball-on-disc tests)	TiAlSiN monolayer	24.7	379.1	0.0652	0.1049	
			TiN/TiAlSiN multilayer	26.3	366.5	0.0718	0.1354	
Xiao et al. [88]	Cathodic arc deposition	Cemented carbide (SEM, EDX and XRD characterization, nano-indentation, scratch and ball-on-disc tests), single crystalline Al_2O_3 (oxidation test)	AlCrN monolayer	27.5[d]	394.4[d]	0.0697	0.1337	[d]estimated from Fig. 4 in ref. [88]
			TiAlSiN monolayer	40.8[d]	483.3[d]	0.0844	0.2908	
			AlCrN/TiAlSiN-1 (alternate layer of AlCrN and TiAlSiN with increasing AlCrN thickness towards the substrate)	38.3[d]	452.8[d]	0.0846	0.2740	
			AlCrN/TiAlSiN-2 (alternate layer of AlCrN and TiAlSiN with fixed individual thickness)	39.2[d]	466.7[d]	0.0840	0.2766	
Liu et al. [91]	High power pulsed magnetron sputtering	Si (100) wafer (FESEM, TEM, GIXRD and XPS characterization), WC-10 wt% Co (nano-indentation, scratch test)	TiAlSiN/CrN with modulation period Λ (nm) of:					
			2.0	19.9[e]	261[e]	0.0762	0.1157	[e]estimated from Fig. 6 in ref. [91]
			3.0	23.3[e]	291[e]	0.0801	0.1494	
			4.5	22.1[e]	257[e]	0.0860	0.1634	
			7.5	26.6[e]	295[e]	0.0902	0.2163	
			8.5	24.9[e]	314[e]	0.0793	0.1566	
			11.0	22.1[e]	257[e]	0.0860	0.1634	
			27.0	20.9[e]	225[e]	0.0929	0.1803	
Liu et al. [92]	Arc ion plating	Si wafers (001) (SEM, EDX, XPS and TEM characterization), 304 stainless steels (XRD characterization), cemented carbides (nano-indentation, scratch and ball-on-disc tests)	AlTiSiN/AlCrSiN with modulation period Λ (nm) of:					
			25 ± 1.8	29.0[f]	438[f]	0.0662	0.1271	[f]estimated from Fig. 8(a) in ref. [92]
			60 ± 2.2	31.6[f]	514[f]	0.0615	0.1194	
			73 ± 3.9	25.9[f]	411[f]	0.0630	0.1029	
			96 ± 5.0	24.9[f]	399[f]	0.0624	0.0970	
			147 ± 9.8	23.9[f]	384[f]	0.0622	0.0926	

(*continued on next page*)

Table 2 – (*continued*)

Ref.	Deposition method	Substrate	Description of coating	Hardness (GPa)	Young's Modulus (GPa)	H/E	H^3/E^2 (GPa)	Remark
Chen et al. [94]	Cathodic vacuum arc	Si (100) wafers (SEM, EDX, XRD, XPS and TEM characterization), high-speed steels (nano-indentation, ball-on-disc test)	CrAlN/TiAlSiN deposited using substrate bias voltage (V) of:					
			−50	30.8	324.5	0.0949	0.2775	
			−80	34.1	362.4	0.0941	0.3019	
			−120	35.4	377.6	0.0938	0.3111	
Zhang et al. [95]	Cathodic arc evaporation	WC-6 wt.% Co (SEM, EDX and TEM characterization, nano-indentation), low-alloy steel foils (XRD characterization), W plates (thermal annealing study), Si stripes (residual stress measurement), polycrystalline Al_2O_3 sheets (SEM and EDX characterization, oxidation test)	TiAlTaN monolayer	32.4	457.6	0.0708	0.1624	
			TiAlSiN monolayer	36.5	458.2	0.0797	0.2316	
			TiAlTaN/TiAlSiN multilayer	36.7	445.9	0.0823	0.2486	
Chang et al. [96]	Cathodic arc evaporation	Polished Silicon (FESEM, TEM, EPMA and XRD characterization, nano-indentation)	TiAlSiN monolayer	38	425	0.0894	0.3038	
			TiAlSiN/TiN multilayer	36	380	0.0947	0.3231	
Li et al. [97]	High power impulse magnetron sputtering (HiPIMS)	Cemented carbide inserts (SEM and XRD characterization, nano-indentation, scratch test)	TiAlSiN monolayer	34	367	0.0926	0.2918	
			TiSiAlN/Ti multilayer with Ti thickness (nm) of:					
			25	31	277	0.1119	0.3883	
			50	27	286	0.0944	0.2406	
			100	24	265	0.0906	0.1969	
			150	19	227	0.0837	0.1331	

higher hardness. Therefore, the hardness and adhesion strength of the multilayer coatings fell somewhere between those of the monolayer coatings (Table 2). The adhesion strength for the multilayer coatings was found to increase with the number of layers and to reach a maximum value in the coating with 8 layers. The 8-layer coating had comparatively more interfaces to retard crack propagation and a smaller period, which functioned more effectively in obstructing dislocation motion. As a result, a higher critical load was required to generate spallation of the coating. The 8-layer coating was also found to have the highest, H/E, H^3/E^2 and toughness. This high toughness could be attributed to the inhibition of crack propagation by the high number of interfaces and the residual stress in the coating. Machining tests on Inconel 718 showed that the 8-layer coated tools with combined superior adhesion strength and hardness, and the highest H/E and H^3/E^2 exhibited the longest tool life. Similarly, high fracture resistance due to the presence of nc-TiN/a-Si_3N_4 and the deflection of cracks at the interfaces have been used to explain the superior performance of the cutting tools coated with (Ti,Si)N/(Ti,Al)N nano-layers in the dry machining of steel [93].

Kim et al. [43] investigated the effect of AlSi cathode arc current and substrate bias voltage on the hardness and compressive stress of TiAlSiN. The TiAlSiN coatings had alternate layers of nanocrystalline TiN and hexagonal AlSiN. Hardness and compressive stress were found to increase with decreasing AlSi cathode arc current and bias voltage (Table 2). The coating with the highest hardness was found to have the smallest Λ and sharp interfaces (indicating that TiN and AlSiN had minimal intermixing at the interfaces) which were effective in impeding dislocation. Therefore, the hardness of the coatings was not governed solely by compressive stress and Λ but also by the nature of the interface generated. Chen et al. [94] studied the effect of the substrate bias voltage on the mechanical and tribological properties of CrAlN/TiAlSiN nano-multilayer coating containing alternate layers of fcc-(Cr,Al)N and nanocrystalline (Ti,Al)N phases embedded in the amorphous matrix. Higher substrate bias voltages produced coatings with higher wear resistance and a lower COF during sliding on WC/Co. These results could be attributed to the coating's high hardness (Table 2) and fracture toughness, and also the formation of a tribo-film rich in Cr, Al, Ti, and O elements.

Zhang et al. [95] found that the TiAlTaN/TiAlSiN multilayer coating had higher hardness in comparison to TiAlTaN and TiAlSiN monolayer coatings (Table 2). This was due to grain size refinement and the generation of greater micro-strain by the strengthening effect of the coherent interfaces in the multilayer coating. The multilayer coating also had lower compressive stress which could be due to the relaxation of stress at the interfaces. The thermal stability of the multilayer coating was similar to that of the TiAlSiN coating but was better than that of the TiAlTaN monolayer coating. As shown in Fig. 6, the change in the magnitude of the hardness of TiAlTaN/TiAlSiN coating with annealing temperature was comparable to TiAlSiN. The multilayer coating exhibited higher oxidation resistance than the monolayer coatings, benefiting from the synergic effect of Ta and Si in inhibiting the transformation of a-TiO_2 to r-TiO_2 phase. The coherent

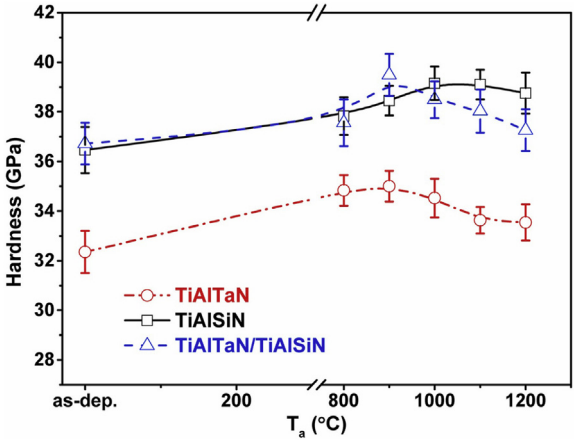

Fig. 6 – Hardness of TiAlTaN and TiAlSiN monolayer, and TiAlTaN/TiAlSiN multilayer coatings as a function of annealing temperature. Reprinted from Vacuum, 187, Jie Zhang, Li Chen, Yi Kong, Chun Hu, Zheren Liu, Yong Du, Shuyan Zhang, Microstructure, mechanical and thermal properties of TiAlTaN/TiAlSiN multilayer, 110138, Copyright (2021), with permission from Elsevier [95].

interfaces and the refined columnar grain in the multilayer coating were also able to retard oxygen diffusion. The oxidation onset temperatures of TiAlSiN, TiAlTaN, and TiAlTaN/TiAlSiN were 915, 954, and 1043 °C, respectively.

Chen et al. [73] attributed the excellent adhesion strength of the TiAlN/TiAlSiN multilayer coating to stress relaxation at the coating interfaces during their growth and to crack deflection at the coating interfaces. In the milling of 42CrMo steel, where tools were subject to impact, the multilayer coated tools with better adhesion strength exhibited longer life than the TiAlSiN monolayer coated tool. Ma et al. [83] reported that the relatively high hardness, H/E and H^3/E^2 ratio of TiN/TiAlSiN multilayer coating, as compared to the TiAlSiN coating (Table 2), was due to the retardation of dislocation movement by the numerous interfaces therein. The multilayer coating which demonstrated higher wear resistance and adhesion strength, exhibited buckling as its failure mode in the scratching test. In contrast, the monolayer coating's failure mode was wedging spallation. Similarly, Chang et al. [96] found that the TiAlSiN/TiN multilayer coating had lower residual stress than the gradient TiAlSiN coating (with chemical composition varying from $Ti_{0.50}Al_{0.43}Si_{0.07}N$ at the surface to $Ti_{0.67}Al_{0.28}Si_{0.05}N$ near the substrate) due to the stress-relaxation effect. The multilayer coating also showed greater resistance to plastic deformation with a higher H/E and H^3/E^2 but slightly lower hardness as compared to TiAlSiN (Table 2). Sui et al. [52] found that TiAlN/TiAlSiN multilayer coating, consisting of a mixture of the columnar and nanocrystal structures, had lower hardness but higher adhesion than TiAlSiN monolayer coating (with nanocrystal structure) and also higher hardness but slightly lower adhesion strength than TiAlN monolayer coating (with columnar structure) (Table 2). In the high-speed turning of titanium with coolant, the TiAlSiN monolayer coated tools performed better than

TiAlN monolayer and TiAlN/TiAlSiN multilayer-coated tools. This was due to the TiAlSiN coating's higher hardness and oxidation resistance owing to the retardation of oxygen diffusion by its fine nanocrystalline structure.

Li et al. [97] found that the thickness of the Ti interlayer could influence the mechanical and tribological properties of TiAlSiN coatings. The hardness and elastic modulus of the TiAlSiN/Ti multilayer coating decreased with increasing thickness of the Ti interlayer (Table 2). The TiAlSiN/Ti multilayer coatings exhibited higher fracture toughness than the TiAlSiN coating due to crack deflection at the interfaces and the weakening of crack propagation by the soft Ti interlayer. The highest H/E and H^3/E^2 was obtained for the coating with the thinnest (25 nm) Ti interlayer. Fracture toughness decreased with increasing Ti interlayer thickness, which was due to greater plasticity mismatch (i.e. the difference in the severity of deformation of the soft Ti and hard TiAlSiN layers) and interlayer stress difference. Cutting tests carried out on Inconel 718 under wet conditions revealed that the cutting performance of TiAlSiN coated tools was enhanced by the Ti interlayer. Among all the mono and multilayer-coated tools, the TiAlSiN/Ti multilayer-coated tools with the thinnest Ti interlayer of 25 nm exhibited the lowest flank wear progression. The wear resistance of TiAlSiN multilayer coatings could be improved by using suitable adhesion and intermediate coating layers [98]. The T1 (TiN adhesion layer + $Al_{17.5}Ti_{80-}Si_{2.5}N$ intermediate layer + $Al_{52}Ti_{39}Si_9N$ top layer) and T2 coatings ($Al_{33}Ti_{67}N$ adhesion layer + $Al_{43}Ti_{54}Si_3N$ intermediate layer + $Al_{54}Ti_{36}Si_{10}N$ top layer) as shown in Fig. 7 had lower cohesion strength and resistance to delamination. The T3 coating ($Al_{67}Ti_{33}N$ adhesion layer + $Al_{64}Ti_{34}Si_2N$ intermediate layer + $Al_{53}Ti_{38}Si_9N$ top layer) with the lowest residual stress possessed the highest cohesion and adhesion properties, and provided the highest protection for the cutting tool in the milling of grey cast iron HT250. It had a relatively low residual stress because it had a more uniform CTE (coefficient of thermal expansion) resulting from the uniformly distributed Al content across the coating layers. In contrast, T1 coating, with the highest difference in the Al distribution across the coating layers, had the highest residual stress and the lowest adhesion property. The difference in the lattice constant a and micro-strain at the interface between the intermediate and adhesion layers was the primary reason for the poor adhesion of the T2 coating architecture.

3. Review of TiAlCrN coatings

3.1. *Mechanical, thermal stability, oxidation and tribological behaviour of TiAlCrN monolayer coatings*

The effect of Cr content on the mechanical properties of TiAlN coatings is summarised in Table 3. Zhou et al. [99] and Xu et al. [100] reported that increases in both the hardness and Young's modulus of TiAlCrN were due to increased internal stress and lattice distortion caused by Cr in the (Ti,Al)N crystals. An optimum Cr content that gave rise to the maximum hardness (and above which hardness was reduced) was identified [99]. Similarly, Sui et al. [101] found that the hardness of TiAlCrN decreased with greater Cr content. This could be due to the generation of excessive soft CrN phase, an increase in the particle size of the coating, and the oblique growth of the porous coating [99,101].

As shown in Figs. 8 and 9, and Table 3, the maximum hardness, H/E and H^3/E^2 of the TiAlCrN coatings produced using various deposition processes and chemical compositions were observed to range between 26.0 and 40.9 GPa, 0.0625–0.1252 and 0.1085–0.3616 GPa, respectively, with means of 32.1 ± 4.7 GPa, 0.0760 ± 0.0132 and 0.2146 ± 0.1073 GPa [99,101–106]. However, only in the study conducted by Lin et al. [106] was it shown that increased Cr content produced a significant increase in hardness. The results produced by Beake et al. [103] showed a correlation between H/E, H^3/E^2, COF and the critical load for coating failure in the scratch test. $Ti_{0.25-}Al_{0.65}Cr_{0.1}N$ had the highest H/E and H^3/E^2, and this was followed by $Al_{0.67}Ti_{0.33}N$ and $Ti_{0.1}Al_{0.7}Cr_{0.2}N$ (see Table 3). The highest critical load for coating failure, and the lowest COF and level of wear progression were measured for $Ti_{0.25}Al_{0.65}Cr_{0.1}N$ with the highest H/E and H^3/E^2. The lowest critical load was measured for $Ti_{0.1}Al_{0.7}Cr_{0.2}N$ with the lowest H/E and H^3/E^2.

Cr had a significant effect on the hardness of TiAlCrN during annealing. Xu et al. [100] reported that when annealed at 900 °C, Cr promoted the spinodal decomposition of Ti–Al–N to form Al-depleted and Al-enriched domains, which were responsible for the increase in the coating's hardness. Above this temperature, hardness was lower due to the coarsening of phases and the formation of wurtzite (w-AlN) [107]. Cr also delayed the formation of w-AlN, during annealing, which was responsible for the reduction in the hardness

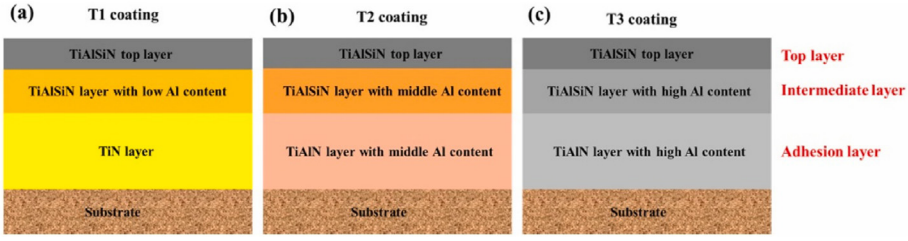

Fig. 7 – TiAlSiN coatings with different multilayer structures (a) T1 (b) T2 and (c) T3 coating. Reprinted from Wear, 488–489, Fei Cai, Jinmin Wang, Qi Zhou, Shihong Zhang, Jun Zheng, Qimin Wang, Kwangho Kim, Reduced delamination and improved cutting performance of TiAlSiN multilayer coated cutter by tailoring the adhesion layers and intermediate layers, 204135, Copyright (2022), with permission from Elsevier [98].

Table 3 – Summary of the deposition method and parameters, substrate, nominal composition, and hardness, Young's modulus, H/E and H^3/E^2 of TiAlCrN monolayer coatings.

Ref.	Deposition method	Substrate	Bias voltage (V)	Nominal composition/ Description of coating	Cr content (at.%)	Hardness (GPa)	Young's Modulus (GPa)	H/E	H^3/E^2 (GPa)	Remark
Zhou et al. [99]	High power impulse magnetron sputtering and DC magnetron sputtering	Si wafers (SEM, EDX and XRD characterization), polished stainless steel (nano-indentation, ball-on-disc test)	Constant at −100		0	31.4[a]	448.8[a]	0.0699	0.1537	[a]estimated from Fig. 6 in ref. [99]
					8.9	33.7[a]	469.5[a]	0.0717	0.1736	
					16.4	28.6[a]	452.5[a]	0.0632	0.1143	
					21.4	21.0[a]	397.5[a]	0.0528	0.0586	
					24.3	18.9[a]	390.0[a]	0.0485	0.0444	
Xu et al. [100]	Cathodic arc system	Low-alloy steel (SEM, EPMA and XRD characterization, thermal annealing study), WC-6 wt.% Co (nano-indentation), poly-crystalline Al_2O_3 plates (SEM characterization, oxidation test), WC −6 wt.% Co inserts (machining)	Constant at −100	$Ti_{0.52}Al_{0.48}N$		31.2	380.3	0.0820	0.2099	
				$Ti_{0.44}Al_{0.50}Cr_{0.06}N$		34.4	360.7	0.0953	0.3129	
Sui et al. [101]	Magnetron sputtering	Si (100) wafer (GIXRD, SEM, EDX and XPS characterization, oxidation test), WC-8 wt.% Co (nano-indentation)	Constant at −120	$Ti_{0.32}Al_{0.38}Cr_{0.30}N$		26[b]				[b]estimated from Fig. 4 in ref. [101]
				$Ti_{0.22}Al_{0.27}Cr_{0.51}N$		21[b]				
				$Ti_{0.17}Al_{0.19}Cr_{0.64}N$		20[b]				
Forsén et al. [102]	Reactive cathodic arc evaporation	Polished WC-Co (SEM, EDX, XRD and TEM characterization, nano-indentation), Fe foils (thermal response study)	Constant at −40	$Ti_{0.52}Cr_{0.01}Al_{0.47}N$		32.7[c]				[c]estimated from Fig. 6 in ref. [102]
				$Ti_{0.31}Cr_{0.07}Al_{0.62}N$		31.1[c]				
				$Ti_{0.31}Cr_{0.17}Al_{0.52}N$		32.9[c]				
Beake et al. [103]	R&D-type hybrid PVD coater	Mirror polished H10A WC-Co (SEM and EDX characterization, nano-indentation, micro-scratch test)	Constant at −100	$Al_{0.67}Ti_{0.33}N$		25.6	413	0.0620	0.0983	
				$Ti_{0.25}Al_{0.65}Cr_{0.10}N$		27.8	445	0.0625	0.1085	
				$Ti_{0.10}Al_{0.70}Cr_{0.20}N$		27.5	467	0.0589	0.0954	

(*continued on next page*)

Table 3 – (*continued*)

Ref.	Deposition method	Substrate	Bias voltage (V)	Nominal composition/ Description of coating	Cr content (at.%)	Hardness (GPa)	Young's Modulus (GPa)	H/E	H^3/E^2 (GPa)	Remark
Yamamoto et al. [104]	Arc ion plating with plasma enhanced arc cathodes	Mirror-polished WC-Co (XPS, XRD and TEM characterization, micro-indentation, thermal annealing study)	Constant at −150	$Ti_{0.26}Cr_{0.10}Al_{0.64}N$ $Ti_{0.27}Cr_{0.11}Al_{0.62}N$ $Ti_{0.11}Cr_{0.22}Al_{0.67}N$ $Ti_{0.10}Cr_{0.24}Al_{0.66}N$		27 29 27 29				
Georgiadis et al. [105]	Cathodic arc evaporation	Hot work H13 steels (SEM, EDX and XRD characterization, nano-indentation, scratch and ball-on-disc tests)	Constant at −50	$Cr_{0.12}Ti_{0.07}Al_{0.39}N$ $Cr_{0.11}Ti_{0.19}Al_{0.31}N$ $Cr_{0.23}Ti_{0.13}Al_{0.22}N$ $Cr_{0.29}Ti_{0.08}Al_{0.15}N$ $Cr_{0.51}Ti_{0.04}Al_{0.08}N$		27.8 34.5 30.2 30.1 29.9	260.1 275.5 271.4 256.5 243.0	0.1069^{+} 0.1252^{+} 0.1113^{+} 0.1173^{+} 0.1230^{+}	0.3176^{+} 0.5410^{+} 0.3739^{+} 0.4145^{+} 0.4527^{+}	$^{+}$Calculated based on E*
Lin et al. [106]	Closed field unbalanced magnetron sputtering	AISI 304 stainless steel (SEM, EDX and XRD characterization, nano-indentation, scratch and ball-on-disc tests, oxidation test)	Constant at −60	$Cr_{0.66}Al_{0.34}N$ $Cr_{0.65}Ti_{0.05}Al_{0.30}N$ $Cr_{0.61}Ti_{0.10}Al_{0.29}N$ $Cr_{0.58}Ti_{0.13}Al_{0.29}N$ $Cr_{0.54}Ti_{0.20}Al_{0.26}N$ $Cr_{0.48}Ti_{0.28}Al_{0.24}N$ $Cr_{0.43}Ti_{0.40}Al_{0.17}N$ $Cr_{0.33}Ti_{0.53}Al_{0.14}N$ $Cr_{0.26}Ti_{0.64}Al_{0.10}N$	35.2 35.0 32.4 30.8 29.1 24.5 22.4 16.9 12.7	28.5^{d} 34.4^{d} 40.9^{d} 35.8^{d} 34.0^{d} 32.9^{d} 30.4^{d} 30.0^{d} 29.3^{d}	330^{d} 370^{d} 435^{d} 395^{d} 375^{d} 365^{d} 355^{d} 360^{d} 360^{d}	0.0864 0.0929 0.0940 0.0907 0.0907 0.0902 0.0855 0.0833 0.0813	0.2126 0.2963 0.3616 0.2943 0.2795 0.2675 0.2220 0.2083 0.1935	^{d}estimated from Fig. 5 in ref. [106]
Yamamoto et al. [112]	Plasma enhanced type of arc-cathode	Mirror polished WC-Co inserts (SEM, EDX, TEM and XRD characterization, micro-indentation), platinum foils (oxidation test), carbide ball-nose end mills (machining)	−0 −25 −50 −100 −150 −200	Hexagonal TiCrAlN Hexagonal TiCrAlN Cubic TiCrAlN Cubic TiCrAlN Cubic TiCrAlN Cubic TiCrAlN		17.5^{e} 27.5^{e} 33.0^{e} 34.0^{e} 35.0^{e} 34.0^{e}				^{e}estimated from Fig. 8 in ref. [112]
Zhang et al. [113]	Multi-arc ion plating	High speed steel (SEM, EDX and XRD characterization, micro-indentation, scratch and thermal shock tests)	−100 −150 −200 −250	TiAlCrN TiAlCrN TiAlCrN TiAlCrN	19.80 20.62 29.30 31.70	27.46 50.01 45.60 45.60				

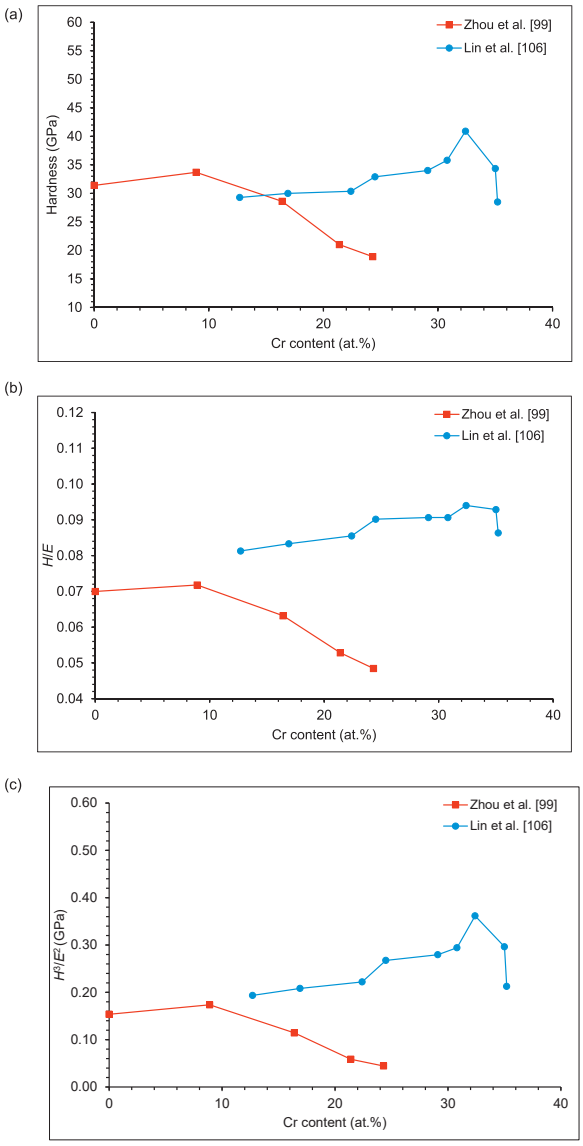

Fig. 8 – Comparison of the (a) hardness, (b) *H/E* and (c) H^3/E^2 ratio measured for TiAlCrN coatings deposited by various deposition techniques as a function of Cr content (at.%).

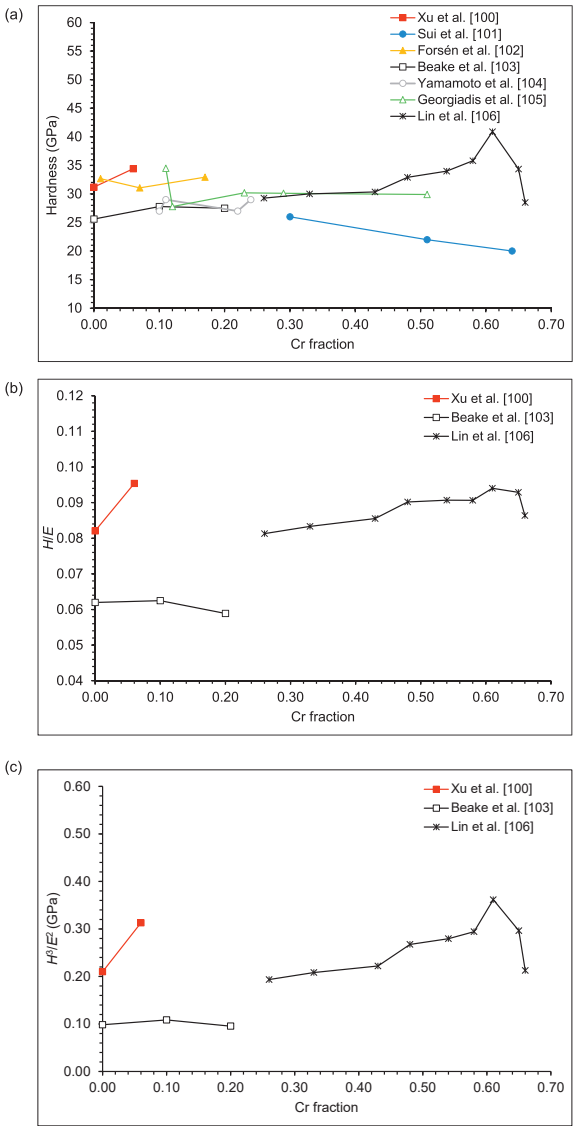

Fig. 9 – Comparison of the (a) hardness, (b) *H/E* and (c) H^3/E^2 ratio measured for TiAlCrN coatings deposited by various deposition techniques as a function of Cr fraction (Nominal composition).

[102,108]. Similarly, Yamamoto et al. [104] found that the c-TiCrAlN films maintained their NaCl-type structure up to 900 °C before partially transforming into h-(TiCrAl)N, resulting in a reduced hardness.

Researchers have observed different mechanisms by which Cr and Al led to improved oxidation resistance of TiAlCrN. Cr was found to promote the formation of dense Cr_2O_3 and Al_2O_3 oxide layers, which were effective in inhibiting the diffusion of oxygen into the coating [109]. It also retarded the transformation of metastable a-TiO_2 into stable r-TiO_2, and thereby the growth of a porous Ti-oxide rich sublayer [100]. Both Cr and Al promoted the formation of a dense oxide scale which retarded the diffusion of titanium and hence the growth of porous TiO_2 on the surface. Porous TiO_2 was undesirable as it had a high tendency to crack, thereby accelerating the oxidation process [110]. Ru et al. [111] found that the preferential diffusion of Al to the outer surface of TiAlCrN to form Al_2O_3 impeded further oxidation via inward diffusion of oxygen to form Cr_2O_3 and TiO_2 at the subsurface. Oxidation resistance improved with greater chromium content [101]. The oxide on the $Ti_{0.32}Al_{0.38}Cr_{0.30}N$ coating changed from a dense Al-rich oxide layer at 800 °C to a loose and porous Ti–Al rich oxide layer at 1000 °C, which severely degraded the oxidation resistance of the coating. However, the $Ti_{0.17}Al_{0.19}Cr_{0.64}N$ coating with a higher Cr content had a Ti–Al rich oxide layer on top and a dense and continuous Cr–Al rich oxide layer at the bottom. This coating exhibited better oxidation resistance because the presence of the Cr–Al rich oxide layer suppressed the diffusion rate of Ti atoms to the surface while preventing oxygen atoms from diffusing into the interior.

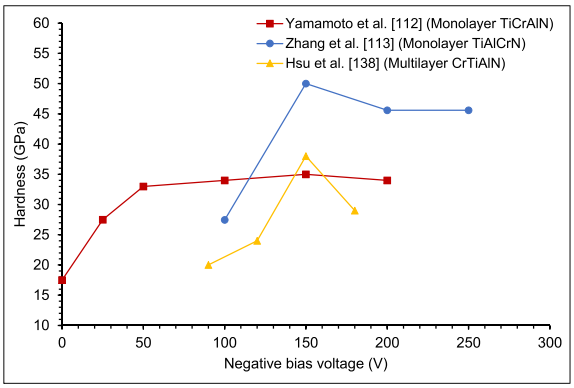

Fig. 10 – Variation in the hardness of the monolayer TiAlCrN and multilayer CrTiAlN coatings with negative bias voltages.

Yamamoto et al. [112] observed a change in the chemical composition and microstructure of $(Ti_xCr_y,Al_z)N$ with the magnitude of the applied substrate bias. The coating studied had the high Al ratio (i.e. z value) of 0.7. Below 50 V, only hexagonal phase was detected in the coating whereas the coating deposited above 50 V had a cubic phase which gave rise to a greater hardness. As the bias voltage was increased from 0 to 200 V, the Al ratio decreased while the Ti ratio (i.e. x value) increased. No significant change in the Cr ratio (y value) was observed. Cubic phase was achievable up to $z = 0.73$ (Al ratio). The transition between the cubic and hexagonal phase for $(Ti_{1-z}Al_z)N$ was observed at lower z values of between 0.4 and 0.67. The oxidation onset temperature for TiAlCrN was found to be 1000 °C, which was between 100–150 °C higher than that of the TiAlN coating. In the high-speed milling of hardened AISI H13 die-steel under dry conditions, the TiCrAlN coated tools, with a combination of high hardness and oxidation resistance, outperformed the TiAlN coated tools. Zhang et al. [113] investigated the effect of the bias voltage on the properties of TiAlCrN coatings with N-gradient distribution. N-gradient distribution, produced by raising the N_2 partial pressure step-by-step during deposition, had the advantage of limiting the accumulation of growth stress and thus enhancing the adhesive strength of the coating. Increasing the bias voltage from −100 to −250 V produced the same dense columnar microstructure, despite causing a change in the chemical composition (i.e. reduced Al content and greater Cr content) (Table 3). The highest hardness, adhesive strength, and thermal shock resistance were achieved at 150 V. The change in the coating's hardness with negative bias voltage is shown in Fig. 10, with the maximum value obtained within the range of 35.0–50.0 GPa, with a mean of 42.5 GPa.

TiAlCrN had a high tendency to form a tribo-film which was effective in suppressing wear. Tu et al. [114] reported that the formation of Cr_2O_3 during machining improved the wear resistance of TiAlCrN coated tools. This result was in accordance with the earlier finding by Warcholinski et al. [115], which showed that Cr reduced the COF and the wear rate of TiAlCrN. Fox-Rabinovich et al. [116] found that in milling AISI H13 steel under dry conditions, the superior wear resistance of the TiAlCrN coated tools was due to both reduced COF at the chip–tool interface and adhesive wear by the formation of protective alumina and lubricious chromia. As a result, these tools exhibited lower flank wear than the TiAlN coated tools, and twice the tool life. Other research attributed the reduction in the COF and wear rate of TiAlCrN with increasing sliding speed to the formation of tribo-films [117]. Another study showed that the reduction in the COF of AlTiCrN coatings with increasing Cr content at 400 °C could be attributed to the formation of chromic-oxide tribo film [99]. Fox-Rabinovich et al. [118] found that the strong Al–Cr metallic bonds enhanced the hot hardness and oxidation resistance of TiAlCrN, making TiAlCrN a suitable coating material for cutting tools which could inhibit the intensive oxidation and thermal softening often found to occur in high-speed machining. Another machining test carried out on the grey cast iron under dry conditions demonstrated that TiAlCrN coated tools suffered less wear progression than TiAlN coated tools, and that this improved wear resistance with increasing Cr content was due to the enhancement of oxidation resistance [119,120]. Xu et al. [100] attributed the superior performance of TiAlCrN coating (as compared to TiAlN) in providing wear protection for cutting tools in the continuous cutting of stainless steel to its high *H/E*. In the milling of hardened tool steel H13, the $Ti_{10}Al_{70}Cr_{20}N$ coated tool with higher hot hardness, oxidation stability, and stiffness outperformed the $Al_{67}Ti_{33}N$ coated tool. However, in the milling of TiAl6V4 alloy and Ni-based super-alloy, $Al_{67}Ti_{33}N$ coated tool, with higher plasticity and impact fatigue fracture resistance, exhibited longer tool life [121].

Although TiAlCrN has a significantly higher hardness value (3033 HV) than TiAlN (1222 HV), the former coating exhibited lower wear resistance due to its lower adhesion strength [122]. Adhesion strength could be improved by reducing the residual compressive stress at the interface with an appropriate interlayer, known as a buffer layer. Chang et al. [123] found that, when compared to Ti and Cr, TiN and CrN interlayers resulted in lower compressive stress in AlTiCrN coatings, which in turn improved the adhesion strength and thus the impact resistance of the coating. Huang et al. [124] deposited an interfacial layer of Cr onto the substrate before the deposition of CrAlTiN coating in order to improve the adhesion of the coating.

Georgiadis et al. [105] found that the hardness of CrTiAlN increased with higher Ti/(Cr + Al) atomic ratio. The improved hardness was due to an increase in solid-solution hardening (due to lattice distortion by the Ti atoms in the lattice) and the growth of (111) lattice planes parallel to the substrate. However, the wear resistance of the coating at 400 °C was not governed by the hardness of the coating but rather its ability to form protective tribo-films at the worn region. Forsén et al. [125] found that increasing the Ti content in TiCrAlN coatings reduced the oxidation resistance due to the greater amount of TiO_2. However, the addition of Ti increased the stability of the TiCr- and Al-rich cubic phase and suppressed the formation and growth of hexagonal AlN precipitates. This explained the pronounced reduction in the hardness of $Ti_{0.01}Cr_{0.39}Al_{0.60}N$ at temperatures above 500 °C while the coating with a higher Ti content (namely $Ti_{0.33}Cr_{0.07}Al_{0.62}N$) retained its hardness up to

1100 °C. Lin et al. [106] studied the mechanical properties of $Cr_xTi_yAl_zN$ coating, and its resistance to oxidation and wear with various Ti fractions of between 5–64%. This coating exhibited a change in preferred orientation from (111), the most densely packed plane, to (311) at above 10% Ti. The coating with 10% Ti possessed the highest hardness, H/E, H^3/E^2, adhesion strength, and oxidation resistance, but the lowest COF and wear rate at both room temperature and at 600 °C. This superior hardness could be attributed to the combination of the solid-solution strengthening effect (substitution of Cr with Ti), as well as the dense microstructure of the (111) plane and the fine microstructure induced by its high Al content.

3.2. *Mechanical, thermal stability, oxidation and tribological behaviour of TiAlCrN multilayer coatings*

Experiments have been carried out to study the mechanical properties of multilayer coatings involving the use of TiAlCrN. The mechanical properties of various TiAlCrN architecture multilayer coatings are summarised in Table 4. A maximum hardness, H/E and H^3/E^2 of 19.8–38.4 GPa, 0.0422–0.1191 and 0.0353–0.5427 GPa are shown, with means of 31.3 ± 6.3 GPa, 0.0839 ± 0.0282 and 0.2706 ± 0.1984 GPa, respectively. Nakonechna et al. [126] attributed the high hardness of their TiAlN/TiAlCrN multilayer coatings to the formation of CrN hard fcc phase, the absence of wurtzite phase, and to the obstruction of dislocation motion by the layer interfaces. The Cr in the multilayer coating promoted the growth of columnar structure, which made cracking less likely to propagate, as indicated by the formation of discontinuous, short, and irregular cracks. Santana et al. [127] reported that the presence of Cr in the TiAlN/TiAlCrN multilayer coating promoted the formation of columnar structure and hard fcc-(Cr,Al)N phase over the softer wurtzite hcp(Al,Ti)N phase. Decreasing the Λ in the multilayer coating reduced interruption of columnar growth of TiAlCrN layers by the TiAlN layers, which promoted the formation of highly columnar films. The high hardness of the multilayer coating could be attributed to the obstruction of dislocation motion by the numerous interfaces and the formation of columnar structures with preferred orientation in the (111) plane.

In the high-speed milling of AISI H13 tool steel under dry conditions, TiAlCrN/NbN nano-multilayer coated tools exhibited longer tool life than the TiAlCrN monolayer coated tools, and the other transition metal nitrides-content (such as TiAlCrN/TaN, TiAlCrN/CrN and TiAlCrN/WN) nano-multilayer coated tools (Fig. 11) [128,129]. The TiAlCrN/NbN coating with 3.81 at.% Nb outperformed those with 1.75 and 9.28 at.% Nb. It was found that the Al_2O_3, Cr_2O_3 and Nb–O (namely, NbO and Nb_2O_5) tribo-films, formed on the TiAlCrN/NbN coatings, worked in synergy respectively to insulate the surface from thermal wear, to lubricate the cutting zone to reduce friction, and to dissipate energy to reduce tool edge damage. However, when the cutting temperature exceeded 1100 °C, the product of the oxidation was non-protective rutile. As a result, intensive seizures occurred, and crater wear started to develop at the exposed substrate. The oxides formed on TiAlCrN/WN multilayer coated tools were lubricious W–O and alumina. These oxides resulted in lower cutting forces and temperature, and inhibited intensive adhesive wear, thus yielding a longer tool life than TiAlCrN monolayer coated tools [130].

The wear performance of TiAlCrSiYN/TiAlCrN nano-multilayer coated tools with different chemical compositions of TiAlCrSiYN during the machining of direct aged Inconel (DA) 718 and powder metallurgical ME 16 Ni-based super-alloys was investigated by Fox-Rabinovich et al. [131]. Due to the low thermal conductivity of these alloys, the heat generated at the cutting zone could reach 900–1000 °C, resulting in severe tool wear, even at moderate cutting speeds. The multilayer coating with TiAlCrSiYN containing a higher concentration of 60 at.% Al exhibited higher oxidation, cracking resistance and ability to dissipate energy during friction, and a lower COF at elevated temperatures. This coating exhibited a lower wear rate in the machining of Inconel alloy. However, the multilayer coating with TiAlCrSiYN containing 55 at.% Al possessed the combined properties of superior oxidation resistance, hardness, and resistance to plastic deformation. This coating exhibited better performance in machining powder metallurgy ME 16 Ni-based superalloys. A main feature of this nano-multilayer coating was its enhanced ability to form protective ceramic tribo-films (i.e. sapphire and mullite), and lubricious silicon and chromium oxides at elevated temperatures [132,133]. For this particular coating system, the cutting parameters could be optimised in order to control the tribo-film formation to achieve longer tool life. By using an initial high cutting speed, followed by a slower speed, it was possible to prolong the tool life of the TiAlCrSiYN/TiAlCrN multilayer coated tool in the machining of the (DA) 718 alloy. With a higher initial cutting speed, the tool showed intensive formation of thermal protective ceramic and lubricious tribo-films, resulting in better frictional conditions at the chip/tool interface. Upon a subsequent reduction in speed, the ceramics tribo-films generated at the initial stage of machining were protected from total wear, which resulted in an overall increase in tool life [134]. The initial tribo-film formed on the TiCrAlSiYN/TiCrAlN multilayer coating was predominantly mullite. It was a protective and thermal barrier tribo-film responsible for reduced surface damage and the stabilization of wear rate after the running-in process. These features were another advantage of this multilayer coating architecture [135].

Chowdhury et al. [133] reported that the TiCrAlN/TiCrAlSiYN bi-multilayer coatings (with TiAlCrN interlayer between the TiCrAlN/TiCrAlSiYN multilayers and substrate) possessed higher hardness, H/E and H^3/E^2 values as well as providing better surface protection than the TiAlCrSiYN and TiAlCrN monolayer coatings and the TiCrAlN/TiCrAlSiYN multilayer coatings (without TiAlCrN sublayer). This could be attributed to the effectiveness of the multilayer structure and TiCrAlN in inhibiting crack propagation. The TiAlCrN interlayer was slightly softer, and therefore its presence improved the adhesion strength of the bi-multilayer coatings. The bi-multilayer coating with a thickness of 3 μm provided better surface protection than the thinner bi-multilayer coating with a thickness of 2 μm. This was due to the better load support provided by the thicker coating, which absorbed most of the impact energy and thereby prevented substrate deformation. The low intensity of surface damage on the bi-multilayer coatings promoted rejuvenation of the protective tribo-films after being worn out. The reasons for the longest tool life and lowest cutting forces produced in milling hardened AISI

Table 4 – Summary of the deposition method and parameters, substrate, description of coating, elemental composition, and hardness, Young's modulus, H/E and H^3/E^2 of TiAlCrN multilayer coatings.

Ref.	Deposition method	Substrate	Description of coating	Cr content (at.%)	Nb content (at.%)	Hardness (GPa)	Young's Modulus (GPa)	H/E	H^3/E^2 (GPa)
Nakonechna et al. [126]	Cathodic arc method	WC-Co (Rutherford backscattering spectroscopy (RBS), SEM and TEM characterization, nano-indentation)	TiAlN/TiAlCrN multilayer with nominal composition of:						
			$Ti_{18}Al_{22}Cr_{26}N_{35}$ (bilayer thickness of 400 nm)			32.9	350	0.0940	0.2907
			$Ti_{19}Al_{16}Cr_{16}N_{49}$ (bilayer thickness of 10 nm)			38.4	323	0.1189	0.5427
Fox-Rabinovich et al. [128]	Unbalanced magnetron sputtering	Mirror polished WC-Co cutting insert (SEM, EDX XRD and XPS characterization, micro-indentation), ball nose end mills (machining), gamma-TiAl intermetallic samples (oxidation test)	TiAlCrN monolayer		–	34.40	577	0.0596	0.1223
			TiAlCrN/NbN multilayer		1.75	31.60	560	0.0564	0.1000
			TiAlCrN/NbN multilayer		3.81	31.67	539	0.0587	0.1093
			TiAlCrN/NbN multilayer		9.28	31.61	501	0.0631	0.1258
Fox-Rabinovich et al. [131]	Plasma-enhanced arc source	WC-Co (STEM, EDX, TEM and FIB characterization, nano-indentation, scratch and oxidation tests), K 313 cemented carbide inserts (machining)	$Ti_{0.2}Al_{0.55}Cr_{0.2}Si_{0.03}Y_{0.02}N$ monolayer			28.4 ± 3.5	343.8 ± 27	0.0826	0.1938
			$Ti_{0.2}Al_{0.55}Cr_{0.2}Si_{0.03}Y_{0.02}N/Ti_{0.25}Al_{0.65}Cr_{0.1}N$ multilayer			28.4 ± 4.8	327.1 ± 36	0.0868	0.2141
			$Ti_{0.15}Al_{0.6}Cr_{0.2}Si_{0.03}Y_{0.02}N$ monolayer			25.9 ± 2.4	314.6 ± 20	0.0823	0.1755
			$Ti_{0.15}Al_{0.6}Cr_{0.2}Si_{0.03}Y_{0.02}N/Ti_{0.25}Al_{0.65}Cr_{0.1}N$ multilayer			24.5 ± 3.9	298.2 ± 26	0.0822	0.1654
Chowdhury et al. [133]	R&D-type hybrid PVD coater	Mirror polished WC-Co (SEM, EDX, XRD, TEM and FIB characterization, ball nose end mills (machining)	$Ti_{0.2}Al_{0.55}Cr_{0.2}Si_{0.03}Y_{0.02}N$ monolayer			29.6	489.8	0.0604	0.1081
			$Ti_{0.25}Al_{0.65}Cr_{0.1}N$ monolayer			25.9	430.7	0.0601	0.0937
			$Ti_{0.2}Al_{0.55}Cr_{0.2}Si_{0.03}Y_{0.02}N/Ti_{0.25}Al_{0.65}Cr_{0.1}N$ multilayer			28.4	429.0	0.0662	0.1245
			$Ti_{0.2}Al_{0.55}Cr_{0.2}Si_{0.03}Y_{0.02}N/Ti_{0.25}Al_{0.65}Cr_{0.1}N$ bi-multilayer with TiAlCrN interlayer (total thickness of 2 μm)			31.6	432.7	0.0730	0.1685
			$Ti_{0.2}Al_{0.55}Cr_{0.2}Si_{0.03}Y_{0.02}N/Ti_{0.25}Al_{0.65}Cr_{0.1}N$ bi-multilayer with TiAlCrN interlayer (total thickness of 3 μm)			30.9	474.6	0.0651	0.1310
Fernandes et al. [136]	DC reactive magnetron sputtering	Polished WC-Co (SEM and EDX characterization, nano-indentation, scratch test), FeCrAl alloy (XRD characterization, oxidation test), WC-Co drills (machining)	TiAlCrN multilayer with alternate TiAlN/CrAlN and nominal composition of:						
			$Ti_{0.30}Al_{0.46}Cr_{0.26}N$	12.8		17.0	459	0.0370	0.0233
			$Ti_{0.28}Al_{0.34}Cr_{0.42}N$	20.7		16.8	444	0.0378	0.0241
			$Ti_{0.28}Al_{0.31}Cr_{0.51}N$	24.3		19.8	469	0.0422	0.0353
Danek et al. [137]	DC reactive magnetron sputtering	Polished WC-Co (SEM and EDX characterization, nano-indentation, scratch test), FeCrAl alloy (XRD characterization, oxidation test), WC-Co drills (machining)	TiAlCrN multilayer with alternate TiAlN/CrAlN and nominal composition of:						
			$Ti_{0.30}Al_{0.46}Cr_{0.26}N$	12.8		17.0	459	0.0370	0.0233
			$Ti_{0.28}Al_{0.34}Cr_{0.42}N$	20.7		16.8	444	0.0378	0.0241
			$Ti_{0.28}Al_{0.31}Cr_{0.51}N$	24.3		19.8	469	0.0422	0.0353

Hsu et al. [138]	Cathodic arc evaporation	AISI 304 stainless steel (FESEM, EPMA and XRD characterization, nano-indentation, scratch and ball-on-disc tests)	TiAlCrN multilayer with alternate CrN/TiAlN deposited using substrate bias voltage (V) of:	20.4	20	288	0.0694	0.0965
			−90	21.1	24	298	0.0805	0.1557
			−120	25.5	38	319	0.1191	0.5392
			−150	23.1	29	301	0.0963	0.2692
			−180					

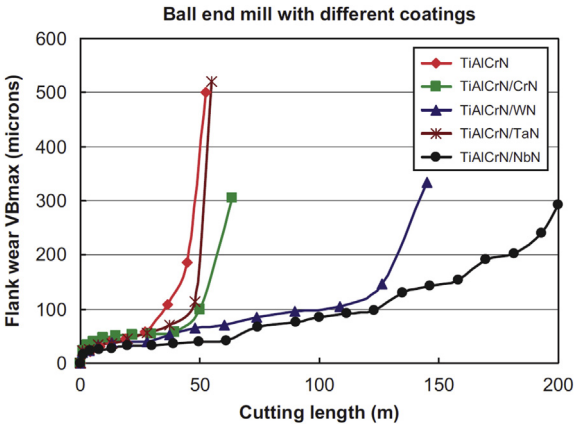

Fig. 11 – Tool wear curves of ball end mills coated with TiAlCrN-based coatings (cutting parameters: $V_{c\ max}$: 300 m/min, f_t: 0.06 mm, a_p: 5 mm, a_c: 0.6 mm). Reprinted from International Journal of Machine Tools and Manufacture, 48(6), L. Ning, S.C. Veldhuis, K. Yamamoto, Investigation of wear behavior and chip formation for cutting tools with nano-multilayered TiAlCrN/NbN PVD coating, 656–665, Copyright (2008), with permission from Elsevier [129].

H13 tool steel under dry conditions could be directly related to the enhanced mechanical and tribological properties explained above.

Fernandes et al. [136] and Danek et al. [137] found that the Young's modulus, hardness, H/E and H^3/E^2 of the multilayer TiAlCrN coatings consisting of alternate Ti(Al)N/Cr(Al)N increased with greater Cr content. Cr also enhanced the oxidation resistance of the multilayer coatings by forming an inner Al–Cr–O amorphous or crystalline $Cr(Al)_2O_3$ layer (depending on the Cr content), which effectively suppressed the diffusion of Ti to the surface and the inward diffusion of O. Hsu et al. [138] studied the effect of bias voltage (specifically, −90, −120, −150 and −180 V) on the mechanical properties of CrTiAlN multilayer coatings consisting of alternate layers of CrN and TiAlN. The optimal substrate bias voltage was found to be −150 V since it resulted in the highest Cr content in the coating and produced the highest adhesion strength, hardness, elastic modulus, H/E, and also the lowest COF (Fig. 10).

4. Review of TiAlVN coatings

4.1. *Mechanical, thermal stability, oxidation and tribological behaviour of TiAlVN monolayer coatings*

V content has been found to significantly influence the microstructural, mechanical, and tribological properties of TiAlVN coatings. By varying the chemical composition, Kutschej et al. [139] and Pfeiler et al. [140] obtained maximum hardness, H/E and H^3/E^2 values of 27.5–46.0 GPa, 0.0840 and 0.1698 GPa, respectively (Table 5). The mean of the maximum hardness value was 36.8 GPa. Kutschej et al. [139] attributed the increase in the hardness of TiAlVN coatings with increasing V content to the effect of solid solution hardening. V also gave rise to other effects such as retarding the transformation of face centre

Table 5 – Summary of the deposition method and parameters, substrate, elemental composition, and hardness, Young's modulus, H/E and H^3/E^2 of TiAlVN monolayer coatings.

Ref.	Deposition method	Substrate	Bias voltage (V)	V content in the coating (at.%)	V content in the target (at.%)	Al/Ti in the coating	Hardness (GPa)	Young's Modulus (GPa)	H/E	H^3/E^2 (GPa)	Remark
Kutschej et al. [139]	Unbalanced DC magnetron sputtering	AISI M2 high speed steel (EDX, XRD and Raman characterization, micro-indentation, ball-on-disc test)	Not available	6	5	1.30 (Target: 1.0 Al/Ti)	43				
				5.6	5	1.95 (Target: 1.5 Al/Ti)	46				
				2.4	2	2.70 (Target: 2.0 Al/Ti)	27				
				5.6	5	2.75 (Target: 2.0 Al/Ti)	28				
				11.1	10	2.30 (Target: 2.0 Al/Ti)	32				
				–	25	- (Target: 2.0 Al/Ti)	38				
Pfeiler et al. [140]	Cathodic arc evaporation	Cemented carbide cutting inserts (GDOES and GAXRD characterization, nano-indentation), cemented carbide discs (ball-on-disc test), single-crystal Si (100) (residual stress measurement)	Constant at −40	0			21.0[a]	250[a]	0.0840	0.1482	[a]estimated from Fig. 2 in ref. [140]
				16.5			27.5[a]	350[a]	0.0786	0.1698	
				20			25.0[a]	325[a]	0.0769	0.1479	
				25			25.5[a]	340[a]	0.0750	0.1434	
Tillmann et al. [145]	Magnetron sputtering	High-speed steel HS6-5-2C (SEM, EDX and XRD characterization, nano-indentation, residual stress measurement, ball-on-disc test)	−50				29.18	445.1	0.0656	0.1254	
			−100				43	532.8	0.0807	0.2801	
			−150				43.28	560.9	0.0772	0.2577	
Pfeiler et al. [146]	Cathodic arc evaporation	Cemented carbide cutting inserts (GDOES and GAXRD characterization, nano-indentation), TSM33 cement carbide disc (ball-on-disc test), single-crystal Si (100) (residual stress measurement)	−40				27.7[b]	349[b]	0.0791	0.1726	[b]estimated from Fig. 2 in ref. [146]
			−80				34.2[b]	480[b]	0.0708	0.1706	
			−120				38.5[b]	532[b]	0.0714	0.1939	
			−160				38.1[b]	485[b]	0.0784	0.2333	

cubic (fcc) structure to hexagonal close-packed (hcp), and reducing the residual compressive stress in the coating, depending on the V content [140]. The increased hardness for the coating with 16.5 at.% V was due to the suppression of the transformation of fcc to hcp structure. However, further increasing V content to 20 and 25 at.% resulted in a reduction in the residual compressive stress and thus the hardness. The wear of TiAlVN coatings was found to decrease with greater V content: all TiAlVN coatings exhibited lower wear than the TiAlN coating in sliding tests carried out at room temperature. Coatings with higher V content had lower Ti content, leading to less abrasive TiO_2 wear debris produced at the interface during sliding. The relatively low wear of the TiAlVN coatings with higher V content could therefore be attributed to their enhanced hardness and to the reduced levels of abrasive wear debris produced. However, at 500 °C, the TiAlVN coatings exhibited more wear than the TiAlN coating, which only worsened with greater V content. The observed deterioration in wear resistance with increasing V content at elevated temperatures was due to a reduction in the oxidation resistance by the formation of non-protective V-oxides. This result was in accordance with the findings of Kutschej et al. [141], which showed that TiAlVN had lower oxidation resistance and was completely oxidised at 750 °C. In contrast, the rapid oxidation of TiAlN took place at above 800 °C [142]. Xu et al. [143] investigated the thermal stability and oxidation resistance of TiAlVN coatings. In the annealing of TiAlVN, V retarded the formation of w-AlN, leading to a pronounced hardening effect. However, the addition of V also promoted the transformation of a-TiO_2 to r-TiO_2 and to less dense Al_2O_3, leading to degradation of the oxidation resistance.

Kutschej et al. [139] found that although Al decreased the grain size of TiAlVN coatings it also promoted the decomposition of fcc to hcp structure, which had an adverse effect on the hardness. Coatings deposited using targets with Al/Ti ratios of 1 and 1.5 at a fixed 5 at.% V had an fcc structure. Deposition using targets with V content of 2, 5, 10, and 25 at.% at a higher fixed Al/Ti ratio of 2 produced coatings with smaller grains and fcc and hcp dual-phase structure. The hcp AlN resulted in a reduction in the hardness of the coatings (Table 5). Al also had a great influence on the decomposition of fcc structure to hcp AlN phase at elevated temperatures. This effect explained the significant hardness reduction found for the coatings with high Al content when temperature was increased from 600 to 700 °C.

The Ar:N_2 gas ratio used in coating deposition had a pronounced effect on microstructure and mechanical properties [144]. All TiAlVN coatings produced under various Ar:N_2 gas ratios had a single-phase fcc structure. However, increasing the Ar:N_2 gas ratio led to greater atomic mobility and thus the formation of densified and fine-grained structures which gave rise to high hardness and elastic modulus but a low COF. Tillmann et al. [145] and Pfeiler et al. [146] proposed that the increase in the hardness and elastic modulus of the TiAlVN coatings with increasing bias voltage (Fig. 12) was caused by the microstructural change from dual-phase fcc + hcp structure to a single-phase fcc structure, as well as an increase in the internal compressive stress. Decreasing the bias voltage reduced the wear coefficient, which the authors attributed to reduced contact area due to the high droplet density formed

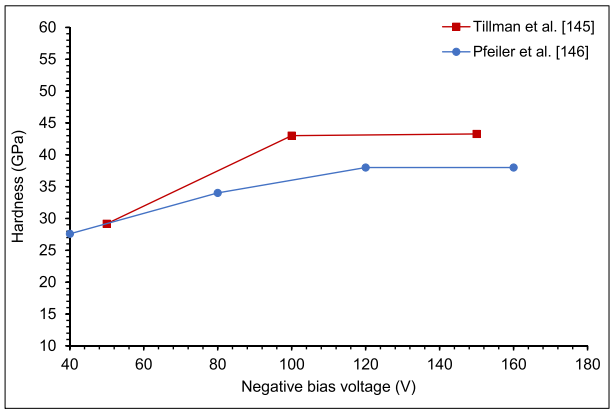

Fig. 12 – Variation in the hardness of the TiAlVN coatings with negative bias voltages.

on the coating surface. High droplet density also produced greater wear on the counter body and hence more wear debris, which subsequently protected the coating from further wear. Other researchers [145] found that high hardness and compressive stress produced by high bias voltage caused coating spallation and the formation of micro-cracks. Penetration of the crack tip into the counter body resulted in increased friction. In another study, Tillmann et al. [38] found that higher heating power used in coating deposition increased the hardness and abrasive wear resistance of TiAlVN coatings. Sliding at 500 °C produced V_2O_5 at the contact surfaces, yielding a lower COF than at room temperature. The maximum levels of hardness, H/E and H^3/E^2 obtained by varying the bias voltage ranged between 38.5–43.3 GPa, 0.0791–0.0807 and 0.2333–0.2801 GPa, respectively, with means of 40.9 GPa, 0.0799 and 0.2567 GPa [145,146].

The formation of V_2O_5 at high temperatures in TiAlVN coatings had great potential for friction reduction due to its low shear strength [147]. Above its melting point of between 670–685 °C, V_2O_5 acted as a liquid lubricant with a low COF [148,149]. Kutschej et al. [141] found a correlation between the COF and the types of oxides formed on the TiAlVN coatings. At 600 °C, the coatings started to oxidise rapidly to form V_2O_5. The COF further reduced to about 0.6 at 650 °C due to massive oxidation which formed a greater amount of V_2O_5 (Fig. 13). The lowest COF was obtained in the initial stage of sliding at 750 °C where the oxides formed on the worn surface were primarily V_2O_5. Analysis of the worn surface revealed that the formation of V_2O_5 was responsible for the low COF (0.2–0.4) compared to that of TiAlN coatings (typical values of between 0.6 and 1.6) [2,14,150,151]. Prolonged sliding led to the formation of substantial TiO_2 and Al_2O_3, followed by $AlVO_4$ from the reaction between Al_2O_3 and V_2O_5, which increased the COF. Reduction in the amount of Al_2O_3 to form $AlVO_4$ could also have led to deterioration of the coating's oxidation resistance [142]. Kathrein et al. [152] credited the formation of V_2O_5 for the outstanding performance of the TiAlVN coated tool, which had the longest tool life (defined as the time for the flank wear to reach 0.3 mm), followed by the TiAlN, TiAlTaN, and TiAlBN coated tools.

Kutschej et al. [139] studied the effects of V content on the tribological behaviour of TiAlVN coatings with a fixed Al/Ti

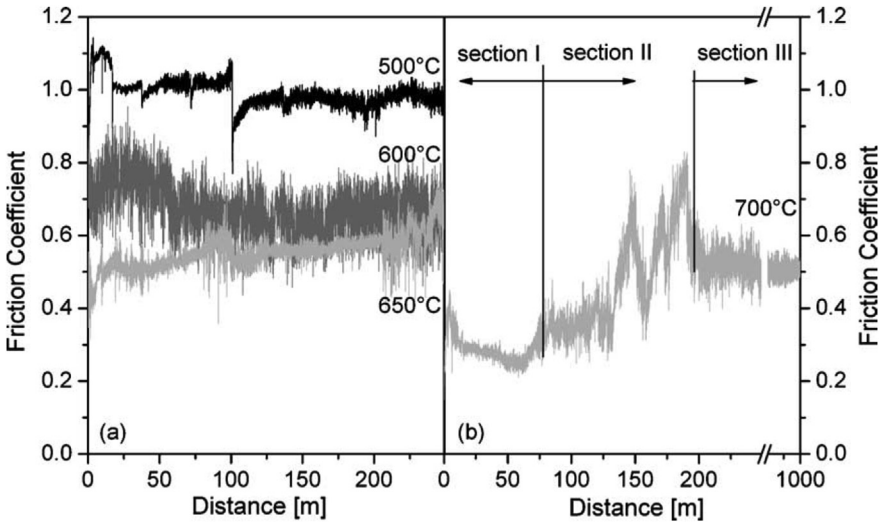

Fig. 13 – Friction curves of TiAlVN coatings tested against alumina balls at (a) 550, 600, 650 °C, and (b) 700 °C. Reprinted from Surface and Coatings Technology, 200(5–6), K. Kutschej, P.H. Mayrhofer, M. Kathrein, P. Polcik, C. Mitterer, Influence of oxide phase formation on the tribological behaviour of Ti–Al–V–N coatings, 1731–1737, Copyright (2005), with permission from Elsevier [141].

ratio. The COF was found to decrease with greater V content at 700 °C, which could be attributed to the increased amount of lubricious V_2O_5 formed at the interface. However, with prolonged sliding and at higher flash temperatures, V_2O_5 could change to VO_2, with an accompanying increase in the COF. Cai et al. [153] used thermal treatment to induce VO_2 and V_2O_5 layers on two VN samples. Although V_2O_5 exhibited higher values of H/E and H^3/E^2 and a lower COF due to its high lubricity, it had the disadvantage of possessing poorer wear resistance due to its low melting temperature. In contrast, VO_2, having a higher melting temperature of 650 °C, demonstrated higher resistance to wear.

4.2. *Mechanical, thermal stability, oxidation and tribological behaviour of TiAlVN multilayer coatings*

To date, the TiAVN multilayer coatings investigated have consisted of alternate layers of TiAlN/VN and had a maximum hardness of 28.3–38.4 GPa (Table 6) with a mean of 34.1 ± 3.8 GPa. Lewis et al. [142] investigated the effect of temperature on the oxidation behaviour of TiAlN/VN multilayer coatings. The onset temperature for rapid oxidation was between 632–645 °C, depending on the (Ti + Al)/V ratio, which decreased with greater power to the V target (Table 6). This onset temperature rose with higher (Ti + Al)/V ratios, indicating that the oxidation resistance increased with a reduction in V content. $AlVO_4$, TiO_2 and V_2O_5 were formed at 550 °C. The oxides that appeared on the surface at 550–670 °C were V_2O_5, r-TiO_2 and $AlVO_4$ which evolved from a reaction between V_2O_5 and Al_2O_3. Their relatively low oxidation resistance, as compared to monolithic TiAlN coatings which exhibited rapid oxidation at above 800 °C, was caused by the depletion of protective Al_2O_3, which was utilized to produce $AlVO_4$. Another study [154] showed that surface oxidation, resulting in the formation of a small amount of V_2O_5, occurred at 550 °C. Oxidation at above 600 °C produced an outer layer of r-TiO_2 and $AlVO_4$, and an inner nano-crystalline microstructure likely to consist of V_2O_5, Al_2TiO_5 and VO_2 phases. TEM analysis showed evidence of preferential oxidation along the columnar grain boundaries between the oxide and coating, which provided paths for the diffusion of atoms. At 672 °C, the entire coating was oxidized and suffered extensive spallation. An in-depth study on the oxidation behaviour of TiAlN/VN at elevated temperatures carried out by Zhou et al. [155] showed that the oxidation resistance of TiAlN/VN was governed by the VN layers. The oxidation onset temperature of the TiAlN/VN coating was 550 °C, with VN being the first component to be oxidized to form V_2O_5. The onset temperature for rapid oxidation was 635 °C. Oxidation at above 600–638 °C produced a duplex structure oxide with an outer region of V_2O_5, TiO_2, and $AlVO_4$, and an inner porous region comprising Ti-rich and V-rich nanocrystallites (most likely TiO_2, V_2O_5, Al_2TiO_5 and VO_2). At 638 °C, a layer of V_2O_5 was formed on top of the duplex layer. At 672 °C, spallation occurred, and the coating was completely oxidized with reduced V_2O_5 and an increased amount of TiO_2 and $AlVO_4$.

Zhou et al. [156] studied the friction behaviour of multilayer TiAlN/VN at various temperatures. The average steady-state COF in the dry sliding of TiAlN/VN against Al_2O_3 at the three temperatures 25, 300, and 635 °C were 0.53, 1.03 and 0.46, respectively. However, the wear rate of the coating increased at higher temperatures. At 25 °C, the suppression of wear by the hydrated tribo-layer (i.e. amorphous monohydroxide) resulted in a low COF and mild adhesive wear. At 300 °C, cracking of the coating was evident and an increase in friction due to the transformation of the monohydroxide to an amorphous (TiAlV)O_xN_y occurred. Sliding at 635 °C produced mainly V_2O_5, leading to lower friction. The presence of a low wear resistance porous oxide scale (formed by extensive volume expansion during the transformation of nitrides to

Table 6 – Summary of the deposition method and parameters, substrate, description of coating, and hardness of TiAlN/VN multilayer coatings.

Ref.	Deposition method	Substrate	Description of coating	Hardness (GPa)	Remark
Lewis et al. [142]	Reactive unbalanced magnetron sputtering	Stainless steel and M2 HSS (SEM, EDX and XRD characterization, Knoop indentation, oxidation and ball-on-disc tests)	(Ti + Al)/V = 1.73 (deposited at 5.5 kW of V target) (Ti + Al)/V = 1.29 (deposited at 7.0 kW of V target) (Ti + Al)/V = 1.59 (deposited at 7.0 kW of V target) (Ti + Al)/V = 1.14 (deposited at 8.0 kW of V target)	32.57[a] 32.58[a] 33.28[a] 36.19[a]	[a]Converted from Knoop hardness (HK) reported by the authors.
Hovsepian et al. [160]	Cathodic arc/ unbalanced magnetron sputtering	High-speed steel (SEM and TEM characterisation, Knoop indentation, pin-on-disc test)	TiAlN/VN	33.5	
Luo et al. [162]	Cathodic arc/ unbalanced magnetron sputtering	Low alloy steel P20 (SEM, XRD and TEM characterisation, Knoop indentation, scratch and pin-on-disc tests), high-speed steel M2 drills (machining)	TiAlN/VN deposited on: Nitrided P20 Non-nitrided P20 Non-nitrided M2 TiAlCrYN deposited on: Nitrided P20 Non-nitrided P20 Nitride M2 Non-nitrided M2	 28.3 ± 1.4 22.2 ± 1.0 25.7 ± 1.8 27.2 ± 3.5 26.6 ± 2.5 28.0 ± 2.1 23.0 ± 1.6	
Kong et al. [163]	Reactive magnetron sputtering	High-speed steel (EDX, XRD and TEM characterisation, nano-indentation)	(Ti,Al)N/VN with modulation period Λ (nm) of: 1.6 3.4 5.6 8.8 11.9	 32.9[b] 33.5[b] 38.4[b] 30.8[b] 30.0[b]	[b]estimated from Fig. 5 in ref. [163]

oxides) was proposed as the reason for the high specific wear rate at this temperature. Dry sliding of alumina balls on TiAlN/VN at room temperature and at 500 °C produced COFs of 0.55 and 0.95, respectively [157]. The increase in COF with temperature could be associated with the change in wear mechanism from mild abrasion to adhesion. Sliding at 700 °C produced the low COF of 0.18 due to the melting of V_2O_5 (estimated melting temperature 635 °C). This low COF prevailed until the liquid V_2O_5 transformed to lower-oxidized vanadium such as V_3O_7, V_4O_9, and V_6O_{13}, and subsequently VO_2, which was responsible for an increase in the COF to about 0.55. In another wear test involving a corundum polycrystalline ball sliding on the TiAlV/VN showed that the wear debris rich in V_2O_5 was responsible for the relatively low COF of 0.54 [158].

Luo [159] studied the tribological behaviour of TiAlN/VN sliding against alumina balls at a broad range of temperatures. Fig. 14 shows the changes in COF with temperature. Below 100 °C, the TiAlN/VN coating exhibited the low COF of 0.6, and the wear rate was governed by mild oxidation wear related to hydroxide tribo-layer formation via the absorption of water vapour. Transition to a higher COF at 100–200 °C was caused by a lack of tribo-layer formation due to dehydration at the contact surfaces. At 200–400 °C, the COF further increased to 0.86–0.89, and severe wear occurred, dominated by cracking and spallation due to intensified stress. Above 500 °C, accelerated oxidation was the dominant mode of wear. Massive oxide debris and a high COF of 1.1 were produced at 500 °C. Approaching the melting temperature of V_2O_5, the shearing resistance of V_2O_5 became the factor controlling COF. In other words, the significant drop in COF with increasing temperature above 550 °C was due to a reduction in the shearing resistance of V_2O_5. At 700 °C, melted V_2O_5 resulted in a dramatic reduction in COF to 0.24. In the high-speed dry milling of wrought Al7010-T7651 and cast AlSi9Cu1 aluminium alloys, it was concluded that V_2O_5 had played a major role in the outstanding performance of the TiAlN/VN coated tools [160]. These tools exhibited longer tool life than the TiAlCrYN and DLC coated and uncoated high-speed steel tools. The TiAlN/VN coated tools also produced lower cutting forces and better surface finish and had a lower propensity for work material adhesion, with no evidence of built-up edge and material transfer on the tool surface. Luo and Hovsepian [161] suggested an alternative view in which it was proposed that the low COF of 0.4 and wear rate of their TiAlN/VN were due to the multi-component V–Al–Ti–O oxides in the tribo-film and wear debris. The tribo-film was formed by the self-sintering process of oxide wear debris at the sliding surfaces.

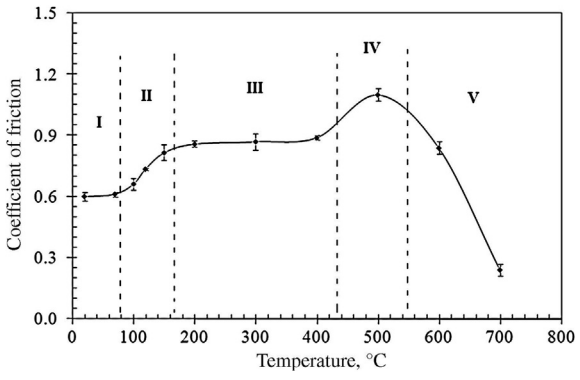

Fig. 14 – Variation of the average steady-stage COF with temperature. Reprinted from Wear, 271(9–10), Q. Luo, Temperature dependent friction and wear of magnetron sputtered coating TiAlN/VN, 2058–2066, Copyright (2011), with permission from Elsevier [159].

Improvements in the mechanical properties and wear resistance of TiAlN/VN multilayer coatings have been attained by treating the substrate surface with pulse plasma nitriding prior to coating deposition [162]. The hardened layer formed on the surface of the substrate in this pre-treatment enhanced the hardness and load-bearing ability of the TiAlN/VN coating, leading subsequently to improved adhesion of the coating with little evidence of cracking upon failure. The untreated M2 drills coated with TiAlN/VN had longer life than the TiAlN and TiCN monolayer coated tools in drilling austenite stainless steel AISI304 under emulsion lubrication. Pre-nitriding the M2 substrate extended the tool life significantly. Kong et al. [163] found that the hardness of (Ti,Al)N/VN multilayer coatings decreased when pronounced composition intermixing of the layers and incoherent interfaces emerged at $\Lambda < 3.4$ nm and $\Lambda > 8.8$ nm, respectively. The coating deposited at Λ between 3.4 and 8.8 nm had higher hardness due to the inhibition of dislocation motion by the alternating tensile and compressive strain developed by the lattice mismatch of the (Ti,Al)N and VN layers.

5. Review of TiAlTaN coatings

5.1. *Mechanical, thermal stability, oxidation and tribological behaviour of TiAlTaN monolayer coatings*

Seidl et al. [164] reported an increase in the hardness of TiAlTaN coatings with greater Ta content. This could be attributed to increased compressive stress, solid solution hardening due to the substitution of Ti and Al by Ta atoms in the fcc lattice, and cohesive strength due to the higher valence electron concentration (VEC) of the alloy. The maximum hardness, H/E and H^3/E^2 of the TiAlTaN monolayer coatings obtained using various deposition methods and chemical compositions were 26.2–35.5 GPa, 0.0826–0.0934 and 0.1784–0.3098 GPa, respectively (Fig. 15 and Table 7), with means of 32.3 ± 3.4 GPa, 0.0871 ± 0.0046 and 0.2478 ± 0.0539 GPa. Among all previous studies [165–169] only the work by Sui et al. [167] showed that Ta led to a significant increase in hardness. The results produced by Mikula et al. [166] showed that an initial increase in Ta content increased the coating hardness but reduced the modulus of elasticity. This brought about a marked increase in the H/E and H^3/E^2 values, indicating a significant enhancement in its toughness. The *ab initio* density functional theory (DFT) analyses showed that the substitution of Ta in TiAlN improved the toughness as it promoted the occupation of metal–metal bonds while preserving the strong metal-N bonds. Seidl et al. [165] found that while increasing the Ta content increased the hardness, H/E and H^3/E^2, the fracture toughness (K_{IC}) could decrease due to the formation of hexagonal-based phases such as Ta_5N_6. Ta

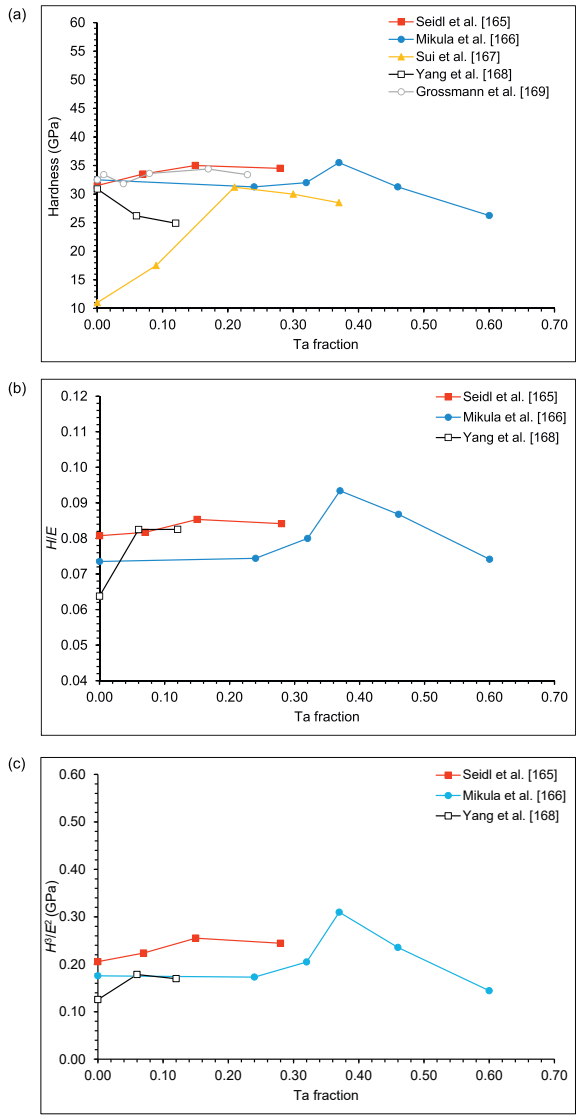

Fig. 15 – Comparison of the (a) hardness, (b) *H/E* and (c) H^3/E^2 ratio measured for TiAlTaN coatings deposited by various deposition techniques as a function of Ta fraction (Nominal composition).

could also increase the proportion of hexagonal w-AlN phases, leading to reduced hardness of TiAlTaN [168] (Fig. 15 and Table 7).

Seidl et al. [164] found that the peak hardness achievable by annealing increased with greater Ta content (Fig. 16). Annealing the as-deposited $Ti_{0.38}Al_{0.34}Ta_{0.28}N$ increased its hardness from 34 to a peak value of 39.5 GPa. The peak hardness and the increase in the hardness magnitude were greater than those with smaller amounts of Ta (i.e. $Ti_{0.44}Al_{0.41}Ta_{0.15}N$ and $Ti_{0.49}Al_{0.44}Ta_{0.07}N$), which were found to increase from 35 to 36 GPa and 33.5–34.5 GPa, respectively. This increase in the hardness by annealing was due to spinodal decomposition of the saturated solid solution into cubic AlN, TiN, and TaN rich domains. Comparison of Fig. 16(a) and (b) reveals similar variation behaviour of both the *H/E* and H^3/E^2 ratios, and the hardness of the annealed TiAlTaN coatings. Ta also delayed the formation of w-AlN from the fcc AlN rich domain at a higher temperature. Therefore, a rapid decrease in hardness occurred at higher temperatures. Similarly, Rachbauer et al. [39] and Grossmann et al. [170] concluded that Ta retarded the decomposition of the supersaturated solid solution to stable constituents of c-$Ti_{1-z}Ta_zN$ and w-AlN at a higher temperature. The onset temperatures for the formation of w-AlN phase for $Ti_{0.41}Al_{0.59}N$, $Ti_{0.41}Al_{0.56}Ta_{0.03}N$, $Ti_{0.40}Al_{0.55}Ta_{0.05}N$, and $Ti_{0.42}Al_{0.48}Ta_{0.10}N$ were 900, 900, 1100 and 1200 °C, respectively. In other words, Ta increased the onset temperature by approximately 200–300 °C [39]. This increase in the hardness of TiAlTaN upon annealing was due to the formation of cubic phases of c-Ti-Ta-rich and c-Al-rich domains via spinodal decomposition. Koller et al. [171] reported that the hardness of $Ti_{0.54}Al_{0.46}N$ was retained at annealing temperatures up to 600 °C but above this temperature, hardness reduced gradually (Fig. 17). The marked reduction in the hardness at 1000–1200 °C was due to the decomposition of the supersaturated TiAlN phase to c-TiN and w-AlN. Similar to that of $Ti_{0.54}Al_{0.46}N$, the hardness of the as-deposited $Ti_{0.45}Al_{0.36}Ta_{0.19}N$, was retained up to 800 °C. Above this temperature, the hardness of $Ti_{0.45}Al_{0.36}Ta_{0.19}N$ increased due to the formation of Ti-rich and Al-rich domains and the retardation of c-TiN and w-AlN formation.

Increases in adatom mobility and compressive stress with higher bias voltages may hinder the growth of the less dense hcp phase and favour the growth of the fcc phase [167,172]. Sui et al. [167] found that the increase in the hardness of TiAlTaN coatings with increasing Ta content was primarily due to the increase in the solid solution strengthening effect resulting from an increase in the lattice constant. When Ta content exceeded the solubility limit, no further increase in the hardness was observed (Table 7). Reduced grain size, significant lattice distortion (due to the substitution of Ta atoms into the fcc TiAlN), and high local strain brought about by the presence of Ta could result in increased boundary and alloy scattering leading to a reduction in thermal conductivity. Both the time-domain thermoreflectance (TDTR) experiment and kinetic model showed that thermal conductivity decreased consistently with greater Ta content [173]. Coatings with low conductivity are preferable for high-speed machining applications as they can effectively deflect the intense heat generated into the chip, which will otherwise conduct into the tool and cause severe tool wear.

Researchers have reported different mechanisms by which Ta increased the oxidation resistance of TiAlTaN. Rachbauer et al. [39] found that $Ti_{0.41}Al_{0.59}N$ was fully oxidized to form a porous oxide after being heated at 850 and 950 °C for 20 h in air. However, the $Ti_{0.40}Al_{0.55}Ta_{0.05}N$ and $Ti_{0.42}Al_{0.48}Ta_{0.10}N$ formed thinner oxide layers consisting of Al-enriched oxide on the surface, and a dense Ti- and Ta-enriched layer, and a porous Ti- and Ta-enriched oxide at the subsurface. Pfeiler et al. [174] also observed the same layered structure in the TiAlTaN coating after being exposed at 900 °C for 5 h. In contrast, TiAlN was completely oxidized to form the much thicker Al_2O_3 and TiO_2. By adding Ta into TiAlN, the oxidation resistance was improved because $Ti_{1-x}Ta_xO_2$ (formed by the replacement of Ti^{3+} ions in TiO_2 by the Ta^{5+} ions) resulted in reduced oxygen vacancy and thus the retardation of oxygen

Table 7 – Summary of the deposition method and parameters, substrate, nominal and elemental composition, and hardness, Young's modulus, H/E and H^3/E^2 of TiAlTaN monolayer coatings.

Ref.	Deposition method	Substrate	Bias voltage (V)	Nominal composition	Ta content (at.%)	Hardness (GPa)	Young's Modulus (GPa)	H/E	H^3/E^2 (GPa)	Remark
Seidl et al. [165]	Cathodic arc evaporation system	Si (100) (SEM, EDX and XRD characterization, fracture toughness, nano-indentation)	Constant at −40	$Ti_{0.54}Al_{0.46}N$	0	31.5[a]	390[a]	0.0808	0.2055	[a]estimated from Fig. 4(b) in ref. [165]
				$Ti_{0.49}Al_{0.44}Ta_{0.07}N$	7	33.5[a]	410[a]	0.0817	0.2236	
				$Ti_{0.44}Al_{0.41}Ta_{0.15}N$	15	35.0[a]	410[a]	0.0854	0.2551	
				$Ti_{0.38}Al_{0.34}Ta_{0.28}N$	28	34.5[a]	410[a]	0.0841	0.2443	
Mikula et al. [166]	Unbalanced magnetron co-sputtering	Mirror polished Si (001) (EDX and XRD characterization), WC-Co (nano-indentation)	Not available	$Ti_{0.46}Al_{0.54}N$	0	32.5[b]	442[b]	0.0735	0.1757	[b]estimated from Fig. 2(a) in ref. [166]
				$Ti_{0.36}Al_{0.40}Ta_{0.24}N$	12	31.2[b]	420[b]	0.0744	0.1730	
				$Ti_{0.32}Al_{0.36}Ta_{0.32}N$	16	32.0[b]	400[b]	0.0800	0.2048	
				$Ti_{0.29}Al_{0.34}Ta_{0.37}N$	18.5	35.5[b]	380[b]	0.0934	0.3098	
				$Ti_{0.27}Al_{0.27}Ta_{0.46}N$	23	31.2[b]	360[b]	0.0868	0.2355	
				$Ti_{0.20}Al_{0.20}Ta_{0.60}N$	30	26.3[b]	354[b]	0.0742	0.1443	
Sui et al. [167]	Reactive magnetron sputtering	Si (100) (SEM, EDX and GIXRD), WC-8 wt.% Co (nano-indentation, oxidation test)	Constant at −50	$Ti_{0.44}Al_{0.56}N$	0	11.0[c]				[c]estimated from Fig. 4 in ref. [167]
				$Ti_{0.41}Al_{0.50}Ta_{0.09}N$	8.9	17.5[c]				
				$Ti_{0.37}Al_{0.42}Ta_{0.21}N$	21.1	31.2[c]				
				$Ti_{0.34}Al_{0.36}Ta_{0.30}N$	30.6	30.0[c]				
				$Ti_{0.31}Al_{0.32}Ta_{0.37}N$	37.2	28.5[c]				
Yang et al. [168]	Cathodic arc system	Low-alloy steel plates (SEM, EDX, EPMA, TEM and XRD characterization), W pieces (thermal annealing, nano-indentation), polycrystalline Al_2O_3 plates (SEM characterization, oxidation test)	Constant at −40	$Ti_{0.52}Al_{0.48}N$	0	30.9	484.6	0.0638	0.1256	
				$Ti_{0.40}Al_{0.54}Ta_{0.06}N$	6	26.2	317.5	0.0825	0.1784	
				$Ti_{0.34}Al_{0.54}Ta_{0.12}N$	12	24.9	301.6	0.0826	0.1697	
Grossmann et al. [169]	Cathodic arc evaporation	Polished cemented carbide disks (SEM, EDX and XRD characterization, ball-on-disc test), low alloy steel foil (thermal stability study)	Constant at −70	$Ti_{0.53}Al_{0.47}N$	0	32.5				Hardness values obtained from ref. [170]
				$Ti_{0.52}Al_{0.47}Ta_{0.01}N$	1	33.4				
				$Ti_{0.52}Al_{0.44}Ta_{0.04}N$	2.5	31.8				
				$Ti_{0.50}Al_{0.42}Ta_{0.08}N$	5	33.6				
				$Ti_{0.46}Al_{0.37}Ta_{0.17}N$	10	34.4				
				$Ti_{0.43}Al_{0.34}Ta_{0.23}N$	15	33.4				

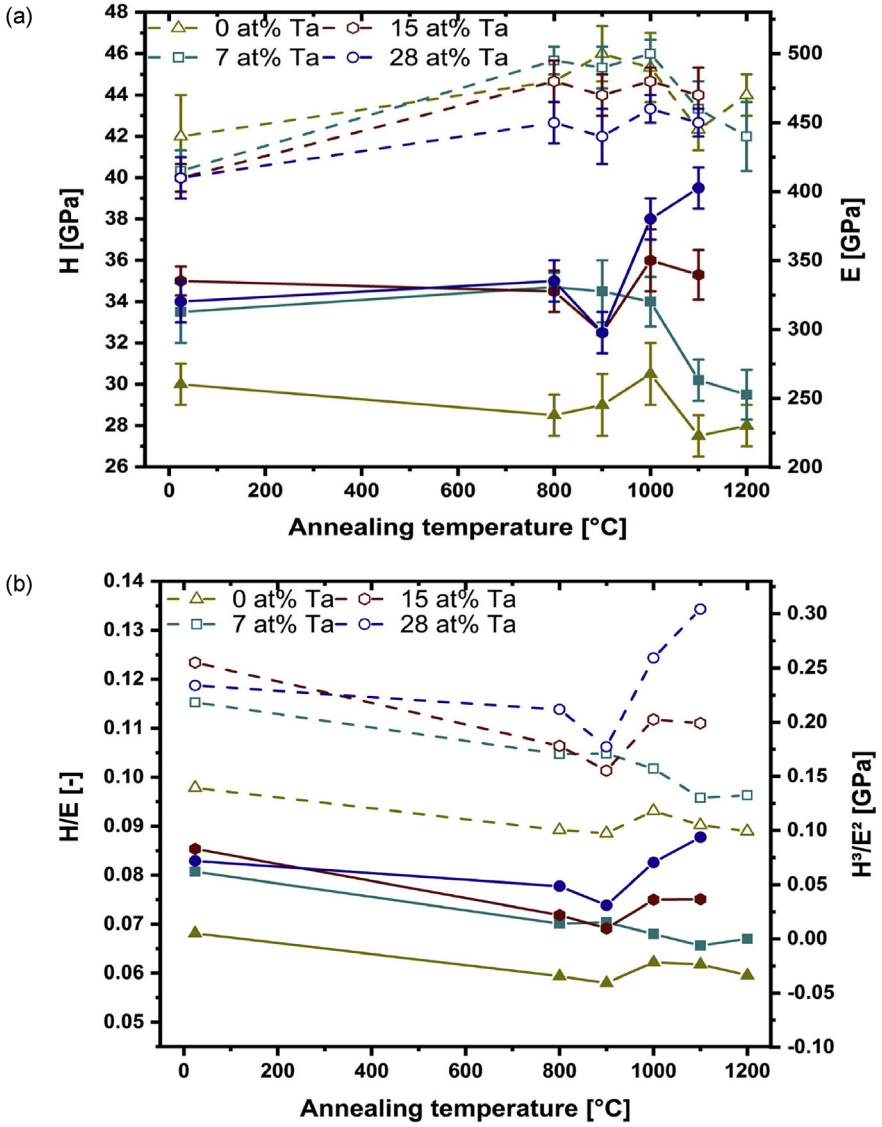

Fig. 16 – (a) Hardness (filled symbol) and modulus of elasticity (open symbol), (b) H/E ratio (filled symbol) and H^3/E^2 ratio (open symbol) of $Ti_{0.54}Al_{0.46}N$, $Ti_{0.38}Al_{0.34}Ta_{0.28}N$, $Ti_{0.44}Al_{0.41}Ta_{0.15}N$ and $Ti_{0.49}Al_{0.44}Ta_{0.07}N$ after vacuum annealing up to 1200 °C. Reprinted from Surface and Coatings Technology, 344, W.M. Seidl, M. Bartosik, S. Kolozsvári, H. Bolvardi, P.H.Mayrhofer, Improved mechanical properties, thermal stabilities, and oxidation resistance of arc evaporated Ti–Al–N coatings through alloying with Ta, 244–249, Copyright (2018), with permission from Elsevier [164].

diffusion [174–176]. Koller et al. [171] found that the $Ti_{0.54}Al_{0.46}N$ and $Ta_{0.89}Al_{0.11}N$ were fully oxidized after heating in ambient air at 850 °C for 20 h. The oxide layer was porous and had poor adhesion with the substrate (Fig. 18). In contrast, the $Ti_{0.45}Al_{0.36}Ta_{0.19}N$ coating was intact, with dense Al_2O_3 formed at the outer surface, protecting the underlying nitride layer from further oxidation. Ta also promoted the direct formation of stable r-TiO_2 during oxidation. This prevented the formation of a-TiO_2 and therefore the undesired phase transformation of a-TiO_2 to r-TiO_2. Transformation of a-TiO_2 to r-TiO_2 could result in volume shrinkage by 5–10%, leading to the formation of cracks and pores which served as diffusion paths for oxygen [40,177]. Hollerweger et al. [40,177], Sui et al. [167], and Yang et al. [168] attributed the high oxidation resistance of TiAlTaN to the absence of cracks and pores as well as to the early formation of dense Al_2O_3 on the surface, which played an important role in hindering the diffusion of oxygen and thus enhancing the oxidation resistance. The addition of Ta in TiAlN raised the onset oxidation temperature by more than 100 °C [167,168]. Sui et al. [167] found that $Ti_{0.44}Al_{0.56}N$ with a relatively high number of pores was fully oxidized at 600 °C to form a-TiO_2 and r-TiO_2. These oxides transformed into the stable r-TiO_2 and Al_2O_3 at 800 °C. Oxides formed on $Ti_{0.37}Al_{0.42}Ta_{0.21}N$ were mainly Al_2O_3, with a small amount of r-TiO_2. However, excessive Ta content was found to increase lattice distortion and to reduce its effectiveness in

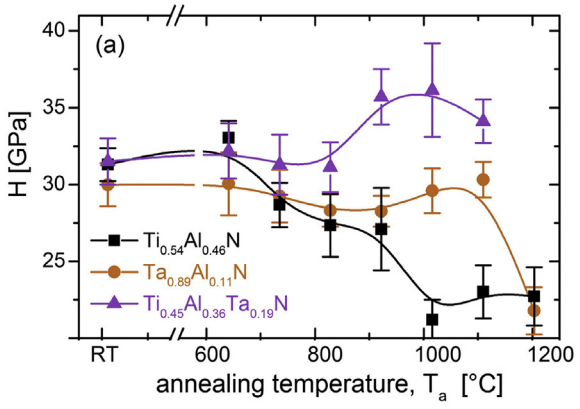

Fig. 17 – Hardness evolution as a function of the vacuum annealing temperature of $Ti_{0.54}Al_{0.46}N$, $Ta_{0.89}Al_{0.11}N$, and $Ti_{0.45}Al_{0.36}Ta_{0.19}N$ coatings. Reprinted from Surface and Coatings Technology, 259, C.M. Koller, R. Hollerweger, C. Sabitzer, R. Rachbauer, S.Kolozsvári, J. Paulitsch, P.H. Mayrhofer, Thermal stability and oxidation resistance of arc evaporated TiAlN, TaAlN, TiAlTaN, and TiAlN/TaAlN coatings, 599–607, Copyright (2014), with permission from Elsevier [171].

preventing the formation of a-TiO_2, hence allowing the transformation of this phase to r-TiO_2 to occur and causing the coating to crack and spall.

Khetan et al. [178] found that below 700 °C, the oxidation mechanism of AlTiTaN coatings was governed by inward diffusion of O to form an amorphous oxide layer. Above 750 °C, the outward diffusion of Al and inward diffusion of O occurred simultaneously to form a bilayer oxide comprising an Al_2O_3 layer with an underlying AlTiTa oxide layer. Above 750 °C, the AlTiTa oxide layer crystallized into the rutile phase and grain boundaries with more defects were formed. These grain boundaries provided pathways for the outward diffusion of Al to form Al_2O_3 oxide on the top surface, acting as a diffusion barrier against oxidation up to 900 °C. Rapid oxidation occurred above 900 °C which was due to the decomposition of c-TiTaN and c-AlN phases and the accelerated inward diffusion of oxygen induced by high thermal energy.

However, increasing Ta content could reduce the proportion of Al in the coating and promote the formation of dense TiO_2, which hindered the outward diffusion of Al [169]. This subsequently reduced the thickness of Al_2O_3, which could protect the coatings from further oxidation. These results showed that Al and Ta content must be well-balanced to allow the rapid formation of Al_2O_3 and the direct formation of r-TiO_2 to occur. In the sliding tests carried out at room temperature, the coatings with greater Ta content (and therefore hardness) exhibited a higher COF. With increasing temperature, the COF of TiAlTaN decreased due to the formation of sub-stoichiometric r-$(Ti,Ta)_nO_{2n-1}$ and Magnéli phase. Magnéli phase was formed due to reduced oxygen vacancies in the coating from the presence of Ta. The Magnéli phase, with low-shear crystallographic planes and reduced bond strength, is known to reduce friction [179,180]. However, when the oxygen deficiency exceeded a critical limit due to excessive Ta content, a change in the crystallographic shear planes would take place, resulting in increased bond strength and COF [180,181]. However, increasing the Ta content resulted in increased abrasion wear due to the formation of Ta_2N.

Pfeiler et al. [172] investigated the influence of the bias voltage used in the coating deposition on the tribological behaviour of TiAlTaN coatings at various temperatures. This variation of the bias voltage had no influence on the tribological behaviour at room temperature, where moisture promoted the rapid formation of Al_2O_3 and hence oxidation wear. At 500 °C, the effect of bias voltage was pronounced, with the width of the wear track increasing with decreasing bias voltage. Low bias voltage produced high-density droplets on the as-deposited coatings, which acted as sharp tips and induced severe abrasion on the ball. At 700 °C, since wear was governed by the oxidation resistance of the coatings, wear decreased with increasing bias voltage due to the depletion of hcp structure.

5.2. *Mechanical and tribological behaviour of TiAlTaN multilayer coatings*

The TiAlTaN multilayer coatings reported to date have had a maximum hardness of 20.0–31.6 GPa (Table 8) with a mean of 25.8 GPa. During the early stage of deposition, the TiAlTaN monolayer coatings displayed fine-grained structure before evolving into columnar structure with increasing diameter. With Ta layers, the re-nucleation and growth of the columnar crystal moved to the interfaces. The growth became increasingly difficult at smaller bilayer thicknesses. This effect explained the reduction in the columnar crystal size, and thus the surface roughness, when the Λ of the TiAlTaN/Ta multilayer coatings ranged from 1000 to 140 nm. This increase in the hardness from 16 to 20 GPa with a reduction in the Λ could be attributed to the reduction in the columnar diameter (the Hall-Petch effect) and the greater number of interfaces which effectively obstructed dislocation motion. Whenever the TiAlTaN/Ta multilayer coating did not peel off (which was found to occur when it was too thick), it produced a lower COF than the TiAlTaN monolayer [182].

The roughness, grain size and residual stress of the (Ti,Al)N/TaN multilayer coating were found to reduce with decreasing Λ from 62.92 to 4.59 nm. The compressive residual stress decreased from 3.97 to 1.51 GPa, respectively. These values were significantly lower than those measured for the TiAlN (7.09 GPa) and TaN (8.66 GPa) monolayer coatings. However, the effect of residual stress on the hardness and adhesion properties of the coatings has not been investigated. The (Ti,Al)N and TaN monolayer coatings with an fcc crystal structure exhibited growth in the [111,200] directions, respectively. For the (Ti,Al)N/TaN multilayer coating, both (Ti,Al)N and TaN showed preferential growth in the [111] direction [183].

Contreras Romero et al. [184] produced nanostructured TiAlTaN-(TiAlN/TaN)n coatings with varying volume fractions of TiAlTaN on top of TiAlN/TaN multilayer layers. The mechanical and tribological behaviour of the samples with TiAlT and TiAlN/TaN volume fractions of 23/77, 48/52, 66/34 and 84/16 were investigated. The coatings with 23/77 and 48/52

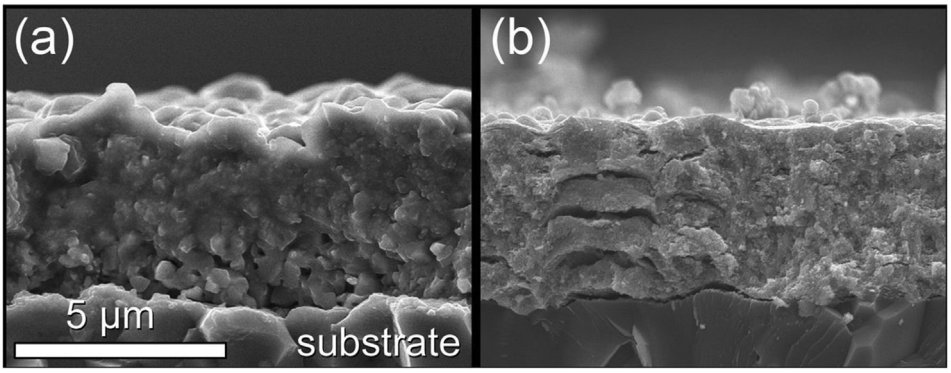

Fig. 18 – Monolithically grown of (a) $Ti_{0.54}Al_{0.46}N$ and (b) $Ta_{0.89}Al_{0.11}N$ coatings after oxidation in ambient air at 850 °C for 20 h. The oxide layer was porous and had poor adhesion. Reprinted from Surface and Coatings Technology, 259, C.M. Koller, R. Hollerweger, C. Sabitzer, R. Rachbauer, S.Kolozsvári, J. Paulitsch, P.H. Mayrhofer, Thermal stability and oxidation resistance of arc evaporated TiAlN, TaAlN, TiAlTaN, and TiAlN/TaAlN coatings, 599–607, Copyright (2014), with permission from Elsevier [171].

volume fractions exhibited the rock-salt-like crystalline structure of TiN, with preferential growth in [111] direction, suggesting the formation of TiAlTaN solid solution. TiAlTaN was harder than TiAlN/TaN, with values of 32.1 GPa and 24.7 GPa, respectively, which explained the increase in the TiAlTaN-(TiAlN/TaN) coating's hardness with an increase in the volume fraction of TiAlTaN from 23/77 to 84/16. This increase coincided with a reduction in the adhesion strength due to greater residual compressive stress: the coating with 84/16 volume fraction had compressive stress close to that of the TiAlTaN. The COF and wear rate increased from 0.59 to 0.84 and 3.5×10^{-4} to 7×10^{-4} mm^3/N, respectively, with an increase in the volume fraction of TiAlTaN.

6. Review of TiAlBN coatings

6.1. *Mechanical, thermal stability, oxidation and tribological behaviour of TiAlBN monolayer coatings*

The maximum hardness, H/E and H^3/E^2 of TiAlBN coatings achievable by various deposition methods were 27.0–42.14 GPa, 0.0842–0.1204 and 0.0928–0.6109 GPa, respectively (Figs. 19 and 20, and Table 9), with means of 31.2 ± 6.6 GPa, 0.1059 ± 0.0123 and 0.3623 ± 0.1521 GPa. Baker et al. [41] studied the microstructure of the as-deposited TiAlBN coatings using various chemical compositions, with results as shown in Table 10. All coatings had nanocrystalline (Ti,Al)N grains (by substitution of Ti with Al in the TiN phase) separated by intergranular amorphous BN (a-BN) phase and a small amount of TiB_2. The average (TiAl)N grain size reduced with decreasing (Ti,Al)N/BN phase ratio. As the ratio approached unity, competitive grain growth occurred, which resulted in the formation of the smallest grain size. An earlier study found that although a reduction in the Ti/B ratio decreased grain size, lower coating hardness was observed [185] (Table 9). This reduction in hardness was attributed to the increasing amount of a-BN phase (due to increasing B content), which was relatively soft as compared to other phases such as AlN, TiN, and TiB_2 [186,187]. All TiAlBN coated cutting tools exhibited longer life than the TiAlN coated tools in the wet drilling of P20 steel and this tool life increased linearly with the (Ti,Al)N fraction, as shown in Fig. 21. It was concluded that the softer BN phase had also contributed to the enhanced toughness and wear resistance of the coatings by permitting some degree of (Ti,Al)N grain displacement under load [41]. Morales-Hernandez et al. [188] investigated the mechanical properties of TiAlBN coatings with different chemical compositions. The fraction of nanocrystalline $(Ti_{1-x}Al_x)N$ phase, a-BN and a-TiB_2 (Table 11), and the microstructure of $(Ti_{1-x}Al_x)N$ appeared to be governed by Al content. However, the structure of (TiAl)N had a greater influence on the mechanical properties of the coatings. The M5 and M6 coating samples, with relatively small values of x (0.50 and 0.53) and dominated by $(Ti_{1-x}Al_x)N$ with a rock salt type (B1–NaCl) structure, exhibited the highest values of hardness and elastic modulus (Fig. 22). In contrast, inferior mechanical properties were measured for the M1, M2, M3 and M4 samples with dominant $(Ti_{1-x}Al_x)N$ phase and wurtzite-type structure. With the exception of the M4 sample (with $x = 0.52$), the M1, M2 and M3 samples had higher values of x (1.0, 0.70, and 0.67, respectively). The M3 sample, which gave the highest XRD peak associated with wurtzite-type structure and the lowest peak associated with rock salt type structure (Fig. 23), had the lowest hardness and elastic modulus. Baker et al. [187] reported that the superior hardness produced for (Ti,Al)$B_{0.92}N_{1.83}$ and (Ti,Al)$B_{0.29}N_{0.46}$ was associated with their high (Ti,Al)N content, which gave rise to the formation of (Ti,Al)$(N,B)_{1-x}$ grains with an amorphous titanium boride monolayer coverage (Table 9).

Nitrogen concentration had a significant effect on the mechanical properties of the coating. Higher nitrogen concentration resulted in more a-BN phase, which being formed at the expense of TiB2, led to a reduction in the hardness and modulus of elasticity (Fig. 20). The best adhesion was obtained when both the coating and the substrate had a similar elastic modulus. Coatings with a higher B/A ratio, which also had higher B content, required a lower concentration of nitrogen

Table 8 – Summary of the deposition method and parameters, substrate, description of coating, hardness, Young's modulus and *H/E* of TiAlTaN multilayer coatings.

Ref.	Deposition method	Substrate	Description of coating	Hardness (GPa)	Young's Modulus (GPa)	H/E	Remark
Sui et al. [182]	Reactive magnetron sputtering	WC-8 wt.% Co (SEM, EDX and AFM characterization, nano-indentation, friction and scratch tests)	TiAlTaN monolayer	16.0			
			TiAlTaN/Ta multilayer with bilayer thickness (nm) of:				
			1000	17.5			
			140	20.0			
Contreras Romero et al. [184]	DC magnetron sputtering	AISI M2 steel (SEM, TEM and FIB characterization, nano-indentation, scratch and ball-on-disc tests), steel foils (XRD characterization), Si Nb-doped (100) (residual stress measurement)	TiAlTaN monolayer	32.01	430	0.0744	[a]estimated from Fig. 9 in ref. [184] [+]Calculated based on E*
			TiAlN/TaN multilayer	24.70	350	0.0706	
			TiAlTaN/(TiAlN/TaN) with volume fraction of (vol%):				
			23/77	27[a]	298[a]	0.0906[+]	
			48/52	28.8[a]	297[a]	0.0971[+]	
			66/34	30.4[a]	310[a]	0.0981[+]	
			84/16	31.6[a]	316[a]	0.1000[+]	

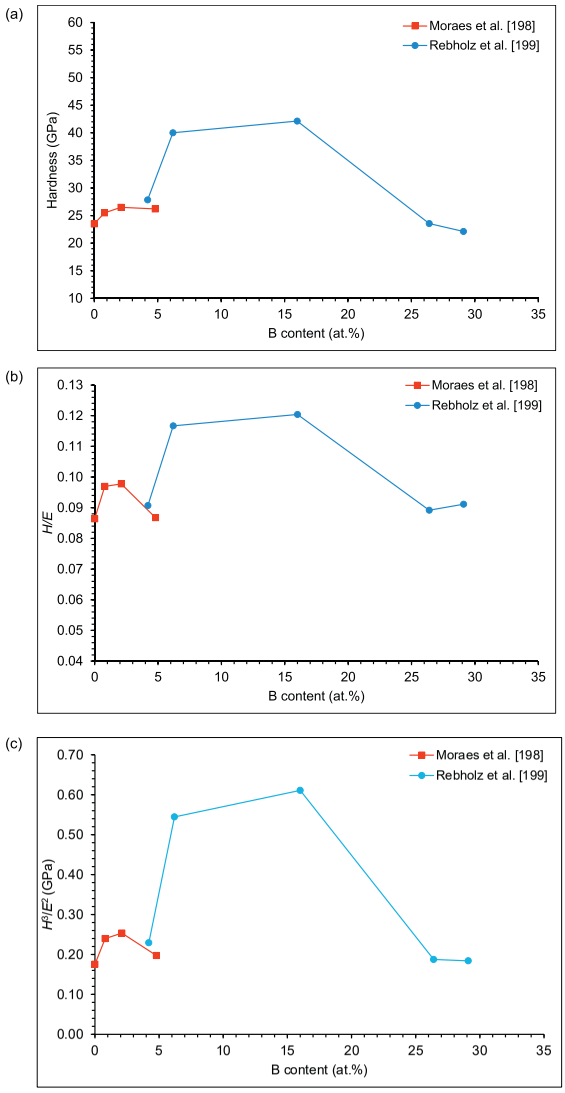

Fig. 19 – Comparison of the (a) hardness, (b) *H/E* and (c) H^3/E^2 ratio for TiAlBN coatings deposited by various deposition techniques as a function of B content (at.%).

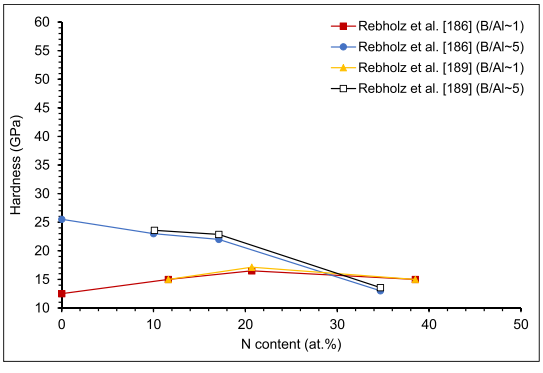

Fig. 20 – Hardness of the TiAlBN coatings deposited by magnetron sputtering as a function of N content (at.%).

Table 9 – Summary of the deposition method and parameters, substrate, description of coating, elemental composition, and hardness, Young's modulus, H/E and H^3/E^2 of TiAlBN monolayer coatings.

Ref.	Deposition method	Substrate	Description of coating	B content (at.%)	Ti content (at.%)	Al content (at.%)	N content (at.%)	BN content (at.%)	Hardness (GPa)	Young's Modulus (GPa)	H/E	H^3/E^2 (GPa)	Remark
Rebholz et al. [185]	Twin-crucible evaporation system	Si (100) wafers (SEM, GDOS and GAXRD characterization), AISI 316 stainless steel (nano-indentation), M2 tool steel (scratch test), HSS twist drills (machining)	$Ti_{0.12}Al_{0.14}B_{0.34}N_{0.40}$ (Ti/B = 0.34)					45.5	17[a]	210[a]	0.0810	0.1141	[a]estimated from Fig. 4(a) in ref. [185]
			$Ti_{0.21}Al_{0.11}B_{0.27}N_{0.41}$ (Ti/B = 0.76)					33.1	17[a]	240[a]	0.0708	0.0853	
			$Ti_{0.23}Al_{0.10}B_{0.25}N_{0.42}$ (Ti/B = 0.92)					29.4	20[a]	260[a]	0.0769	0.1183	
			$Ti_{0.30}Al_{0.12}B_{0.17}N_{0.41}$ (Ti/B = 1.73)					10.8	31[a]	320[a]	0.0969	0.2909	
			$Ti_{0.34}Al_{0.11}B_{0.15}N_{0.40}$ (Ti/B = 2.31)					2.4	37[a]	320[a]	0.1156	0.4947	
Rebholz et al. [186]	Magnetron sputtering	Si (100) wafers (SEM, GDOES, GAXRD and XPS characterization), AISI 316 stainless-steel (nano-indentation, scratch and pin-on-disc tests)	B/Al~1	22	18	21.5	38.5		15.0[b]	196[b]	0.0765	0.0879	[b]estimated from Fig. 6 in ref. [186]
			B/Al~1	28.3	23.0	28.0	20.7		16.5[b]	220[b]	0.0750	0.0928	
			B/Al~1	30.4	27.0	31.0	11.6		15.0[b]	196[b]	0.0765	0.0879	
			B/Al~1	33.5	33.0	33.5	0		12.5[b]	188[b]	0.0665	0.0553	
			B/Al~5	40.3	20.0	5.0	34.7		13.0[b]	172[b]	0.0756	0.0743	
			B/Al~5	49.9	25.0	8.0	17.1		22.0[b]	265[b]	0.0830	0.1516	
			B/Al~5	52.0	28.0	10.0	10.0		23.0[b]	290[b]	0.0793	0.1447	
			B/Al~5	57.0	32.0	11.0	0		25.5[b]	245[b]	0.1041	0.2762	
Baker et al. [187]	Electron beam evaporating	AISI 316 stainless steel (XPS, GAXRD and TEM characterization, nano-indentation)	$(Ti,Al)B_{1.82}N_{1.78}$	39.6	15.3	6.4	38.7	55	23[c]	220[c]	0.1045	0.2514	[c]estimated from Fig. 7 in ref. [187]
			$(Ti,Al)B_{1.75}N_{2.49}$	33.4	12.1	7.0	47.5	58	22[c]	225[c]	0.0978	0.2103	
			$(Ti,Al)B_{0.92}N_{1.83}$	24.5	21.6	5.1	48.8	47	32[c]	283[c]	0.1131	0.4091	
			$(Ti,Al)B_{0.66}N_{0.25}$	34.5	47.9	4.4	13.2		26[c]	262[c]	0.0990	0.2551	
			$(Ti,Al)B_{0.29}N_{0.46}$	16.8	52.4	4.6	26.2		32[c]	295[c]	0.1085	0.3765	
Rebholz et al. [189]	Reactive magnetron sputtering	Si (100) wafers (SEM, GDOES, XPS, XRD and TEM characterization), AISI 316 stainless-steel (nano-indentation)	B/Al~1	23.9	17.6	20.0	38.5		15.0[d]	200[d]	0.0750	0.0844	[d]estimated from Fig. 4 in ref. [189]
			B/Al~1	29	21.7	28.6	20.7		17.1[d]	221[d]	0.0774	0.1027	
			B/Al~1	30.1	26.1	32.2	11.6		15.0[d]	200[d]	0.0750	0.0844	
			B/Al~5	40.2	19.4	5.7	34.7		13.6[d]	171[d]	0.0792	0.0850	
			B/Al~5	50.3	24.5	8.1	17.1		22.9[d]	271[d]	0.0842	0.1621	
			B/Al~5	52.1	27.4	10.4	10.1		23.6[d]	290[d]	0.0813	0.1557	
Moraes et al. [198]	Magnetron sputtering	100 oriented Si (SEM, EDX, XPS and XRD characterization), AISI Fe-foil (thermal stability study), 1−102 oriented sapphire (nano-indentation)	$Ti_{0.31}Al_{0.69}N$	0	16.1	36.5	47.4		23.5[e]	272[e]	0.0863	0.1754	[e]estimated from Fig. 4 in ref. [198]
			Ti−Al−2B−N	0.8	12.2	38.8	49.0		25.5[e]	263[e]	0.0970	0.2397	
			Ti−Al−5B−N	2.1	11.4	36.6	49.9		26.5[e]	271[e]	0.0978	0.2534	
			Ti−Al−10B−N	4.8	13.1	34.0	48.1		26.2[e]	302[e]	0.0868	0.1927	

(*continued on next page*)

Table 9 – (*continued*)

Ref.	Deposition method	Substrate	Description of coating	B content (at.%)	Ti content (at.%)	Al content (at.%)	N content (at.%)	BN content (at.%)	Hardness (GPa)	Young's Modulus (GPa)	H/E	H^3/E^2 (GPa)	Remark
Rebholz et al. [199]	Twin-crucible EB evaporation source system	Si (100) (SEM, XPS and GAXRD characterization), AISI 316 stainless steel (thermal annealing study, nano-indentation) and AISI M2 tool steel (high-temperature stability study)	$(Ti,Al)B_{0.09}N_{1.07}$	4.2	39.1	7.2	49.5		27.9[f]	307[f]	0.0907	0.2292	[f]estimated from Fig. 6(b) in ref. [199]
			$(Ti,Al)B_{0.14}N_{1.12}$	6.2	36.2	8.0	49.5		40.0[f]	343[f]	0.1167	0.5444	
			$(Ti,Al)B_{0.45}N_{1.37}$	16.0	25.3	10.1	48.6		42.1[f]	350[f]	0.1204	0.6109	
			$(Ti,Al)B_{1.02}N_{1.85}$	26.4	16.8	9.0	47.8		23.6[f]	264[f]	0.0892	0.1875	
			$(Ti,Al)B_{1.35}N_{2.30}$	29.1	10.1	11.4	49.4		22.1[f]	243[f]	0.0912	0.1840	

to form a-BN. The hardness of the coatings was reduced by a-BN (Fig. 20) [186,189]. Rebholz et al. [189] found that the modulus of elasticity, hardness, and density of TiAlBN coatings were governed by the phases present in the coatings and their chemical composition. Coatings consisting of TiB_2 and (Ti,Al)N phases exhibited high hardness, elastic modulus, and density. A linear correlation between the hardness and elastic modulus of the coatings was observed (Fig. 24(a)). A plot of hardness and elastic modulus vs density shows a strong linear correlation except for those coatings containing a significant amount of a-BN phase (Fig. 24(b)).

Rebholz et al. [190] found that the phase in the TiAlBN coatings was also governed by their Al content. Incorporating a small amount of Al (5–11 at.%) into TiBN resulted in the formation of a hexagonal BN (h-BN) phase. Sliding tests carried out using the TiAlBN coating with numerous amounts of h-BN and a-BN produced a low COF and wear rate on both the coating and the counter body material [186,190]. h-BN is a low-friction material with a lamellar structure similar to that of graphite and MoS_2 which can be used as a solid lubricant in various applications. The steady-state COF of 5 wt.% h-BN in vaseline was 0.08, which was lower than that of graphite grease and SFR (superior friction reduction) 2522 grease (0.12 and > 0.17, respectively) [191]. Water was found able to react with h-BN to form H_3BO_3, further reducing the COF [192]. Oxidation of BN with water vapour could result in the formation of B_2O_3 and subsequently a lubricious layer of boric acid, leading to a reduction in the COF [193]. Since the tribological performance of grease containing h-BN particles was greatly dependent on the particle size and the concentration of the h-BN, these two parameters could be optimised to produce COF and wear comparable to, or even lower than, those produced under graphite-grease lubrication [194]. Similarly, Mitterer et al. [195] found that adding a small amount of Al (2–6 at.%) promoted the formation of h-BN over c-BN, and the amount of h-BN increased with greater nitrogen content in the coatings.

However, h-BN was found to reduce the tool life of cutting tools [185]. In the wet drilling of P20 steel, the life of TiAlBN coated tools increased with higher Ti/B ratios, which also coincided with greater hardness due to a reduction in the amount of h-BN. The life of TiAlBN coated tools with high Ti/B ratios (1.73–2.31) and therefore low h-BN content was twice that of the TiAlN coated tools. BN can also exist in the form of wurtzite (w-BN). Pan et al. [196] reported that w-BN was harder than c-BN, with hardness comparable to that of diamond. However, Liu et al. [197] found that c-BN had higher hardness than the w-BN. Therefore, the transformation of the BN phase resulted in a change in hardness. Moraes et al. [198] found that the Al content at which the cubic-to-wurtzite structure transition occurred in the $(Ti_{1-x}Al_x)_{1-y}B_yN$ solid solution (B substituted for metals) reduced with greater B content. The formation energy for the wurtzite structure was significantly lower than that of the cubic structure at higher B concentration (Fig. 25). These effects were not seen with the $Ti_{1-x}Al_xB_yN_{1-y}$ solid solution (B substituted for nitrogen). The addition of B also caused the crystalline wurtzite phase to be embedded in the disordered region, leading to a reduction in grain size. The increase in hardness of the as-deposited coatings from 23 to 27 GPa (Table 9) with greater boron

Table 10 – The relative phase fraction, (Ti,Al)N/BN phase ratio, Ti/B ratio, and average (Ti,Al)N grain size for TiAlBN coatings with various chemical compositions [41].

Sample	Elemental (at. %)				Relative phase fraction (%)		(Ti,Al)N/BN phase ratio	Ti/B ratio	Average (Ti,Al)N grain size (μm)
	Ti	Al	B	N	(Ti,Al)N	BN			
40	10.1	11.4	29.1	49.4	45.9	52.2	0.88	0.35	3
60	16.8	9.0	26.4	47.8	54.6	42.3	1.29	0.64	7
80	25.3	10.1	16.0	48.6	–	–	–	1.58	21
90	26.2	8.0	6.2	49.5	88.2	10.8	8.17	4.23	26
100	39.1	7.2	4.2	49.5	90.1	8.4	10.73	9.30	35

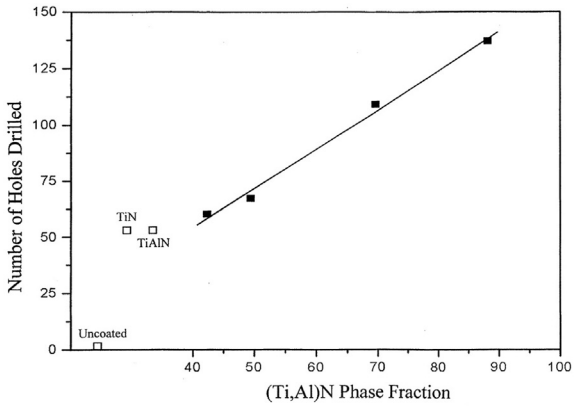

Fig. 21 – Tool life of TiAlBN coated tools with various (Ti,Al)N phase fractions. Reprinted from Surface and Coatings Technology, 151, M.A. Baker, S. Klose, C. Rebholz, A. Leyland, A. Matthews, Evaluating the microstructure and performance of nanocomposite PVD TiAlBN coatings, 338–343, Copyright (2002), with permission from Elsevier [41].

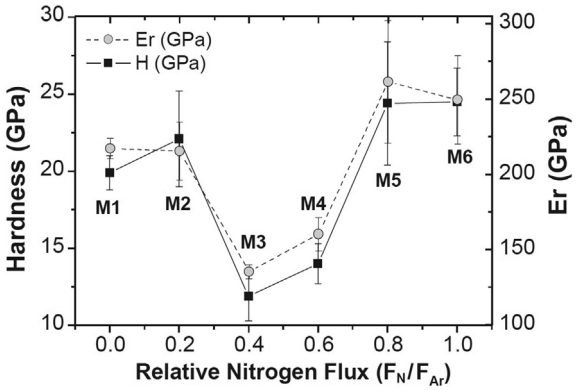

Fig. 22 – Nano hardness and modulus of elasticity (Er) for coating samples with various compositions produced by different F_N/F_{Ar} ratios. Reprinted from Vacuum, 76(2–3), J. Morales-Hernández, L. García-González, J. Muñoz-Saldaña, F.J.Espinoza-Beltrán, Structure and mechanical properties of (Ti,Al) (B,N) coatings fabricated by reactive DC magnetron sputtering, 161–164, Copyright (2004), with permission from Elsevier [188].

content could also be associated with the increase in cohesive strength. The hardness and elastic modulus of the wurtzite TiAlBN coatings increased continuously with higher annealing temperatures up to 1000 °C (Fig. 26). The densification of the disordered region encapsulating the wurtzite structure and a further increase in the cohesive strength could be attributed to the enhancement of these properties. In contrast, the hardness of the wurtzite TiAlN declined rapidly at temperatures above 600 °C. It was also found that the onset temperature at which mass-loss was detected (due to the release of N) increased from 1350 to 1450 °C with increasing B content from 0 to 10 at.%. Annealing of TiAlN resulted in an increase in grain size but this effect was not pronounced in the annealing of TiAlBN. Rebholz et al. [199] found that TiAlBN (with 6.2 and 26.4 at.% B) containing nc-(TiAl)N/a-BN exhibited high thermal stability upon annealing up to 900 °C, as indicated by only small variations in hardness and elastic modulus with annealing temperature (Fig. 27). The increase in the hardness with the initial temperature increase to 700 °C

Table 11 – The relative phase fraction, x value for $(Ti_{1-x}Al_x)N$, (Ti,Al)N/BN phase ratio, Ti/B ratio, and average (Ti,Al)N grain size for TiAlBN coatings with various chemical compositions [188].

Sample	Elemental (at. %)				Relative phase fraction (%)			x value for $(Ti_{1-x}Al_x)N$	(Ti,Al)N/BN phase ratio	Ti/B ratio	Average (Ti,Al)N grain size (μm)
	Ti	Al	B	N	TiB_2	(Ti,Al)N	BN				
M1	22.6	10.5	53.7	13.2	73.6	17.1	9.3	1.0	1.84	0.42	2.213
M2	18.7	8.7	45.0	27.6	44.8	24.9	30.3	0.70	0.82	0.42	2.607
M3	17.3	8.5	43.9	30.3	39.4	25.3	35.3	0.67	0.72	0.39	1.433
M4	17.1	7.5	40.5	35.0	30.1	29.1	40.8	0.52	0.72	0.42	1.146
M5	17.1	7.6	39.7	35.7	28.7	30.3	41.0	0.50	0.74	0.43	1.263
M6	16.2	7.7	40.2	36.0	28.0	29.1	42.9	0.53	0.68	0.40	1.795

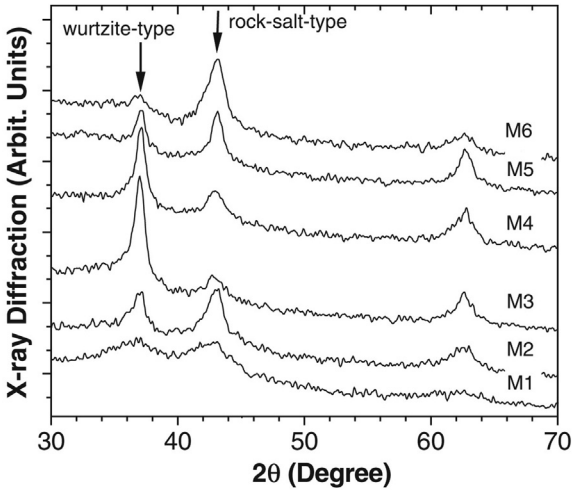

Fig. 23 – XRD analysis for coating samples with various compositions. Reprinted from Vacuum, 76(2–3), J. Morales-Hernández, L. García-González, J. Muñoz-Saldaña, F.J.Espinoza-Beltrán, Structure and mechanical properties of (Ti,Al) (B,N) coatings fabricated by reactive DC magnetron sputtering, 161–164, Copyright (2004), with permission from Elsevier [188].

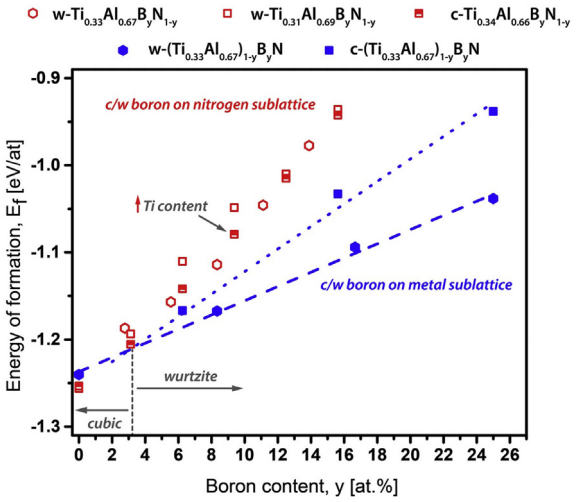

Fig. 25 – The energy of formation for cubic and wurtzite structured for $(Ti_{1-x}Al_x)_{1-y}B_yN$ and $Ti_{1-x}Al_xB_yN_{1-y}$ as a function of the boron content. Reprinted from International Journal of Refractory Metals and Hard Materials, 71, V. Moraes, H. Bolvardi, S. Kolozsvári, H. Riedl, P.H. Mayrhofer, Thermal stability and mechanical properties of Ti–Al–B–N thin films, 320–324, Copyright (2018), with permission from Elsevier [198].

was due to the self-hardening effect (i.e. the continuation of incomplete phase segregation during deposition via spinodal phase segregation) [200]. Upon further annealing, declining hardness may have been due to the oxidation of TiB_2 phases, the evaporation of BO_x, and the loss of B content [201].

7. Review of TiAlCrSiN coatings

7.1. *Mechanical, thermal stability, oxidation and tribological behaviour of TiAlCrSiN monolayer coatings*

The mechanical properties of TiAlCrSiN coatings produced by various deposition processes are shown in Table 12. The maximum hardness, H/E and H^3/E^2 of TiAlCrSiN achievable by varying the chemical composition were 31.0–34.4 GPa (with a mean of 32.8 ± 1.7 GPa), 0.1158 and 0.4424 GPa, respectively. Bobzin et al. [202] attributed the superior mechanical properties of the TiAlCrSiN coatings to the TiAlCrN nanocrystalline grains formed in the amorphous a-Si_3N_4 matrix, and to the strong cohesion between the nano-grains and matrix. Typically, the coating had small TiAlCrN grains with a diameter of less than 15 nm [202,203]. The CrTiAlSiN coatings produced by Kuo et al. [203] had higher hardness, fracture toughness, H/E and H^3/E^2 than CrTiAlN. Increasing the Si content from 0 to 8 at.% Si in CrTiAlSiN reduced the grain size from 12.4 to 5.8 nm, which occurred because the formation of the a-SiN_x phases and nanocrystalline TiSi

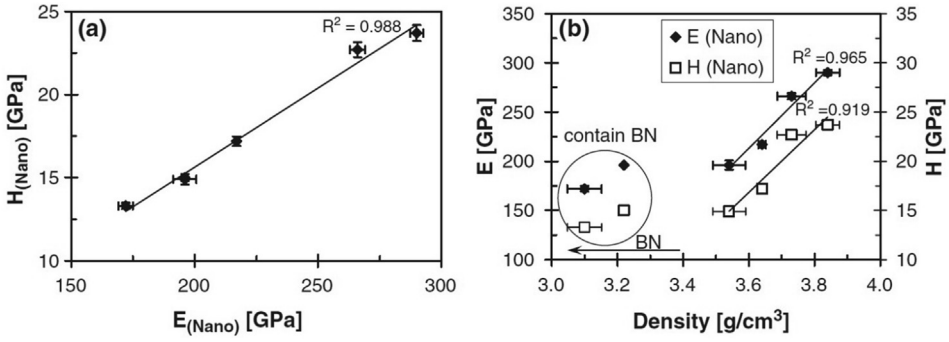

Fig. 24 – (a) Hardness vs elastic modulus, (b) Elastic modulus and hardness vs density for various TiAlBN coatings. Reprinted from Thin Solid Films, 514(1–2), C. Rebholz, A. Leyland, A. Matthews, C. Charitidis, S.Logothetidis, D. Schneider, Correlation of elastic modulus, hardness and density for sputtered TiAlBN thin films, 81–86, Copyright (2006), with permission from Elsevier [189].

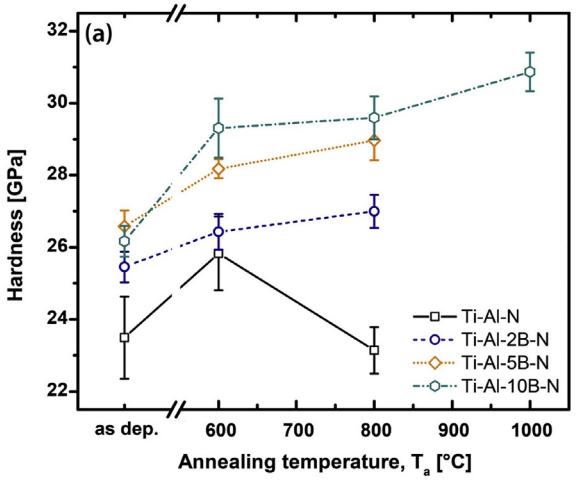

Fig. 26 – Variation in the hardness of TiAlN and TiAlBN coatings deposited from $(Ti_{0.33}Al_{0.66})_{1-y}B_y$ targets with annealing temperature. Reprinted from International Journal of Refractory Metals and Hard Materials, 71, V. Moraes, H. Bolvardi, S. Kolozsvári, H. Riedl, P.H. Mayrhofer, Thermal stability and mechanical properties of Ti–Al–B–N thin films, 320–324, Copyright (2018), with permission from Elsevier [198].

grains restricted grain growth. It was also found that increasing the Si content from 0.4 to 2.9 at.% altered the microstructure from a columnar to a dense structure. A nanocomposite microstructure was formed in the coating with 8 at.% Si. Coating hardness increased with Si content and reached the peak value at 1 at.% Si. This increased hardness was due to the solid solution hardening effect. Above this value, the solubility limit of Si in CrTiAlN was exceeded, leading to the segregation of softer a-SiN_x phase into the grain boundaries and thus a decrease in the hardness. The H/E, H^3/E^2 and K_c values showed a similar trend, meaning that the optimal toughness, H/E and H^3/E^2 could be obtained with an appropriate Si concentration. The variation in the wear resistance and COF exhibited by the CrTiAlN and CrTiAlSiN coatings with different Si content were due to more than just differences in their toughness, resistance to plastic deformation, and hardness. The amount of lubricious oxides (such as chromium oxide) produced was another important factor in this variation. As shown in Table 12, Cr content reduced from 33.5 to 25.3 at.% when Si content increased from 0 to 8.0 at.%, indicating that less chromium oxide was formed. Shen et al. [204] found that in the sliding of AlCrTiSiN coating, the lowest wear and COF were obtained in the test which produced the most Al_2O_3 and Cr_2O_3.

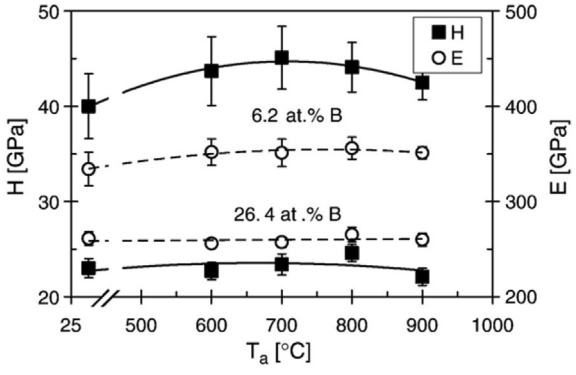

Fig. 27 – Variation in the hardness and elastic modulus for two coatings with nc-(Ti,Al)N/a-BN. Reprinted from Surface and Coatings Technology, 201(13), C. Rebholz, M.A. Monclus, M.A. Baker, P.H. Mayrhofer, P.N.Gibson, A. Leyland, A. Matthews, Hard and superhard TiAlBN coatings deposited by twin electron-beam evaporation, 6078–6083, Copyright (2007), with permission from Elsevier [199].

A similar grain size reduction to 5–10 nm by the addition of Si in the $Ti_xCr_yAl_zSi_{1-x-y-z}N$ coatings was also reported by Ichijo et al. [205]. Ezura et al. [206] and Ichijo et al. [205] investigated the effect of (Al + Si) ratio and bias voltage on the structure formed in $Ti_xCr_yAl_zSi_{1-x-y-z}N$ coatings. Coatings deposited using targets with an (Al + Si) ratio of between 0.56 and 0.60 had NaCl-type cubic structure. Higher ratios of between 0.67 and 0.69 produced a mixture of cubic and hexagonal structures. Ratios of above 0.69 produced wurtzite-type hexagonal structure (Table 12). Ezura et al. [206] found that increasing the bias voltage from −20 to −200 V increased the cubic to hexagonal phase ratio and the hardness of the $Ti_{0.20}Cr_{0.11}Al_{0.58}Si_{0.11}N$ coatings (Table 12). The phase and hardness change during annealing was greatly dependent on the chemical composition of the coatings. Increasing the annealing temperature from 800 to 1000 °C, $Ti_{0.20}Cr_{0.20}Al_{0.55}Si_{0.05}N$ (with cubic phase) exhibited an increase in micro-hardness due to the build-up of the coherency strain between the matrix (c-TiCrAlSiN phase) and newly-formed cubic (Ti,Cr)-rich and Al-rich phases. In contrast, stress relaxation occurred in the $Ti_{0.22}Cr_{0.22}Al_{0.44}Si_{0.12}N$ coating (with cubic phase), resulting in reduced micro-hardness. The $Ti_{0.20}Cr_{0.11}Al_{0.58}Si_{0.11}N$ (with both cubic and hexagonal phases) exhibited an increase in thermal stability and micro-hardness upon annealing regardless of (Al + Si) content due to the greater amount of cubic phase formed. Si increased the thermal stability of the coating at high temperatures by suppressing the formation of hcp-AlN through phase separation. Therefore, the coating retained its NaCl structure up to 1000 °C.

The variation in the bias voltage and pulse frequency in the coating deposition was found to have no significant influence on the chemical composition of the coating (Table 12) [202]. However, increasing the bias voltage from −110 to −160 V slightly increased the diameter of the grain from about 3.6 to 3.8 nm. Further increasing the bias voltage to −210 V led to a reduction in the diameter to about 3.2 nm. Reducing the frequency from 2000 to 500 Hz at a fixed voltage of −160 V increased the hardness and elastic modulus of the coating. The same effect was also seen when reducing the bias voltage from −210 to −110 V at a fixed pulse frequency f = 1000 Hz. Reducing the bias voltage also resulted in increased fracture toughness due to fewer lattice defects and to lower residual stress produced in the coating by lower kinetic energy ions. The maximum

Table 12 – Summary of the deposition method and parameters, substrate, description of coating, elemental composition, and hardness, Young's modulus, grain size, *H/E* and H^3/E^2 of TiAlCrSiN monolayer coatings.

Ref.	Deposition method	Substrate	Bias voltage (V) and pulse frequency (Hz)	Description of coating	(Si + Al) ratio	Si content (at.%)	Cr content (at.%)	Hardness (GPa)	Young's Modulus (GPa)	*H/E*	H^3/E^2 (GPa)	Grain size (nm)	Remark
Bobzin et al. [202]	Hybrid process consisting of direct current magnetron sputtering and high power pulsed magnetron sputtering (dcMS/HPPMS)	Tungsten carbide of grade HB10 (nano-indentation, scratch test), ball-nose cemented carbide end mills (machining). All samples were used in SEM, EDX, TEM, FIB and XRD characterization.	−160 V, 500 Hz	TiAlCrSiN		3.1	4.7	27.3	332.2	0.0822	0.1844	3.9	
			−160 V, 2000 Hz	TiAlCrSiN		2.3	4.5	24.5	303.8	0.0806	0.1593	4.2	
			−160 V, 1000 Hz	TiAlCrSiN		2.4	4.3	25.7	329.3	0.0780	0.1565	3.8	
			−210 V, 1000 Hz	TiAlCrSiN		2.4	4.1	23.2	295.9	0.0784	0.1426	3.2	
			−110 V, 1000 Hz	TiAlCrSiN		2.4	4.4	26.0	348.1	0.0747	0.1450	3.6	
Kuo et al. [203]	Magnetron co-sputtering	P-type (100) silicon wafers (FE-EPMA, GIXRD, XPS, FESEM, TEM and FIB characterization, residual stress, indentation toughness), AISI420 stainless steel discs (SEM and EDX characterization, nano-indentation, ball-on-disc test)	−200 V	CrTiAlN		0	33.5	28.8[a]	294[a]	0.0979	0.2764	12.4	[a]estimated from Fig. 11 in ref. [203]
			−150 V	CrTiAlSiN		0.4	32.8	32.4[a]	299[a]	0.1084	0.3804	11.9	
			−150 V	CrTiAlSiN		1.0	31.6	34.4[a]	304[a]	0.1132	0.4405	10.2	
			−150 V	CrTiAlSiN		1.6	29.1	33.5[a]	292[a]	0.1147	0.4409	8.7	
			−150 V	CrTiAlSiN		2.9	28.5	33.0[a]	285[a]	0.1158	0.4424	5.2	
			−150 V	CrTiAlSiN		8.0	25.3	30.7[a]	274[a]	0.1120	0.3854	5.8	
Ichijo et al. [205]	Cathodic arc method	Si substrate (SEM, TEM and XRD characterization), WC-Co (micro-indentation)	Not available	$Ti_{0.22}Cr_{0.22}Al_{0.44}Si_{0.12}N$ (c)	0.56			31.0[b]					[b]estimated from Fig. 3 in ref. [205]
				$Ti_{0.27}Cr_{0.13}Al_{0.53}Si_{0.07}N$ (c)	0.60			30.2[b]					
				$Ti_{0.20}Cr_{0.20}Al_{0.55}Si_{0.05}N$ (c)	0.60			29.8[b]					
				$Ti_{0.11}Cr_{0.22}Al_{0.61}Si_{0.06}N$ (c,h)	0.67			29.4[b]					
				$Ti_{0.20}Cr_{0.11}Al_{0.58}Si_{0.11}N$ (c,h)	0.69			29.0[b]					
				$Ti_{0.15}Cr_{0.15}Al_{0.62}Si_{0.08}N$ (h)	0.70			28.8[b]					
				$Ti_{0.12}Cr_{0.12}Al_{0.64}Si_{0.12}N$ (h)	0.76			26.0[b]					
				(c) – cubic phase (h) – hexagonal phase									
Ezura et al. [206]	Cathodic arc method	Mirror- polished WC-Co (EDX, TEM and XRD characterization, micro-indentation, thermal stability study)	−200 V	$Ti_{0.22}Cr_{0.22}Al_{0.44}Si_{0.12}N$ (c)	0.56	4.6	11.3	33					
			−200 V	$Ti_{0.27}Cr_{0.13}Al_{0.53}Si_{0.07}N$ (c)	0.60	3.6	7.3	32					
			−200 V	$Ti_{0.20}Cr_{0.20}Al_{0.55}Si_{0.05}N$ (c)	0.60	2.0	11.2	32					
			−200 V	$Ti_{0.11}Cr_{0.22}Al_{0.61}Si_{0.06}N$ (c,h)	0.67	3.0	11.9	31					
			−20 V	$Ti_{0.20}Cr_{0.11}Al_{0.58}Si_{0.11}N$ (c,h)	0.69	4.4	5.5	23					
			−100 V	$Ti_{0.20}Cr_{0.11}Al_{0.58}Si_{0.11}N$ (c,h)	0.69	4.6	5.4	25					
			−200 V	$Ti_{0.20}Cr_{0.11}Al_{0.58}Si_{0.11}N$ (c,h)	0.69	4.8	5.7	32					
			−200 V	$Ti_{0.15}Cr_{0.15}Al_{0.62}Si_{0.08}N$ (h)	0.70	6.4	5.4	29					
			−200 V	$Ti_{0.12}Cr_{0.12}Al_{0.64}Si_{0.12}N$ (h)	0.76	4.9	6.2	28					
				(c) – cubic phase (h) – hexagonal phase									

Siwawut et al. [211]	Filtered cathodic arc process	Co-WC inserts (SEM, EDX and XRD characterization, nano-indentation, machining)	Constant bias voltage of −75 V	CrTiAlSiN	0.9	13.0	26.1	233.4	0.1118	0.3264
				TiAlSiN	1.2	6.6	29.8	288.1	0.1034	0.3188
Khanchaiyaphum et al. [212]	Filtered cathodic arc	AISI 316 stainless steel (SEM, EDX and XRD characterization, nano-indentation and soft-sliding test)	−100 V	TiN			26.4			
			−75 V	TiAlSiN			31.6			
			−75 V	TiCrAlSiN			30.4			

hardness, H/E and H^3/E^2 obtained by varying the bias voltage were 26.0–33.0 GPa (with a mean of 29.5 GPa), 0.0784 and 0.1565 GPa, respectively. The deposition parameters were optimized to produce a coating with the highest hardness and fracture toughness, which led to the highest abrasive wear resistance for the cemented carbide tool in the milling of high-speed steel AISI M3-2. The volume Q removed by abrasive wear by brittle fracture decreases with an increase in the fracture toughness (K_c) and hardness (H), and is defined as [207]:

$$Q = N\frac{w^{5/4}}{K_c^{3/4}H^{1/2}} \quad (1)$$

where α is a constant, N is the number of particles in contact with the surface, w is the normal load on the particle. The constant α depends on the particle shape.

Chang and Hsiao [208] observed that CrTiAlSiN had a grain size of between 8–12 nm. Oxidation of this coating involved the diffusion of Ti to the surface to form TiO_2. CrAlSiN exhibited better oxidation resistance than CrTiAlSiN due to the absence of fast-forming TiO_2. TiO_2 grew faster than Al_2O_3 and Cr_2O_3 due to its higher oxidation parabolic rate constant. Cracks generated in the Al_2O_3 and Cr_2O_3 (due to the different coefficients of thermal expansion of the coatings and oxides) accelerated the diffusion of Ti to the surface to form undesirable TiO_2. Kim and Lee [209] found that TiAlCrSiN formed an outer TiO_2 layer, a middle Al_2O_3 layer, and an inner (Cr_2O_3, SiO_2)-rich layer after being exposed to a temperature of 1000 °C for 30 h. Prolonging the oxidation time to 70 h resulted in the formation of (Ti, Cr, Fe)-rich oxide underneath these oxide layers. This coating had high oxidation resistance owing to the slow growth of both the highly stoichiometric Al_2O_3, Cr_2O_3, and SiO_2, and also nonstoichiometric TiO_2 compounds. A similar oxide layer structure was seen in TiAlCrSiN deposited on WC-20TiC-10Co substrate after being oxidized at 900 °C for 10 h, indicating that it too had a good oxidation resistance [210]. However, at 1000 °C, the increasing oxidation rate and partial oxidation of the WC substrate formed a thicker and more fragile oxide layer.

In the dry face milling of cast iron, the CrTiAlSiN-coated tungsten carbide tools suffered coating delamination and thermal cracking due to a large difference in the thermal expansion coefficient of the coating and substrate. The TiAlSiN-coated tools suffered higher flank wear rate due to abrasion, low resistance to plastic deformation, and high chemical affinity between the coating with the workpiece [211]. Khanchaitaphum et al. [212] compared the wear resistance of TiN, TiAlSiN, and TiCrAlSiN coated hooks under dry sliding against nylon fibres. The wear of the coated hooks was due to adhesive wear involving the transfer of fibre onto the coated surface, and to subsequent detachment of the transfer film together with the coating. The high adhesive wear resistance exhibited by the TiAlSiN and TiCrAlSiN coatings (compared to TiN) was due to more than their high hardness since the TiAlSiN coating exhibited greater wear resistance despite both possessing similar hardness values. It was suggested that the wear of the coating was also governed by the type of oxide formed.

Table 13 – The range and mean of the maximum hardness, H/E and H^3/E^2 of the TiAlXN monolayer coatings obtained by varying the chemical composition in various deposition techniques.

	TiAlSiN	TiAlCrN	TiAlVN	TiAlTaN	TiAlBN	TiAlCrSiN
Range of the max. hardness (GPa)	24.4–57.0	26.0–40.9	27.5–46.0	26.2–35.5	27.0–42.1	31.0–34.4
Mean of the max. hardness (GPa)	38.9 ± 9.1	32.1 ± 4.7	36.8[a]	32.3 ± 3.4	31.2 ± 6.6	32.8 ± 1.7
Range of the max. H/E	0.0713–0.1164	0.0625–0.1252	0.0871	0.0826–0.0934	0.0842–0.1204	0.1158
Mean of the max. H/E	0.0922 ± 0.0105	0.0760 ± 0.0132	0.0871[a]	0.0871 ± 0.0046	0.1059 ± 0.0123	0.1158[a]
Range of the max. H^3/E^2 (GPa)	0.1957–0.4333	0.1085–0.3616	0.1698	0.1784–0.3098	0.0928–0.6109	0.4424
Mean of the max. H^3/E^2 (GPa)	0.3291 ± 0.0738	0.2146 ± 0.1073	0.1698[a]	0.2478 ± 0.0539	0.3623 ± 0.1521	0.4424[a]

[a] Standard deviation is not computed due to lack of data.

Table 14 – The range and mean of the maximum hardness, H/E and H^3/E^2 of the TiAlXN monolayer coatings obtained by varying the bias voltage in various deposition techniques.

	TiAlSiN	TiAlCrN	TiAlVN	TiAlTaN	TiAlBN	TiAlCrSiN
Range of the max. hardness (GPa)	27.1–42.2	35.0–50.0	38.5–43.3	Not available	Not available	26.0–33.0
Mean of the max. hardness (GPa)	35.2 ± 3.5	42.5[a]	40.9[a]	Not available	Not available	29.5[a]
Range of the max. H/E	0.0844–0.0881	Not available	0.0791–0.0807	Not available	Not available	0.0784[a]
Mean of the max. H/E	0.0863[a]	Not available	0.0799[a]	Not available	Not available	0.0784[a]
Range of the max. H^3/E^2 (GPa)	0.1825–0.2341	Not available	0.2333–0.2801	Not available	Not available	0.1565[a]
Mean of the max. H^3/E^2 (GPa)	0.2083[a]	Not available	0.2567[a]	Not available	Not available	0.1565[a]

[a] Standard deviation is not computed due to lack of data.

Table 15 – The range and mean of maximum hardness, H/E and H^3/E^2 obtained for the TiAlXN multilayer coatings.

	TiAlSiN	TiAlCrN	TiAlVN	TiAlTaN	TiAlBN	TiAlCrSiN
Range of the max. hardness (GPa)	20.8–42.8	19.8–38.4	28.3–38.4	20.0–31.6	Not available	Not available
Mean of the max. hardness (GPa)	34.1 ± 6.1	31.3 ± 6.3	34.1 ± 3.8	25.8[a]	Not available	Not available
Range of the max. H/E	0.0662–0.1119	0.0422–0.1191	Not available	0.0981[a]	Not available	Not available
Mean of the max. H/E	0.0885 ± 0.0132	0.0839 ± 0.0282	Not available	0.0981[a]	Not available	Not available
Range of the max. H^3/E^2 (GPa)	0.1271–0.3883	0.0353–0.5427	Not available	Not available	Not available	Not available
Mean of the max. H^3/E^2 (GPa)	0.2598 ± 0.0829	0.2706 ± 0.1984	Not available	Not available	Not available	Not available

[a] Standard deviation is not computed due to lack of data.

8. Conclusions

8.1. *Comparison of mechanical properties*

Table 13 shows the range and the mean of the maximum hardness, H/E and H^3/E^2 of the TiAlXN monolayer coatings obtained by varying the chemical composition in various deposition techniques. The achievable maximum hardness of the TiAlSiN monolayer coatings (57.0 GPa) was higher than other coatings. It also possessed the highest maximum hardness mean (38.9 ± 9.1 GPa). These values were higher than those produced via voltage optimization (42.2 GPa and 35.2 ± 3.5 GPa, respectively) (Table 14). In contrast, the values produced for the TiAlCrN coatings via voltage optimization were much higher. These results demonstrated the pronounced ability of Si to enhance coating hardness. The achievable maximum hardness and the mean of the maximum hardness obtained for the multilayer coatings (Table 15) were lower than those of the monolayer coatings (Table 13). The achievable maximum H/E and H^3/E^2 (0.1164 and 0.4333 GPa, respectively), and the mean of the maximum H/E and H^3/E^2 (0.0922 ± 0.0105 and 0.3291 ± 0.0738 GPa, respectively) obtained for the TiAlSiN monolayer coatings (Table 13) were higher than those of the multilayer coatings (0.1119, 0.3883 GPa, 0.0885 ± 0.0132 and 0.2598 ± 0.0829 GPa, respectively). For the TiAlCrN, these values (except the achievable maximum H/E) were higher for the multilayer coatings.

8.2. *TiAlSiN coatings*

8.2.1. *Monolayer coatings*

- Several mechanisms have been proposed to account for the pronounced increase in hardness, H/E and H^3/E^2 brought about by Si addition in TiAlSiN coatings: the formation of nanocrystalline Ti(AlSi)N or (TiAl)N embedded in the Si_3N_4 amorphous phases with a reduction in grain size, solid solution hardening, strengthening of the grain boundary by the cohesive energy of the amorphous and crystalline interphase boundaries, and the restriction of dislocation motion by the amorphous Si_3N_4 phase. Improvement in these mechanical properties often results in higher wear resistance. The evolving microstructure,

grain size and hardness of TiAlSiN were also governed by the Al/Ti ratio and the concentration of Al and N.
- During annealing, Si delayed the formation of w-AlN and h-AlN, which were responsible for reducing coating hardness.
- Si increased the oxidation resistance by suppressing the formation of porous r-TiO_2, as well as promoting dense Al_2O_3 and SiO_2 on the surface, amorphous Si_3N_4 boundary phase, and dense nanocrystal structure.
- TiAlSiN coatings demonstrated a high tendency to form SiO_2, $Si(OH)_2$, Al_2O_3 and SiO_2 tribo-layers, leading to wear reduction.
- Increases in bias voltage could change coating microstructure from coarse columnar to fine-grained, reduce grain size, and increase hardness without significantly altering the chemical composition of the coatings.
- The adhesion property of TiAlSiN coatings could be improved by means of gradually reducing the Si content towards the substrate.

8.2.2. *Multilayer coatings*

- The TiAlSiN multilayer coatings investigated in the past consisted of alternate TiAlSiN and other coating layers (i.e. TiAlN, CrAlN, CrN, TiN, Ti, and TiAlTaN), alternate layers of TiAlSiN deposited using different bias voltage and Si content, and alternate (Ti,Si)N/(Ti,Al)N and alternate Ti-rich/AlSi-rich nano-layers.
- TiAlSiN multilayer coatings of different architectures showed clear superiority in oxidation resistance, mechanical properties, and adhesion strength. The Λ, bias voltage, arc current, number of coating layers, and thickness of the individual layers could be optimised to further enhance these properties.

8.3. *TiAlCrN coatings*

8.3.1. *Monolayer coatings*

- Increases in the hardness, H/E and H^3/E^2 of TiAlCrN brought about by Cr were due to solute solution hardening. The increased hardness was not pronounced, as was evident when compared to the results achieved by Si in the TiAlSiN coatings.
- Increasing the Ti/(Cr + Al) atomic ratio resulted in a higher degree of solid-solution hardening. However, increasing the Ti content reduced oxidation resistance by increasing the amount of TiO_2.
- The high-temperature stability of the coating hardness during annealing was due to the delayed formation of w-AlN brought about by Cr.
- A change in the applied substrate bias voltage was found to significantly affect the chemical composition, microstructure, hardness, adhesion strength, and thermal shock resistance of the coatings.
- The superior oxidation of TiAlCrN was due to the formation of dense Cr_2O_3 and Al_2O_3, and also the suppressed transformation of a-TiO_2 into r-TiO_2. Cr_2O_3 and Al_2O_3 tribo-layers were effective in suppressing wear.

8.3.2. *Multilayer coatings*

- The TiAlCrN multilayer coatings comprised of alternate TiAlSiN and other coating layers (i.e. TiAlN, NbN, CrN, WN and TiAlCrSiYN), and alternate layers of TiAlN/CrN and Ti(Al)N/Cr(Al)N).
- Advantages of the multilayer architecture coatings include: improved hardness, the formation of additional Nb–O and W–O tribo-films (for TiAlCrN/NbN and TiAlCrN/WN) acting together with Al_2O_3 and Cr_2O_3 to inhibit wear, increased Al content (for TiAlCrSiYN/TiAlCrN), leading to enhancement of their oxidation and cracking resistance, and energy dissipation capacity with a high tendency to form protective sapphire and mullite tribo-films.
- The Λ (for TiAlN/TiAlCrN) and applied substrate bias (for TiAlN/CrN) could be optimised to improve adhesion strength and mechanical properties.

8.4. *TiAlVN coatings*

8.4.1. *Monolayer coatings*

- An increase in the hardness of TiAlVN coatings brought about by V content was due to solid solution hardening and the suppressed transformation of fcc to hcp structure.
- High thermal stability exhibited during annealing was due to the retardation of w-AlN formation by V.
- The evolving microstructure, either having a single-phase fcc or dual-phase fcc + hcp structure, was highly dependent on Al content and bias voltage.
- Increasing the Ar:N_2 gas ratio led to the formation of densified and fine-grained structures, resulting in high hardness.
- Lubricious V_2O_5 formed at elevated temperatures acted as a liquid lubricant above its melting point.
- V promoted the transformation of a-TiO_2 to r-TiO_2 and less dense Al_2O_3, leading to inferior oxidation resistance.

8.4.2. *Multilayer coatings*

- The TiAVN multilayer coatings were comprised of alternate layers of TiAlN/VN.
- The onset temperature for rapid oxidation was governed by the (Ti + Al)/V ratio.
- The oxidation resistance of TiAlN/VN was governed by its VN layers, with VN being the first component to be oxidized.
- Reduced wear resulted from the formation of a hydroxide tribo-layer and V_2O_5 at low and high temperatures, respectively.

8.5. *TiAlTaN coatings*

8.5.1. *Monolayer coatings*

- The increased hardness of TiAlTaN brought about by Ta was due to solid solution hardening, increased compressive stress and cohesive strength, as well as a reduction in the grain size.

- The high thermal stability of the coatings was due to the suppressed formation of w-AlN by Ta.
- The formation of hexagonal-based phases such as Ta_5N_6 resulting from high Ta content improved the coating's toughness.
- Ta improved oxidation resistance by promoting the formation of dense Ti, Al and Ta oxide layers and the direct formation of stable r-TiO_2.
- Increasing the bias voltage favoured the growth of the fcc phase over the less dense hcp phase, leading to improved oxidation resistance.

8.5.2. *Multilayer coatings*

- The TiAlTaN multilayer coatings comprised of alternate layers of TiAlTaN/Ta, and TiAlTaN on top of the TiAlN/TaN multilayer layers.
- A change in the Λ of the TiAlTaN/Ta altered the columnar crystal size, hardness, and compressive stress.
- The hardness, compressive stress, adhesion strength, and wear resistance were greatly dependent on the volume fractions of TiAlTaN and TiAlN/TaN.

8.6. *TiAlBN coatings*

8.6.1. *Monolayer coatings*

- B increased the hardness of TiAlBN coatings via the formation of TiB_2 and nanocrystalline (Ti,Al)N grains separated by a-BN phase.
- Decreasing the (Ti,Al)N/BN and Ti/B phase ratios led to a reduction in the (Ti,Al)N grain size. However, a reduction in the Ti/B ratio, as well as an increase in nitrogen, was found to increase the amount of the softer a-BN phase.
- a-BN phase was able to enhance wear resistance and toughness by permitting some degree of (Ti,Al)N grain displacement under load.
- Al promoted the formation of soft h-BN over hard c-BN. A further reduction in COF occurred when the two phases reacted with water to produce boric acid and H_3BO_3. However, the formation of h-BN was found to reduce tool life.

8.7. *TiAlCrSiN coatings*

8.7.1. *Monolayer coatings*

- Increases in the hardness, H/E and H^3/E^2 of TiAlCrSiN coatings brought about by Cr and Si were due to the formation of nanocrystalline TiAlCrN grains in the amorphous a-Si_3N_4 matrix, strong cohesive strength between the nano-grains and matrix, a reduction in grain size, and solid solution hardening.
- Increasing the Si content changed the structure from columnar to dense and restricted grain growth by the formation of a-SiN_x phase and nanocrystalline TiSi grains.
- Coatings with more Al_2O_3 and Cr_2O_3 exhibited lower wear and COF.
- Increasing Al and Si content led to the transformation of cubic structure to a mixture of cubic + hexagonal and ultimately to a completely wurtzite-type structure.
- Si increased thermal stability at high temperatures by suppressing the formation of hcp-AlN, and thereby retaining the NaCl structure.

Funding

This work was supported by the Ministry of Higher Education, Malaysia (Fundamental Research Grant Scheme FRGS/1/2020/TK0/UMS/02/7) and Universiti Malaysia Sabah (UMSGreat Grant GUG0393-2/2019).

Declaration of Competing Interest

The authors declare that they have no known competing financial interests or personal relationships that could have appeared to influence the work reported in this paper.

REFERENCES

[1] Sidky PS, Hocking MG. Review of inorganic coatings and coating processes for reducing wear and corrosion. Br Corrosion J 1999;34:171–83. https://doi.org/10.1179/000705999101500815.
[2] Vancoille E, Celis JP, Roos JR. Dry sliding wear of TiN based ternary PVD coatings. Wear 1993;165:41–9. https://doi.org/10.1016/0043-1648(93)90370-2.
[3] Huang ZP, Sun Y, Bell T. Friction behaviour of TiN, CrN and (TiAl)N coatings. Wear 1994;173:13–20. https://doi.org/10.1016/0043-1648(94)90252-6.
[4] Rodríguez RJ, García JA, Medrano A, Rico M, Sánchez R, Martínez R, et al. Tribological behaviour of hard coatings deposited by arc-evaporation PVD. Vacuum 2002;67:559–66. https://doi.org/10.1016/S0042-207X(02)00248-8.
[5] Wittmer M, Noser J, Melchior H. Oxidation kinetics of TiN thin films. J Appl Phys 1981;52:6659–64. https://doi.org/10.1063/1.328659.
[6] Milošev I, Strehblow HH, Navinšek B. XPS in the study of high-temperature oxidation of CrN and TiN hard coatings. Surf Coating Technol 1995;74–75:897–902. https://doi.org/10.1016/0257-8972(95)08360-X.
[7] Fateh N, Fontalvo GA, Gassner G, Mitterer C. Influence of high-temperature oxide formation on the tribological behaviour of TiN and VN coatings. Wear 2007;2:1152–8. https://doi.org/10.1016/j.wear.2006.11.006.
[8] PalDey S, Deevi SC. Single layer and multilayer wear resistant coatings of (Ti,Al)N: a review. Mater Sci Eng, A 2003;342:58–79. https://doi.org/10.1016/S0921-5093(02)00259-9.
[9] Elmkhah H, Zhang TF, Abdollah-zadeh A, Kim KH, Mahboubi F. Surface characteristics for the Ti-Al-N coatings deposited by high power impulse magnetron sputtering technique at the different bias voltages. J Alloys Compd 2016;688:820–7. https://doi.org/10.1016/j.jallcom.2016.07.013.
[10] Komarov FF, Konstantinov VM, Kovalchuk AV, Konstantinov SV, Tkachenko HA. The effect of steel substrate pre-hardening on structural, mechanical, and tribological properties of magnetron sputtered TiN and

TiAlN coatings. Wear 2016;352–353:92–101. https://doi.org/10.1016/j.wear.2016.02.007.
[11] Lee S, Ryoo H, Lee J. Ti1−xAlx)N coatings by plasma-enhanced chemical vapor deposition. J Vac Sci Technol A Vacuum, Surfaces, Film 1994;12:1602–7. https://doi.org/10.1116/1.579362.
[12] Kimura A, Hasegawa H, Yamada K, Suzuki T. Effects of Al content on hardness, lattice parameter and microstructure of Ti1-xAlxN films. Surf Coating Technol 1999;120–121:438–41. https://doi.org/10.1016/S0257-8972(99)00491-0.
[13] Panjan P, Navinšek B, Čekada M, Zalar A. Oxidation behaviour of TiAlN coatings sputtered at low temperature. Vacuum 1999;53:127–31. https://doi.org/10.1016/S0042-207X(98)00407-2.
[14] Ohnuma H, Nihira N, Mitsuo A, Toyoda K, Kubota K, Aizawa T. Effect of aluminum concentration on friction and wear properties of titanium aluminum nitride films. Surf Coating Technol 2004;177–178:623–6. https://doi.org/10.1016/S0257-8972(03)00936-8.
[15] Höling A, Hultman L, Odén M, Sjölén J, Karlsson L. Mechanical properties and machining performance of Ti1-xAlxN-coated cutting tools. Surf Coating Technol 2005;191:384–92. https://doi.org/10.1016/j.surfcoat.2004.04.056.
[16] Wüstefeld C, Rafaja D, Klemm V, Michotte C, Kathrein M. Effect of the aluminium content and the bias voltage on the microstructure formation in Ti1-xAlxN protective coatings grown by cathodic arc evaporation. Surf Coating Technol 2010;205:1345–9. https://doi.org/10.1016/j.surfcoat.2010.07.057.
[17] Chen L, Paulitsch J, Du Y, Mayrhofer PH. Thermal stability and oxidation resistance of Ti–Al–N coatings. Surf Coating Technol 2012;206:2954–60. https://doi.org/10.1016/j.surfcoat.2011.12.028.
[18] Chang CL, Yang FC. Reprint of "Effect of target composition on the microstructural, mechanical, and corrosion properties of TiAlN thin films deposited by high-power impulse magnetron sputtering. Surf Coating Technol 2019;376:113–20. https://doi.org/10.1016/j.surfcoat.2019.07.008.
[19] Patel SB, Mohammadpour E, Mondinos N, Zhao X, Veder JP, feng Zhou Z, et al. High temperature in-situ phase stability of sputtered TiAlxN coatings. J Alloys Compd 2019;786:507–14. https://doi.org/10.1016/j.jallcom.2019.01.379.
[20] Kim CW, Kim KH. Anti-oxidation properties of TiAlN film prepared by plasma-assisted chemical vapor deposition and roles of Al. Thin Solid Films 1997;307:113–9.
[21] Münz W. Titanium aluminum nitride films: a new alternative to TiN coatings. J Vac Sci Technol A Vacuum, Surfaces, Film 1986;4:2717–25. https://doi.org/10.1116/1.573713.
[22] Vaz F, Rebouta L, Andritschky M, da Silva MF, Soares JC. Thermal oxidation of Ti1−xAlxN coatings in air. J Eur Ceram Soc 1997;17:1971–7. https://doi.org/10.1016/S0955-2219(97)00050-2.
[23] Qi ZB, Sun P, Zhu FP, Wu ZT, Liu B, Wang ZC, et al. Relationship between tribological properties and oxidation behavior of Ti0.34Al0.66N coatings at elevated temperature up to 900°C. Surf Coating Technol 2013;231:267–72. https://doi.org/10.1016/j.surfcoat.2012.02.017.
[24] Wang D, Li Y, Chang C, Ho W. Deposition of high quality (Ti,Al)N hard coatings by vacuum arc evaporation process. Surf Coating Technol 1999;114:109–13.
[25] Deng J, Liu A. Dry sliding wear behavior of PVD TiN, Ti55Al45N, and Ti35Al65N coatings at temperatures up to 600°C. Int J Refract Met Hard Mater 2013;41:241–9. https://doi.org/10.1016/j.ijrmhm.2013.04.008.
[26] Liu AH, Deng JX. Elevated temperature tribological properties of AlTiN coating up to 700°C. Surf Eng 2015;31:17–23. https://doi.org/10.1179/1743294414Y.0000000352.
[27] Barshilia HC, Yogesh K, Rajam KS. Deposition of TiAlN coatings using reactive bipolar-pulsed direct current unbalanced magnetron sputtering. Vacuum 2009;83:427–34. https://doi.org/10.1016/j.vacuum.2008.04.075.
[28] Vaz F, Rebouta L, Andritschky M, da Silva M, Soares J. The effect of the addition of Al and Si on the physical and mechanical properties of titanium nitride. J Mater Process Technol 1999;92–93:169–76. https://doi.org/10.1016/S0924-0136(99)00159-4.
[29] Li YS, Shimada S, Kiyono H, Hirose A. Synthesis of Ti–Al–Si–N nanocomposite films using liquid injection PECVD from alkoxide precursors. Acta Mater 2006;54:2041–8. https://doi.org/10.1016/j.actamat.2005.12.034.
[30] Miyamura A, Yamaguchi M, Hattori K, Sato Y, Nakamura S, Shigesato Y. Ti–Al–Si–N films for superhard coatings deposited by reactive cosputtering using Ti, Al, and Si targets. J Vac Sci Technol A Vacuum, Surfaces, Film 2007;25:1103–7. https://doi.org/10.1116/1.2721577.
[31] Kong D, Fu G. Nanoindentation analysis of TiN, TiAlN, and TiAlSiN coatings prepared by cathode ion plating. Sci China Technol Sci 2015;58:1360–8. https://doi.org/10.1007/s11431-015-5876-2.
[32] Chen H, Zheng BCC, Li YGG, Wu ZLL, Lei MKK. Flexible hard TiAlSiN nanocomposite coatings deposited by modulated pulsed power magnetron sputtering with controllable peak power. Thin Solid Films 2019;669:377–86. https://doi.org/10.1016/j.tsf.2018.10.031.
[33] Vennemann A, Stock H-R, Kohlscheen J, Rambadt S, Erkens G. Oxidation resistance of titanium-aluminium-silicon nitride coatings. Surf Coating Technol 2003;174–175:408–15. https://doi.org/10.1016/S0257-8972.
[34] Yang S-M, Chang Y-Y, Lin D-Y, Wang D-Y, Wu W. Thermal stability of TiAlN and nanocomposite TiAlSiN thin films. J Nanosci Nanotechnol 2009;9:1108–12. https://doi.org/10.1166/jnn.2009.C098.
[35] Chang Y-Y, Yang S-M. High temperature oxidation behavior of multicomponent TiAlSiN coatings. Thin Solid Films 2010;518:S34–7. https://doi.org/10.1016/j.tsf.2010.03.020.
[36] Wainstein D, Kovalev A. Tribooxidation as a way to improve the wear resistance of cutting tools. Coatings 2018;8:223. https://doi.org/10.3390/coatings8060223.
[37] Gui B, Zhou H, Zheng J, Liu X, Feng X, Zhang Y, et al. Microstructure and properties of TiAlCrN ceramic coatings deposited by hybrid HiPIMS/DC magnetron co-sputtering. Ceram Int 2021;47:8175–83. https://doi.org/10.1016/j.ceramint.2020.11.175.
[38] Tillmann W, Momeni S, Hoffmann F. A study of mechanical and tribological properties of self-lubricating TiAlVN coatings at elevated temperatures. Tribol Int 2013;66:324–9. https://doi.org/10.1016/j.triboint.2013.06.007.
[39] Rachbauer R, Holec D, Mayrhofer PH. Increased thermal stability of Ti–Al–N thin films by Ta alloying. Surf Coating Technol 2012;211:98–103. https://doi.org/10.1016/j.surfcoat.2011.07.009.
[40] Hollerweger R, Riedl H, Paulitsch J, Arndt M, Rachbauer R, Polcik P, et al. Origin of high temperature oxidation resistance of Ti–Al–Ta–N coatings. Surf Coating Technol 2014;257:78–86. https://doi.org/10.1016/j.surfcoat.2014.02.067.

[41] Baker MA, Klose S, Rebholz C, Leyland A, Matthews A. Evaluating the microstructure and performance of nanocomposite PVD TiAlBN coatings. Surf Coating Technol 2002;151–152:338–43.
[42] Chen M, Cai F, Chen W, Wang Q, Zhang S. Influence of vacuum annealing on structures and properties of Al Ti Si N coatings with corrosion resistance. Surf Coating Technol 2017;312:25–31. https://doi.org/10.1016/j.surfcoat.2016.08.006.
[43] Kim SK, Van Le V. Cathodic arc plasma deposited TiAlSiN thin films using an Al-15 at.% Si cathode. Thin Solid Films 2010;518:7483–6. https://doi.org/10.1016/j.tsf.2010.05.029.
[44] Miletić A, Panjan P, Škorić B, Čekada M, Dražič G, Kovač J. Microstructure and mechanical properties of nanostructured Ti-Al-Si-N coatings deposited by magnetron sputtering. Surf Coating Technol 2014;241:105–11. https://doi.org/10.1016/j.surfcoat.2013.10.050.
[45] Zhao F, Ge Y, Wang L, Wang X. Tribological and mechanical properties of hardness-modulated TiAlSiN multilayer coatings fabricated by plasma immersion ion implantation and deposition. Surf Coating Technol 2020;402:126475. https://doi.org/10.1016/j.surfcoat.2020.126475.
[46] Li G, Sun J, Xu Y, Xu Y, Gu J, Wang L, et al. Microstructure, mechanical properties, and cutting performance of TiAlSiN multilayer coatings prepared by HiPIMS. Surf Coating Technol 2018;353:274–81. https://doi.org/10.1016/j.surfcoat.2018.06.017.
[47] Yu D, Wang C, Cheng X, Zhang F. Microstructure and properties of TiAlSiN coatings prepared by hybrid PVD technology. Thin Solid Films 2009;517:4950–5. https://doi.org/10.1016/j.tsf.2009.03.091.
[48] Carvalho S, Rebouta L, Cavaleiro A, Rocha L, Gomes J, Alves E. Microstructure and mechanical properties of nanocomposite (Ti,Si,Al)N coatings. Thin Solid Films 2001;398–399:391–6. https://doi.org/10.1016/S0040-6090(01)01348-7.
[49] Tillmann W, Dildrop M. Influence of Si content on mechanical and tribological properties of TiAlSiN PVD coatings at elevated temperatures. Surf Coating Technol 2017;321:448–54. https://doi.org/10.1016/j.surfcoat.2017.05.014.
[50] Park I-W, Choi SR, Suh JH, Park C-G, Kim KH. Deposition and mechanical evaluation of superhard Ti–Al–Si–N nanocomposite films by a hybrid coating system. Thin Solid Films 2004;447–448:443–8. https://doi.org/10.1016/S0040-6090(03)01122-2.
[51] Zou CW, Zhang J, Xie W, Shao LX, Guo LP, Fu DJ. Characterization and properties Ti–Al–Si–N nanocomposite coatings prepared by middle frequency magnetron sputtering. Appl Surf Sci 2011;257:10373–8. https://doi.org/10.1016/j.apsusc.2011.06.086.
[52] Sui X, Li G, Qin X, Yu H, Zhou X, Wang K, et al. Relationship of microstructure, mechanical properties and titanium cutting performance of TiAlN/TiAlSiN composite coated tool. Ceram Int 2016;42:7524–32. https://doi.org/10.1016/j.ceramint.2016.01.159.
[53] Rahman MM, Jiang Z-T, Zhou Z, Xie Z, Yin CY, Kabir H, et al. Effects of annealing temperatures on the morphological, mechanical, surface chemical bonding, and solar selectivity properties of sputtered TiAlSiN thin films. J Alloys Compd 2016;671:254–66. https://doi.org/10.1016/j.jallcom.2016.02.077.
[54] Kim JS, Kim GJ, Chang Kang M, Kim JW, Kim KH. Cutting performance of Ti-Al-Si-N-coated tool by a hybrid-coating system for high-hardened materials. Surf Coating Technol 2005;193:249–54. https://doi.org/10.1016/j.surfcoat.2004.07.019.
[55] Chang C-L, Lee J-W, Tseng M-D. Microstructure, corrosion and tribological behaviors of TiAlSiN coatings deposited by cathodic arc plasma deposition. Thin Solid Films 2009;517:5231–6. https://doi.org/10.1016/j.tsf.2009.03.082.
[56] Zhao F, Wang L, Wang X. Microstructure and properties of TiAlSiN ultra-hard coatings prepared by plasma immersion ion implantation and deposition with TiAlSi alloy cathodes. Vacuum 2020;174:109194. https://doi.org/10.1016/j.vacuum.2020.109194.
[57] He N, Li H, Ji L, Liu X, Zhou H, Chen J. High temperature tribological properties of TiAlSiN coatings produced by hybrid PVD technology. Tribol Int 2016;98:133–43. https://doi.org/10.1016/j.triboint.2016.02.034.
[58] Kim GS, Kim BS, Lee SY, Hahn JH. Effect of Si content on the properties of TiAl–Si–N films deposited by closed field unbalanced magnetron sputtering with vertical magnetron sources. Thin Solid Films 2006;506–507:128–32. https://doi.org/10.1016/j.tsf.2005.08.136.
[59] Jiang N, Shen YG, Zhang HJ, Bao SN, Hou XY. Superhard nanocomposite Ti–Al–Si–N films deposited by reactive unbalanced magnetron sputtering. Mater Sci Eng B 2006;135:1–9. https://doi.org/10.1016/j.mseb.2006.06.043.
[60] Wu J, He N, Li H, Liu X, Ji L, Huang X, et al. Deposition and characterization of TiAlSiN coatings prepared by hybrid PVD coating system. Surf Interface Anal 2015;47:184–91. https://doi.org/10.1002/sia.5680.
[61] Fuentes GG, Almandoz E, Pierrugues R, Martínez R, Rodríguez RJ, Caro J, et al. High temperature tribological characterisation of TiAlSiN coatings produced by cathodic arc evaporation. Surf Coating Technol 2010;205:1368–73. https://doi.org/10.1016/j.surfcoat.2010.09.004.
[62] Xie Z, Wang L, Wang X, Huang L, Lu Y, Yan J. Influence of Si content on structure and mechanical properties of TiAlSiN coatings deposited by multi-plasma immersion ion implantation and deposition. Trans Nonferrous Met Soc China 2011;21:s476–82. https://doi.org/10.1016/S1003-6326(11)61628-2.
[63] Flink A, Andersson JM, Alling B, Daniel R, Sjölén J, Karlsson L, et al. Structure and thermal stability of arc evaporated (Ti0.33Al0.67)1−xSixN thin films. Thin Solid Films 2008;517:714–21. https://doi.org/10.1016/j.tsf.2008.08.126.
[64] Martin PJ, Bendavid A, Cairney JM, Hoffman M. Nanocomposite Ti–Si–N, Zr–Si–N, Ti–Al–Si–N, Ti–Al–V–Si–N thin film coatings deposited by vacuum arc deposition. Surf Coating Technol 2005;200:2228–35. https://doi.org/10.1016/j.surfcoat.2004.06.012.
[65] Chen L, Du Y, Wang AJ, Wang SQ, Zhou SZ. Effect of Al content on microstructure and mechanical properties of Ti–Al–Si–N nanocomposite coatings. Int J Refract Met Hard Mater 2009;27:718–21. https://doi.org/10.1016/j.ijrmhm.2008.12.002.
[66] Cao F, Munroe P, Zhou Z, Xie Z. Mechanically robust TiAlSiN coatings prepared by pulsed-DC magnetron sputtering system: scratch response and tribological performance. Thin Solid Films 2018;645:222–30. https://doi.org/10.1016/j.tsf.2017.10.058.
[67] Chen H, Zheng BC, Ou YX, Lei MK. Microstructure and thermal conductivity of Ti-Al-Si-N nanocomposite coatings deposited by modulated pulsed power magnetron sputtering. Thin Solid Films 2020;693:137680. https://doi.org/10.1016/j.tsf.2019.137680.
[68] Ma Q, Li L, Xu Y, Gu J, Wang L, Xu Y. Effect of bias voltage on TiAlSiN nanocomposite coatings deposited by HiPIMS. Appl Surf Sci 2017;392:826–33. https://doi.org/10.1016/j.apsusc.2016.09.028.
[69] Tillmann W, Dildrop M. Influence of bias voltage and sputter mode on the coating properties of TiAlSiN. Mater

Werkst 2017;48:855–61. https://doi.org/10.1002/mawe.201600731.
[70] Chang Y-Y, Lai H-M. Wear behavior and cutting performance of CrAlSiN and TiAlSiN hard coatings on cemented carbide cutting tools for Ti alloys. Surf Coating Technol 2014;259:152–8. https://doi.org/10.1016/j.surfcoat.2014.02.015.
[71] Pei F, Liu HJ, Chen L, Xu YX, Du Y. Improved properties of TiAlN coating by combined Si-addition and multilayer architecture. J Alloys Compd 2019;790:909–16. https://doi.org/10.1016/j.jallcom.2019.03.248.
[72] Xie ZW, Wang LP, Wang XF, Huang L, Lu Y, Yan JC. Influence of oxidation on the structural and mechanical properties of TiAlSiN coatings synthesized by multi-plasma immersion ion implantation and deposition. Nucl Instrum Methods Phys Res Sect B Beam Interact Mater Atoms 2012;271:1–5. https://doi.org/10.1016/j.nimb.2011.10.011.
[73] Chen L, Wang SQ, Du Y, Zhou SZ, Gang T, Fen JC, et al. Machining performance of Ti–Al–Si–N coated inserts. Surf Coating Technol 2010;205:582–6. https://doi.org/10.1016/j.surfcoat.2010.07.043.
[74] Chen T, Xie Z, Gong F, Luo Z, Yang Z. Correlation between microstructure evolution and high temperature properties of TiAlSiN hard coatings with different Si and Al content. Appl Surf Sci 2014;314:735–45. https://doi.org/10.1016/j.apsusc.2014.06.057.
[75] Hong D, Huang L, Yuan J, Li C. Influence of annealing temperature on microstructure evolution of TiAlSiN coating and its tribological behavior against Ti6Al4V alloys. Ceram Int 2021;47:3789–96. https://doi.org/10.1016/j.ceramint.2020.09.236.
[76] Barshilia HC, Ghosh M, Shashidhara Ramakrishna R, Rajam KS. Deposition and characterization of TiAlSiN nanocomposite coatings prepared by reactive pulsed direct current unbalanced magnetron sputtering. Appl Surf Sci 2010;256:6420–6. https://doi.org/10.1016/j.apsusc.2010.04.028.
[77] Chen L, Yang B, Xu Y, Pei F, Zhou L, Du Y. Improved thermal stability and oxidation resistance of Al–Ti–N coating by Si addition. Thin Solid Films 2014;556:369–75. https://doi.org/10.1016/j.tsf.2014.01.072.
[78] Pilloud D, Pierson JF, Marco de Lucas MC, Cavaleiro A. Study of the structural changes induced by air oxidation in Ti–Si–N hard coatings. Surf Coating Technol 2008;202:2413–7. https://doi.org/10.1016/j.surfcoat.2007.09.017.
[79] Zhu L, Hu M, Ni W, Liu Y. High temperature oxidation behavior of Ti0.5Al0.5N coating and Ti0.5Al0.4Si0.1N coating. Vacuum 2012;86:1795–9. https://doi.org/10.1016/j.vacuum.2012.04.013.
[80] Liu J, Zhu S-S, Deng X, Liu J-Y, Wang Z-P, Qu Z. Cutting performance and wear behavior of AlTiN- and TiAlSiN-coated carbide tools during dry milling of Ti–6Al–4V. Acta Metall Sin English Lett 2020;33:459–70. https://doi.org/10.1007/s40195-020-01010-6.
[81] Philippon D, Godinho V, Nagy PM, Delplancke-Ogletree MP, Fernández A. Endurance of TiAlSiN coatings: effect of Si and bias on wear and adhesion. Wear 2011;270:541–9. https://doi.org/10.1016/j.wear.2011.01.009.
[82] hui Zhu L, Song C, yang Ni W, xiong Liu Y. Effect of 10% Si addition on cathodic arc evaporated TiAlSiN coatings. Trans Nonferrous Met Soc China English 2016;26:1638–46. https://doi.org/10.1016/S1003-6326(16)64273-5.
[83] Ma H, Miao Q, Zhang G, Liang W, Wang Y, Sun Z, et al. The influence of multilayer structure on mechanical behavior of TiN/TiAlSiN multilayer coating. Ceram Int 2021;47:12583–91. https://doi.org/10.1016/j.ceramint.2021.01.117.
[84] Lü W, Li G, Zhou Y, Liu S, Wang K, Wang Q. Effect of high hardness and adhesion of gradient TiAlSiN coating on cutting performance of titanium alloy. J Alloys Compd 2020;820:153137. https://doi.org/10.1016/j.jallcom.2019.153137.
[85] Hsu T-W, Greczynski G, Boyd R, Kolozsvári S, Polcik P, Bolz S, et al. Influence of Si content on phase stability and mechanical properties of TiAlSiN films grown by AlSi-HiPIMS/Ti-DCMS co-sputtering. Surf Coating Technol 2021:127661. https://doi.org/10.1016/j.surfcoat.2021.127661.
[86] Chang Y-Y, Cai M-C. Mechanical property and tribological performance of AlTiSiN and AlTiBN hard coatings using ternary alloy targets. Surf Coating Technol 2019;374:1120–7. https://doi.org/10.1016/j.surfcoat.2018.01.077.
[87] Wu ZL, Li YG, Wu B, Lei MK. Effect of microstructure on mechanical and tribological properties of TiAlSiN nanocomposite coatings deposited by modulated pulsed power magnetron sputtering. Thin Solid Films 2015;597:197–205. https://doi.org/10.1016/j.tsf.2015.11.047.
[88] Xiao B, Liu J, Liu F, Zhong X, Xiao X, Zhang TF, et al. Effects of microstructure evolution on the oxidation behavior and high-temperature tribological properties of AlCrN/TiAlSiN multilayer coatings. Ceram Int 2018;44:23150–61. https://doi.org/10.1016/j.ceramint.2018.09.125.
[89] Fukumoto N, Ezura H, Suzuki T. Synthesis and oxidation resistance of TiAlSiN and multilayer TiAlSiN/CrAlN coating. Surf Coating Technol 2009;204:902–6. https://doi.org/10.1016/j.surfcoat.2009.04.027.
[90] Parlinska-Wojtan M. Oxygen diffusion in columnar TiAlSiN coatings investigated by electron microscopy. Thin Solid Films 2016;616:437–43. https://doi.org/10.1016/j.tsf.2016.08.050.
[91] Liu H, Yang F-C, Tsai Y-J, Wang X, Li W, Chang C-L. Effect of modulation structure on the microstructural and mechanical properties of TiAlSiN/CrN thin films prepared by high power impulse magnetron sputtering. Surf Coating Technol 2019;358:577–85. https://doi.org/10.1016/j.surfcoat.2018.11.069.
[92] Liu Y, Liu HD, Pelenovich V, Wan Q, Guo JL, Chen YM, et al. Influences of modulation period on structure and properties of AlTiSiN/AlCrSiN nanocomposite multilayer coatings. Vacuum 2021;193:110516. https://doi.org/10.1016/j.vacuum.2021.110516.
[93] Carvalho S, Ribeiro E, Rebouta L, Tavares C, Mendonça J, Caetano Monteiro A, et al. Microstructure, mechanical properties and cutting performance of superhard (Ti,Si,Al)N nanocomposite films grown by d.c. reactive magnetron sputtering. Surf Coating Technol 2004;177–178:459–68. https://doi.org/10.1016/j.surfcoat.2003.08.056.
[94] Chen W, Lin Y, Zheng J, Zhang S, Liu S, Kwon SC. Preparation and characterization of CrAlN/TiAlSiN nano-multilayers by cathodic vacuum arc. Surf Coating Technol 2015;265:205–11. https://doi.org/10.1016/j.surfcoat.2015.01.023.
[95] Zhang J, Chen L, Kong Y, Hu C, Liu Z, Du Y, et al. Microstructure, mechanical and thermal properties of TiAlTaN/TiAlSiN multilayer. Vacuum 2021;187:110138. https://doi.org/10.1016/j.vacuum.2021.110138.
[96] Chang Y-Y, Yang S-J, Wu W, Kuo Y-C, Lee J-W, Wang C-J. Mechanical properties of gradient and multilayered TiAlSiN hard coatings. Thin Solid Films 2009;517:4934–7. https://doi.org/10.1016/j.tsf.2009.03.036.
[97] Li G, Li L, Han M, Luo S, Jin J, Wang L, et al. The performance of TiAlSiN coated cemented carbide tools enhanced by inserting Ti interlayers. Metals (Basel) 2019;9:918. https://doi.org/10.3390/met9090918.
[98] Cai F, Wang J, Zhou Q, Zhang S, Zheng J, Wang Q, et al. Reduced delamination and improved cutting performance

of TiAlSiN multilayer coated cutter by tailoring the adhesion layers and intermediate layers. Wear 2022;488–489:204135. https://doi.org/10.1016/j.wear.2021.204135.
[99] Zhou H, Zheng J, Gui B, Geng D, Wang Q. AlTiCrN coatings deposited by hybrid HIPIMS/DC magnetron co-sputtering. Vacuum 2017;136:129–36. https://doi.org/10.1016/j.vacuum.2016.11.021.
[100] Xu YX, Chen L, Yang B, Peng YB, Du Y, Feng JC, et al. Effect of CrN addition on the structure, mechanical and thermal properties of Ti-Al-N coating. Surf Coating Technol 2013;235:506–12. https://doi.org/10.1016/j.surfcoat.2013.08.010.
[101] Sui X, Li G, Zhou H, Zhang S, Yu Y, Wang Q, et al. Evolution behavior of oxide scales of TiAlCrN coatings at high temperature. Surf Coating Technol 2019;360:133–9. https://doi.org/10.1016/j.surfcoat.2019.01.016.
[102] Forsén R, Johansson M, Odén M, Ghafoor N. Decomposition and phase transformation in TiCrAlN thin coatings. J Vac Sci Technol A Vacuum, Surfaces, Film 2012;30:061506. https://doi.org/10.1116/1.4757953.
[103] Beake BD, Isern L, Endrino JL, Fox-Rabinovich GS. Micro-impact testing of AlTiN and TiAlCrN coatings. Wear 2019;418–419:102–10. https://doi.org/10.1016/j.wear.2018.11.010.
[104] Yamamoto T, Hasegawa H, Suzuki T, Yamamoto K. Effects of thermal annealing on phase transformation and microhardness of (TixCryAlz)N films. Surf Coating Technol 2005;200:321–5. https://doi.org/10.1016/j.surfcoat.2005.02.048.
[105] Georgiadis A, Fuentes GG, Almandoz E, Medrano A, Palacio JF, Miguel A. Characterisation of cathodic arc evaporated CrTiAlN coatings: tribological response at room temperature and at 400 °C. Mater Chem Phys 2017;190:194–201. https://doi.org/10.1016/j.matchemphys.2017.01.021.
[106] Lin J, Zhang X, Ou Y, Wei R. The structure, oxidation resistance, mechanical and tribological properties of CrTiAlN coatings. Surf Coating Technol 2015;277:58–66. https://doi.org/10.1016/j.surfcoat.2015.07.013.
[107] Chen L, Chang KK, Du Y, Li JR, Wu MJ. A comparative research on magnetron sputtering and arc evaporation deposition of Ti-Al-N coatings. Thin Solid Films 2011;519:3762–7. https://doi.org/10.1016/j.tsf.2011.01.358.
[108] Lind H, Forsén R, Alling B, Ghafoor N, Tasndi F, Johansson MP, et al. Improving thermal stability of hard coating films via a concept of multicomponent alloying. Appl Phys Lett 2011;99:2011–4. https://doi.org/10.1063/1.3631672.
[109] Zhou ZF, Tam PL, Shum PW, Li KY. High temperature oxidation of CrTiAlN hard coatings prepared by unbalanced magnetron sputtering. Thin Solid Films 2009;517:5243–7. https://doi.org/10.1016/j.tsf.2009.03.115.
[110] Xu YX, Riedl H, Holec D, Chen L, Du Y, Mayrhofer PH. Thermal stability and oxidation resistance of sputtered Ti-Al-Cr-N hard coatings. Surf Coating Technol 2017;324:48–56. https://doi.org/10.1016/j.surfcoat.2017.05.053.
[111] Ru Q, Hu S, Huang N, Zhao L, Qiu X, Hu X. Properties of TiAlCrN coatings prepared by vacuum cathodic arc ion plating. Rare Met 2008;27:251–6. https://doi.org/10.1016/S1001-0521(08)60124-2.
[112] Yamamoto K, Sato T, Takahara K, Hanaguri K. Properties of (Ti,Cr,Al)N coatings with high Al content deposited by new plasma enhanced arc-cathode. Surf Coating Technol 2003;174–175:620–6. https://doi.org/10.1016/S0257-8972.
[113] Zhang J, Lv H, Cui G, Jing Z, Wang C. Effects of bias voltage on the microstructure and mechanical properties of (Ti,Al,Cr)N hard films with N-gradient distributions. Thin Solid Films 2011;519:4818–23. https://doi.org/10.1016/j.tsf.2011.01.036.
[114] Tu J, Duan H, Xu J, Li J. Tribological performance of TiAlSiN and TiAlCrN/TiAlN coating blades. Sci China Technol Sci 2014;57:345–50. https://doi.org/10.1007/s11431-013-5432-x.
[115] Warcholinski B, Gilewicz A, Myslinski P. Tribological properties of TiAlCrN thin films. Rev Adv Mater Sci 2009;22:81–8.
[116] Fox-Rabinovich GS, Yamomoto K, Veldhuis SC, Kovalev AI, Dosbaeva GK. Tribological adaptability of TiAlCrN PVD coatings under high performance dry machining conditions. Surf Coating Technol 2005;200:1804–13. https://doi.org/10.1016/j.surfcoat.2005.08.057.
[117] Luo Q, Rainforth WM, Donohue LA, Wadsworth I, Münz WD. Tribological investigation of TiAlCrN and TiAlN/CrN coatings grown by combined steered-arc/unbalanced magnetron deposition. Vacuum 1999;53:123–6. https://doi.org/10.1016/S0042-207X(98)00406-0.
[118] Fox-Rabinovich GS, Kovalev AI, Aguirre MH, Beake BD, Yamamoto K, Veldhuis SC, et al. Design and performance of AlTiN and TiAlCrN PVD coatings for machining of hard to cut materials. Surf Coating Technol 2009;204:489–96. https://doi.org/10.1016/j.surfcoat.2009.08.021.
[119] Harris SG, Doyle ED, Vlasveld AC, Audy J, Quick D. A study of the wear mechanisms of Ti1-xAlxN and Ti1-x-yAlxCryN coated high-speed steel twist drills under dry machining conditions. Wear 2003;254:723–34. https://doi.org/10.1016/S0043-1648(03)00258-8.
[120] Harris SG, Doyle ED, Vlasveld AC, Audy J, Long JM, Quick D. Influence of chromium content on the dry machining performance of cathodic arc evaporated TiAlN coatings. Wear 2003;254:185–94. https://doi.org/10.1016/S0043-1648(02)00290-9.
[121] Kovalev AI, Wainstein DL, Rashkovskiy AY, Fox-Rabinovich GS, Yamamoto K, Veldhuis S, et al. Impact of Al and Cr alloying in TiN-based PVD coatings on cutting performance during machining of hard to cut materials. Vacuum 2010;84:184–7. https://doi.org/10.1016/j.vacuum.2009.06.019.
[122] Shen L, Zhao J, Zhang Y-Q, Quan G-Z. Performance evaluation of titanium-based metal nitride coatings and die lifetime prediction in a cold extrusion process. High Temp Mater Process 2021;40:108–20. https://doi.org/10.1515/htmp-2021-0019.
[123] Chang YY, Yang YJ, Weng SY. Effect of interlayer design on the mechanical properties of AlTiCrN and multilayered AlTiCrN/TiSiN hard coatings. Surf Coating Technol 2020;389:125637. https://doi.org/10.1016/j.surfcoat.2020.125637.
[124] Huang W, Zalnezhad E, Musharavati F, Jahanshahi P. Investigation of the tribological and biomechanical properties of CrAlTiN and CrN/NbN coatings on SST 304. Ceram Int 2017;43:7992–8003. https://doi.org/10.1016/j.ceramint.2017.03.081.
[125] Forsén R, Johansson MP, Odén M, Ghafoor N. Effects of Ti alloying of AlCrN coatings on thermal stability and oxidation resistance. Thin Solid Films 2013;534:394–402. https://doi.org/10.1016/j.tsf.2013.03.003.
[126] Nakonechna O. Effect of Cr dopants on the structure and failure mechanism of TiAlN multilayered films. Metallofiz i Noveishie Tekhnologii 2019;41:621–31. https://doi.org/10.15407/mfint.41.05.0621.
[127] Santana AE, Karimi A, Derflinger VH, Schütze A. Microstructure and mechanical behavior of TiAlCrN multilayer thin films. Surf Coating Technol 2004;177–178:334–40. https://doi.org/10.1016/j.surfcoat.2003.09.023.

[128] Fox-Rabinovich GS, Yamamoto K, Kovalev AI, Veldhuis SC, Ning L, Shuster LS, et al. Wear behavior of adaptive nano-multilayered TiAlCrN/NbN coatings under dry high performance machining conditions. Surf Coating Technol 2008;202:2015–22. https://doi.org/10.1016/j.surfcoat.2007.08.067.
[129] Ning L, Veldhuis SC, Yamamoto K. Investigation of wear behavior and chip formation for cutting tools with nano-multilayered TiAlCrN/NbN PVD coating. Int J Mach Tool Manufact 2008;48:656–65. https://doi.org/10.1016/j.ijmachtools.2007.10.021.
[130] Fox-Rabinovich GS, Yamamoto K, Veldhuis SC, Kovalev AI, Shuster LS, Ning L. Self-adaptive wear behavior of nano-multilayered TiAlCrN/WN coatings under severe machining conditions. Surf Coating Technol 2006;201:1852–60. https://doi.org/10.1016/j.surfcoat.2006.03.010.
[131] Fox-Rabinovich GS, Beake BD, Yamamoto K, Aguirre MH, Veldhuis SC, Dosbaeva G, et al. Structure, properties and wear performance of nano-multilayered TiAlCrSiYN/TiAlCrN coatings during machining of Ni-based aerospace superalloys. Surf Coating Technol 2010;204:3698–706. https://doi.org/10.1016/j.surfcoat.2010.04.050.
[132] Fox-Rabinovich GS, Yamamoto K, Beake BD, Kovalev AI, Aguirre MH, Veldhuis SC, et al. Emergent behavior of nano-multilayered coatings during dry high-speed machining of hardened tool steels. Surf Coating Technol 2010;204:3425–35. https://doi.org/10.1016/j.surfcoat.2010.04.002.
[133] Chowdhury S, Beake BD, Yamamoto K, Bose B, Aguirre M, Fox-Rabinovich GS, et al. Improvement of wear performance of nano-multilayer PVD coatings under dry hard end milling conditions based on their architectural development. Coatings 2018;8:1–14. https://doi.org/10.3390/coatings8020059.
[134] Yuan J, Yamamoto K, Covelli D, Tauhiduzzaman M, Arif T, Gershman IS, et al. Tribo-films control in adaptive TiAlCrSiYN/TiAlCrN multilayer PVD coating by accelerating the initial machining conditions. Surf Coating Technol 2016;294:54–61. https://doi.org/10.1016/j.surfcoat.2016.02.041.
[135] Fox-Rabinovich G, Kovalev A, Aguirre MH, Yamamoto K, Veldhuis S, Gershman I, et al. Evolution of self-organization in nano-structured PVD coatings under extreme tribological conditions. Appl Surf Sci 2014;297:22–32. https://doi.org/10.1016/j.apsusc.2014.01.052.
[136] Fernandes F, Danek M, Polcar T, Cavaleiro A. Tribological and cutting performance of TiAlCrN films with different Cr contents deposited with multilayered structure. Tribol Int 2018;119:345–53. https://doi.org/10.1016/j.triboint.2017.11.008.
[137] Danek M, Fernandes F, Cavaleiro A, Polcar T. Influence of Cr additions on the structure and oxidation resistance of multilayered TiAlCrN films. Surf Coating Technol 2017;313:158–67. https://doi.org/10.1016/j.surfcoat.2017.01.053.
[138] Hsu CH, Chen KL, Lin ZH, Su CY, Lin CK. Bias effects on the tribological behavior of cathodic arc evaporated CrTiAlN coatings on AISI 304 stainless steel. Thin Solid Films 2010;518:3825–9. https://doi.org/10.1016/j.tsf.2010.02.012.
[139] Kutschej K, Mayrhofer PH, Kathrein M, Polcik P, Mitterer C. A new low-friction concept for Ti1−xAlxN based coatings in high-temperature applications. Surf Coating Technol 2004;188–189:358–63. https://doi.org/10.1016/j.surfcoat.2004.08.022.
[140] Pfeiler M, Kutschej K, Penoy M, Michotte C, Mitterer C, Kathrein M. The effect of increasing V content on structure, mechanical and tribological properties of arc evaporated Ti–Al–V–N coatings. Int J Refract Met Hard Mater 2009;27:502–6. https://doi.org/10.1016/j.ijrmhm.2008.06.008.
[141] Kutschej K, Mayrhofer PH, Kathrein M, Polcik P, Mitterer C. Influence of oxide phase formation on the tribological behaviour of Ti–Al–V–N coatings. Surf Coating Technol 2005;200:1731–7. https://doi.org/10.1016/j.surfcoat.2005.08.044.
[142] Lewis DB, Creasey S, Zhou Z, Forsyth JJ, Ehiasarian AP, Hovsepian PE, et al. The effect of (Ti+Al):V ratio on the structure and oxidation behaviour of TiAlN/VN nano-scale multilayer coatings. Surf Coating Technol 2004;177–178:252–9. https://doi.org/10.1016/j.surfcoat.2003.09.041.
[143] Xu YX, Chen L, Pei F, Yue JL, Du Y. Thermal stability and oxidation resistance of V-alloyed TiAlN coatings. Ceram Int 2018;44:1705–10. https://doi.org/10.1016/j.ceramint.2017.10.100.
[144] Phuong DD, Luong VD, Minh PN, Park HJ, Moon K Il. Microstructure, mechanical and tribological behavior of the TiAlVN coatings. Acta Metall Slovaca 2018;24:266–72. https://doi.org/10.12776/ams.v24i4.1187.
[145] Tillmann W, Sprute T, Hoffmann F, Chang Y-Y, Tsai C-Y. Influence of bias voltage on residual stresses and tribological properties of TiAlVN-coatings at elevated temperatures. Surf Coating Technol 2013;231:122–5. https://doi.org/10.1016/j.surfcoat.2012.03.012.
[146] Pfeiler M, Kutschej K, Penoy M, Michotte C, Mitterer C, Kathrein M. The influence of bias voltage on structure and mechanical/tribological properties of arc evaporated Ti–Al–V–N coatings. Surf Coating Technol 2007;202:1050–4. https://doi.org/10.1016/j.surfcoat.2007.07.045.
[147] Torres H, Rodríguez Ripoll M, Prakash B. Tribological behaviour of self-lubricating materials at high temperatures. Int Mater Rev 2018;63:309–40. https://doi.org/10.1080/09506608.2017.1410944.
[148] Franz R, Mitterer C. Vanadium containing self-adaptive low-friction hard coatings for high-temperature applications: a review. Surf Coating Technol 2013;228:1–13. https://doi.org/10.1016/j.surfcoat.2013.04.034.
[149] Fateh N, Fontalvo GA, Gassner G, Mitterer C. The beneficial effect of high-temperature oxidation on the tribological behaviour of V and VN coatings. Tribol Lett 2007;28:1–7. https://doi.org/10.1007/s11249-007-9241-x.
[150] Kutschej K, Mayrhofer PH, Kathrein M, Polcik P, Tessadri R, Mitterer C. Structure, mechanical and tribological properties of sputtered Ti1−xAlxN coatings with $0.5 \leq x \leq 0.75$. Surf Coating Technol 2005;200:2358–65. https://doi.org/10.1016/j.surfcoat.2004.12.008.
[151] Yoon S-Y, Kim J-K, Kim KH. A comparative study on tribological behavior of TiN and TiAlN coatings prepared by arc ion plating technique. Surf Coating Technol 2002;161:237–42. https://doi.org/10.1016/S0257-8972(02)00474-7.
[152] Kathrein M, Michotte C, Penoy M, Polcik P, Mitterer C. Multifunctional multi-component PVD coatings for cutting tools. Surf Coating Technol 2005;200:1867–71. https://doi.org/10.1016/j.surfcoat.2005.08.105.
[153] Cai Z, Pu J, Lu X, Jiang X, Wang L, Xue Q. Improved tribological property of VN film with the design of pre-oxidized layer. Ceram Int 2019;45:6051–7. https://doi.org/10.1016/j.ceramint.2018.12.076.
[154] Zhou Z, Rainforth WM, Lewis DB, Creasy S, Forsyth JJ, Clegg F, et al. Oxidation behaviour of nanoscale TiAlN/VN multilayer coatings. Surf Coating Technol 2004;177–178:198–203. https://doi.org/10.1016/j.surfcoat.2003.09.031.

[155] Zhou Z, Rainforth WM, Rodenburg C, Hyatt NC, Lewis DB, Hovsepian PE. Oxidation behavior and mechanisms of TiAlN/VN coatings. Metall Mater Trans A 2007;38:2464–78. https://doi.org/10.1007/s11661-007-9293-4.
[156] Zhou Z, Rainforth WM, Luo Q, Hovsepian PE, Ojeda JJ, Romero-Gonzalez ME. Wear and friction of TiAlN/VN coatings against Al2O3 in air at room and elevated temperatures. Acta Mater 2010;58:2912–25. https://doi.org/10.1016/j.actamat.2010.01.020.
[157] Mayrhofer PH, Hovsepian PE, Mitterer C, Münz W-D. Calorimetric evidence for frictional self-adaptation of TiAlN/VN superlattice coatings. Surf Coating Technol 2004;177–178:341–7. https://doi.org/10.1016/j.surfcoat.2003.09.024.
[158] Constable CP, Yarwood J, Hovsepian P, Donohue LA, Lewis DB, Münz W-D. Structural determination of wear debris generated from sliding wear tests on ceramic coatings using Raman microscopy. J Vac Sci Technol A Vacuum, Surfaces, Film 2000;18:1681–9. https://doi.org/10.1116/1.582407.
[159] Luo Q. Temperature dependent friction and wear of magnetron sputtered coating TiAlN/VN. Wear 2011;271:2058–66. https://doi.org/10.1016/j.wear.2011.01.054.
[160] Hovsepian PE, Luo Q, Robinson G, Pittman M, Howarth M, Doerwald D, et al. TiAlN/VN superlattice structured PVD coatings: a new alternative in machining of aluminium alloys for aerospace and automotive components. Surf Coating Technol 2006;201:265–72. https://doi.org/10.1016/j.surfcoat.2005.11.106.
[161] Luo Q, Hovsepian PE. Transmission electron microscopy and energy dispersive X-ray spectroscopy on the worn surface of nano-structured TiAlN/VN multilayer coating. Thin Solid Films 2006;497:203–9. https://doi.org/10.1016/j.tsf.2005.10.086.
[162] Luo Q, Hovsepian PE, Lewis DB, Münz W-D, Kok YN, Cockrem J, et al. Tribological properties of unbalanced magnetron sputtered nano-scale multilayer coatings TiAlN/VN and TiAlCrYN deposited on plasma nitrided steels. Surf Coating Technol 2005;193:39–45. https://doi.org/10.1016/j.surfcoat.2004.07.058.
[163] Kong M, Shao N, Dong Y, Yue J, Li G. Growth, microstructure and mechanical properties of (Ti, Al)N/VN nanomultilayers. Mater Lett 2006;60:874–7. https://doi.org/10.1016/j.matlet.2005.10.053.
[164] Seidl WM, Bartosik M, Kolozsvári S, Bolvardi H, Mayrhofer PH. Improved mechanical properties, thermal stabilities, and oxidation resistance of arc evaporated Ti-Al-N coatings through alloying with Ta. Surf Coating Technol 2018;344:244–9. https://doi.org/10.1016/j.surfcoat.2018.03.014.
[165] Seidl WM, Bartosik M, Kolozsvári S, Bolvardi H, Mayrhofer PH. Influence of Ta on the fracture toughness of arc evaporated Ti-Al-N. Vacuum 2018;150:24–8. https://doi.org/10.1016/j.vacuum.2018.01.028.
[166] Mikula M, Truchlý M, Sangiovanni DG, Plašienka D, Roch T, Gregor M, et al. Experimental and computational studies on toughness enhancement in Ti-Al-Ta-N quaternaries. J Vac Sci Technol A Vacuum, Surfaces, Film 2017;35:060602. https://doi.org/10.1116/1.4997431.
[167] Sui X, Li G, Jiang C, Yu H, Wang K, Wang Q. Effect of Ta content on microstructure, hardness and oxidation resistance of TiAlTaN coatings. Int J Refract Met Hard Mater 2016;58:152–6. https://doi.org/10.1016/j.ijrmhm.2016.04.014.
[168] Yang Y, Xu YX, Chen L, Mayrhofer PH. Improved Ti-Al-N coatings through Ta alloying and multilayer architecture. Surf Coating Technol 2017;328:428–35. https://doi.org/10.1016/j.surfcoat.2017.09.016.
[169] Grossmann B, Tkadletz M, Schalk N, Czettl C, Pohler M, Mitterer C. High-temperature tribology and oxidation of Ti1−x−yAlxTayN hard coatings. Surf Coating Technol 2018;342:190–7. https://doi.org/10.1016/j.surfcoat.2018.02.062.
[170] Grossmann B, Jamnig A, Schalk N, Czettl C, Pohler M, Mitterer C. Tailoring age hardening of Ti1−xAlxN by Ta alloying. J Vac Sci Technol A Vacuum, Surfaces, Film 2017;35:060604. https://doi.org/10.1116/1.4995000.
[171] Koller CM, Hollerweger R, Sabitzer C, Rachbauer R, Kolozsvári S, Paulitsch J, et al. Thermal stability and oxidation resistance of arc evaporated TiAlN, TaAlN, TiAlTaN, and TiAlN/TaAlN coatings. Surf Coating Technol 2014;259:599–607. https://doi.org/10.1016/j.surfcoat.2014.10.024.
[172] Pfeiler M, Fontalvo GA, Wagner J, Kutschej K, Penoy M, Michotte C, et al. Arc evaporation of Ti–Al–Ta–N coatings: the effect of bias voltage and Ta on high-temperature tribological properties. Tribol Lett 2008;30:91–7. https://doi.org/10.1007/s11249-008-9313-6.
[173] Waldl H, Tkadletz M, Winkler M, Grossmann B, Czettl C, Pohler M, et al. Evolution of the thermal conductivity of arc evaporated fcc-Ti1-x-yAlxTayN coatings with increasing Ta content. Surf Coating Technol 2021;406:126658. https://doi.org/10.1016/j.surfcoat.2020.126658.
[174] Pfeiler M, Scheu C, Hutter H, Schnöller J, Michotte C, Mitterer C, et al. On the effect of Ta on improved oxidation resistance of Ti–Al–Ta–N coatings. J Vac Sci Technol A Vacuum, Surfaces, Film 2009;27:554–60. https://doi.org/10.1116/1.3119671.
[175] Mayrhofer PH, Rachbauer R, Holec D, Rovere F, Schneider JM. Protective transition metal nitride coatings. Compr. Mater. Process. 2014;4:355–88. https://doi.org/10.1016/B978-0-08-096532-1.00423-4. Elsevier.
[176] Warlimont H. Titanium and titanium alloys. Springer Handbooks; 2018. p. 199–210. https://doi.org/10.1007/978-3-319-69743-7_7.
[177] Hollerweger R, Riedl H, Arndt M, Kolozsvari S, Primig S, Mayrhofer PH. Guidelines for increasing the oxidation resistance of Ti-Al-N based coatings. Thin Solid Films 2019;688:137290. https://doi.org/10.1016/j.tsf.2019.05.009.
[178] Khetan V, Valle N, Duday D, Michotte C, Delplancke-Ogletree M-P, Choquet P. Influence of temperature on oxidation mechanisms of fiber-textured AlTiTaN coatings. ACS Appl Mater Interfaces 2014;6:4115–25. https://doi.org/10.1021/am405727p.
[179] Woydt M. Tribological characteristics of polycrystalline Magnéli-type titanium dioxides. Tribol Lett 2000;8:117–30. https://doi.org/10.1023/a:1019170831371.
[180] Gardos MN. Magnéli phases of anion-deficient rutile as lubricious oxides. Part I. Tribological behavior of single-crystal and polycrystalline rutile (TinO2n-1). Tribol Lett 2000;8:65–78. https://doi.org/10.1023/a:1019122915441.
[181] Gardos MN. The effect of anion vacancies on the tribological properties of rutile (TiO 2–x). Tribol Trans 1988;31:427–36. https://doi.org/10.1080/10402008808981844.
[182] Sui X, Li G, Jiang C, Gao Y, Wang K, Wang Q. Improved surface quality of layered architecture TiAlTaN/Ta coatings for high precision micromachining. Surf Coating Technol 2017;320:298–303. https://doi.org/10.1016/j.surfcoat.2016.12.083.
[183] Contreras E, Bejarano G, Gómez M. Synthesis and microstructural characterization of nanoscale multilayer TiAlN/TaN coatings deposited by DC magnetron sputtering. Int J Adv Manuf Technol 2019;101:663–73. https://doi.org/10.1007/s00170-018-2972-z.
[184] Contreras Romero E, Cortínez Osorio J, Talamantes Soto R, Hurtado Macías A, Gómez Botero M. Microstructure,

mechanical and tribological performance of nanostructured TiAlTaN-(TiAlN/TaN)n coatings: understanding the effect of quaternary/multilayer volume fraction. Surf Coating Technol 2019;377:124875. https://doi.org/10.1016/j.surfcoat.2019.07.086.
[185] Rebholz C, Leyland A, Matthews A. Deposition and characterisation of TiAlBN coatings produced by direct electron-beam evaporation of Ti and Ti-Al-B-N material from a twin crucible source. Thin Solid Films 1999;343(344):242–5. https://doi.org/10.1016/S0040-6090(98)01635-6.
[186] Rebholz C, Schneider JM, Voevodin AA, Steinebrunner J, Charitidis C, Logothetidis S, et al. Structure, mechanical and tribological properties of sputtered TiAlBN thin films. Surf Coating Technol 1999;113:126–33.
[187] Baker MA, Monclus MA, Rebholz C, Gibson PN, Leyland A, Matthews A. A study of the nanostructure and hardness of electron beam evaporated TiAlBN coatings. Thin Solid Films 2010;518:4273–80. https://doi.org/10.1016/j.tsf.2009.12.109.
[188] Morales-Hernández J, García-González L, Muñoz-Saldaña J, Espinoza-Beltrán FJ. Structure and mechanical properties of (Ti,Al)(B,N) coatings fabricated by reactive DC magnetron sputtering. Vacuum 2004;76:161–4. https://doi.org/10.1016/j.vacuum.2004.07.059.
[189] Rebholz C, Leyland A, Matthews A, Charitidis C, Logothetidis S, Schneider D. Correlation of elastic modulus, hardness and density for sputtered TiAlBN thin films. Thin Solid Films 2006;514:81–6. https://doi.org/10.1016/j.tsf.2006.02.038.
[190] Rebholz C, Ziegele H, Leyland A, Matthews A. Structure, mechanical and tribological properties of Ti–B–N and Ti–Al–B–N multiphase thin films produced by electron-beam evaporation. J Vac Sci Technol A Vacuum, Surfaces, Film 1998;16:2851–7. https://doi.org/10.1116/1.581431.
[191] Pawlak Z, Pai R, Bayraktar E, Kaldonski T, Oloyede A. Lamellar lubrication in vivo and vitro: friction testing of hexagonal boron nitride. Biosystems 2008;94:202–8. https://doi.org/10.1016/j.biosystems.2008.05.029.
[192] Cao Y, Du L, Huang C, Liu W, Zhang W. Wear behavior of sintered hexagonal boron nitride under atmosphere and water vapor ambiences. Appl Surf Sci 2011;257:10195–200. https://doi.org/10.1016/j.apsusc.2011.07.018.
[193] Martin JM, Le Mogne T, Chassagnette C, Gardos MN. Friction of hexagonal boron nitride in various environments. Tribol Trans 1992;35:462–72. https://doi.org/10.1080/10402009208982144.
[194] Podgornik B, Kosec T, Kocijan A, Donik Č. Tribological behaviour and lubrication performance of hexagonal boron nitride (h-BN) as a replacement for graphite in aluminium forming. Tribol Int 2015;81:267–75. https://doi.org/10.1016/j.triboint.2014.09.011.
[195] Mitterer C, Rödhammer P, Störi H, Jeglitsch F. Radio-frequency sputter deposition of boron nitride based thin films. J Vac Sci Technol A Vacuum, Surfaces, Film 1989;7:2646–51. https://doi.org/10.1116/1.575767.
[196] Pan Z, Sun H, Zhang Y, Chen C. Harder than diamond: superior indentation strength of wurtzite BN and lonsdaleite. Phys Rev Lett 2009;102:055503. https://doi.org/10.1103/PhysRevLett.102.055503.
[197] Liu Y, David Zhan G, Wang Q, He D, Zhang J, Liang A, et al. Hardness of polycrystalline wurtzite boron nitride (wBN) compacts. Sci Rep 2019;9:10215. https://doi.org/10.1038/s41598-019-46709-4.
[198] Moraes V, Bolvardi H, Kolozsvári S, Riedl H, Mayrhofer PH. Thermal stability and mechanical properties of Ti-Al-B-N thin films. Int J Refract Met Hard Mater 2018;71:320–4. https://doi.org/10.1016/j.ijrmhm.2017.11.027.
[199] Rebholz C, Monclus MA, Baker MA, Mayrhofer PH, Gibson PN, Leyland A, et al. Hard and superhard TiAlBN coatings deposited by twin electron-beam evaporation. Surf Coating Technol 2007;201:6078–83. https://doi.org/10.1016/j.surfcoat.2006.08.121.
[200] Veprek S, Veprek-Heijman MGJ, Karvankova P, Prochazka J. Different approaches to superhard coatings and nanocomposites. Thin Solid Films 2005;476:1–29. https://doi.org/10.1016/j.tsf.2004.10.053.
[201] Karvánková P, Vepřek-Heijman MGJ, Zawrah MF, Vepřek S. Thermal stability of nc-TiN/a-BN/a-TiB2 nanocomposite coatings deposited by plasma chemical vapor deposition. Thin Solid Films 2004;467:133–9. https://doi.org/10.1016/j.tsf.2004.03.046.
[202] Bobzin K, Brögelmann T, Kruppe NC, Carlet M. HPPMS TiAlCrSiN - influence of substrate bias and pulse frequency on cutting performance. Surf Coating Technol 2020;397:126056. https://doi.org/10.1016/j.surfcoat.2020.126056.
[203] Kuo Y-C, Wang C-J, Lee J-W. The microstructure and mechanical properties evaluation of CrTiAlSiN coatings: effects of silicon content. Thin Solid Films 2017;638:220–9. https://doi.org/10.1016/j.tsf.2017.07.058.
[204] Shen H, Kong W, Zhou W, Kong D. Surface characteristics and wear resistance of AlCrTiSiN coatings at high temperatures. Surf Rev Lett 2019;26:1850159. https://doi.org/10.1142/S0218625X18501597.
[205] Ichijo K, Hasegawa H, Suzuki T. Microstructures of (Ti,Cr,Al,Si)N films synthesized by cathodic arc method. Surf Coating Technol 2007;201:5477–80. https://doi.org/10.1016/j.surfcoat.2006.07.016.
[206] Ezura H, Ichijo K, Hasegawa H, Yamamoto K, Hotta A, Suzuki T. Micro-hardness, microstructures and thermal stability of (Ti,Cr,Al,Si)N films deposited by cathodic arc method. Vacuum 2008;82:476–81. https://doi.org/10.1016/j.vacuum.2007.07.048.
[207] Hutchings IM, Shipway P. Tribology: friction and wear of engineering materials. ed. United Kingdom: Butterworth-Heinemann; 2017. https://doi.org/10.1016/0261-3069(92)90241-9.
[208] Chang Y-Y, Hsiao C-Y. High temperature oxidation resistance of multicomponent Cr–Ti–Al–Si–N coatings. Surf Coating Technol 2009;204:992–6. https://doi.org/10.1016/j.surfcoat.2009.04.009.
[209] Kim MJ, Lee DB. Oxidation of TiAlCrSiN thin films at 1000°C in air. Appl Mech Mater 2015;719–720:127–31. https://doi.org/10.4028/www.scientific.net/amm.719-720.127.
[210] Lee DB. High-temperature oxidation of the TiAlCrSiN film deposited on the cemented hard carbide. J Korean Inst Surf Eng 2014;47:252–6. https://doi.org/10.5695/jkise.2014.47.5.252.
[211] Siwawut S, Saikaew C, Wisitsoraat A, Surinphong S. Cutting performances and wear characteristics of WC inserts coated with TiAlSiN and CrTiAlSiN by filtered cathodic arc in dry face milling of cast iron. Int J Adv Manuf Technol 2018;97:3883–92. https://doi.org/10.1007/s00170-018-2200-x.
[212] Khanchaiyaphum S, Saikaew C, Wisitsoraat A, Surinphong S. Wear behaviours of filtered cathodic arc deposited TiN, TiAlSiN and TiCrAlSiN coatings on AISI 316 stainless steel fishing net-weaving machine components under dry soft-sliding against nylon fibres. Wear 2017;390–391:146–54. https://doi.org/10.1016/j.wear.2017.07.018.

Willey Yun Hsien Liew. He is a Professor and Chartered Engineer (CEng) at the Faculty of Engineering, Universiti Malaysia Sabah. He received his BEng in Mechanical Engineering (1st class honours) from the University of Leicester in 1991 and PhD from the

University of Cambridge in 1998 under the Cambridge Commonwealth Trust and the Overseas Research Students Scholarship. He was the recipient of the Institution of Mechanical Engineers (IMechE)/Shell Oils Tribology Award, Institution of Mechanical Engineers (IMechE) Project Prize and Institution of Mechanical Engineers (IMechE) Frederick Barnes Waldron Prize. His research interests include tribology, precision machining, nanocoatings and novel carburization process. He serves as a reviewer for several renowned international journals.

Hooi Peng Lim. She received her BEng in Mechanical (Materials) and MEng in Mechanical (by research) from Universiti Teknologi Malaysia, and second MEng in Mechanical from Queensland University of Technology, Brisbane Australia. She is now a PhD student at Universiti Malaysia Sabah conducting research on the tribological behaviour of thin coatings.

Gan Jet Hong Melvin. He received his PhD from Shinshu University, Japan in 2015. Then, he joined Institute of Carbon Science and Technology, Japan for 1 year as a researcher. Now, he is a Senior Lecturer in Mechanical Engineering Program and a Research Fellow of Centre of Energy and Advanced Materials at the Faculty of Engineering, Universiti Malaysia Sabah, Malaysia. His major field is related to materials science, which includes nanoparticles, hybrid nanomaterials, carbon-based nanomaterials, and composite materials. Some of his previous and currently active projects and works are related to polymer-based electroactive actuators, electromagnetic wave absorber, energy storage devices, solar absorber, and biomass derived carbon materials which are published in peer-reviewed journals, books including book chapters, conference proceedings, and abstracts. He is also an active reviewer for several material-related journals, a Professional Engineer of Board of Engineers, Malaysia, and a Professional Technologist of Malaysia Board of Technologists.

Jedol Dayou. He received his PhD from the University of Southampton in 2000. Currently, he is an Associate Professor at the Faculty of Science & Natural Resources, Universiti Malaysia Sabah. He has published over 100 scientific articles in renowned international journals and received numerous innovation awards. His current research interests include interaction of energy and matter, acoustics and vibration, and biophysics.

Zhong-Tao Jiang (PhD). He is an Associate Professor in Physics and Nanotechnology at Murdoch University. His research interests include materials science and engineering, functional thin films (optical, dielectric, mechanical, thermal and biological composite materials), surface physics and technology. Zhong-Tao is an expert in nanostructured and nanosized material characterization using advanced spectroscopic and microscopic techniques, including synchrotron radiation facilities. He is very proficient in investigating, by computational simulation/modelling, various physical properties (thermal, electronic, mechanical, and optical details), for functional composite materials, including high strength low alloy steels, welding and biological materials. He has published over 200 scientific articles in renowned international journals with more than 2200 citations.